HAL
open science

Etude des parois de domaines dans les nanofils magnétiques

Ségolène Jamet

To cite this version:

Ségolène Jamet. Etude des parois de domaines dans les nanofils magnétiques. Physique [physics]. Université Grenoble Alpes, 2015. Français. NNT : 2015GREAY068 . tel-01451511

HAL Id: tel-01451511

https://theses.hal.science/tel-01451511v1

Submitted on 1 Feb 2017

HAL is a multi-disciplinary open access archive for the deposit and dissemination of scientific research documents, whether they are published or not. The documents may come from teaching and research institutions in France or abroad, or from public or private research centers.

L'archive ouverte pluridisciplinaire **HAL**, est destinée au dépôt et à la diffusion de documents scientifiques de niveau recherche, publiés ou non, émanant des établissements d'enseignement et de recherche français ou étrangers, des laboratoires publics ou privés.

UNIVERSITÉ GRENOBLE ALPES

THÈSE

Pour obtenir le grade de

DOCTEUR DE L'UNIVERSITÉ GRENOBLE ALPES

Spécialité : **Nanophysique**

Arrêté ministériel : 7 août 2006

Présentée par

Ségolène JAMET

Thèse dirigée par **Jean-Christophe TOUSSAINT**
et
codirigée par **Olivier FRUCHART**

préparée au sein de l'**Institut Néel**
dans **l'École Doctorale de Physique**

Etude des parois de domaines dans des nanofils magnétiques

Thèse soutenue publiquement le **30 Octobre 2015,**
devant le jury composé de :

M. Bernard DIENY,
Directeur de recherche, CEA Spintec (Grenoble), Président
M. Jose Maria DE TERESA,
Professeur, Université de Zaragoza (Zaragoza, Espagne), Examinateur
M. Thibaut DEVOLDER,
Directeur de Recherche (IEF Orsay), Rapporteur
M. Olivier FRUCHART,
Directeur de Recherche, CNRS (Institut Néel, Grenoble), Co-Directeur de Thèse
Mme Laura HEYDERMAN
Professeur, ETH Zürich et PSI (Villigen, Suisse), Rapporteur
M. André THIAVILLE,
Directeur de Recherche (LPS Orsay), Examinateur
M. Jean-Christophe TOUSSAINT
Professeur, Grenoble INP et CNRS (Institut Néel, Grenoble), Directeur de Thèse

Remerciements

Vient le temps des remerciements....Presque le plus difficile à écrire m'avait-on dit. Je dois admettre que oui. Ce n'est pas basé sur des résultats obtenus durant la thèse, quoiqu'on remercie bien volontiers les personnes ayant aidé à obtenir de bon résultats. Il ne faut oublier personne aussi. Enfin, un simple merci, le mot que l'on dit tous les jours, sans y prêter attention ne semble pas forcément adapté. Alors je vais essayer (même si un verre de vin dit qu'il faut faire ou ne pas faire et non pas essayer).

Je tiens en premier lieu à remercier l'Institut Néel, mon laboratoire d'accueil et plus particulièrement l'équipe Micro et NanoMagnétisme. Avec certain(e)s, il se reconnaitront, je suis allée au fond d'un cratère à Hawaii, j'ai fractionné, bivouaqué sur les crêtes du Vercors ou bien fait de l'accro-branches. Je n'aurais pas pu effectuer ma thèse sans le financement de l'Europe à travers le projet M3d, qui a commencé en même temps que ma thèse. Il y a aussi mes deux fabuleux directeurs de thèse, Jean-Christophe Toussaint et Olivier Fruchart. Tous les deux différents et tellement complémentaires pour m'aiguiller, m'épauler, m'aider. Je n'ai pas partagé que des discussions scientifiques avec eux. Discussions scientifiques très riches, parfois emplies de doutes, à la fin desquelles il m'est arrivé de me poser bien plus de questions qu'au début. On a aussi bien ri, joué avec les mots et regardé un tas de configurations de fils 3D sur un écran 2D qui nous on fait tourner la tête.

Il y a aussi eu les conférences, les colloques Louis Néel et les temps de faisceau au synchrotron de Trieste. Outre l'aspect scientifique de ces moments, qui sont propices à l'apprentissage en étant plongé en permanence dans la science, j'ai passé de très bons moments. On (au moins moi) se souviendra des "mois bissextiles" et de la glace extra noire à Regensburg, de Dresde et du piano "numerikakeu" au pied de la Frauenkirche. Il y a aussi eu la croisière sur le Rhin, encore une fois conclue par un glace. Je n'oublierai pas non plus mon initiation aux bonnes bières en piochant dans toutes les bonnes bouteilles que mes compagnons commandaient. Les temps de faisceau et les conférences ont été l'occasion de petits détours touristiques toujours très appréciés. Les protagonistes sauront de quoi je parle en évoquant les grotte, porte bloquée ou glace à l'italienne, les "4° au Nord du pole Nord" lors d'un footing matinal (trop matinal certainement), et enfin de mousse au chocolat maison au plastique. Bien évidemment, personne ne peut oublier le sourire d'Onur et la gentillesse d'Andrea, le café nocturne bien accompagné de papillotes (ça fonctionne aussi avec du chocolat plus classique). Volontairement, je n'ai cité personne, mais chacun se reconnaitra, je l'espère.

Enfin, je remercie tous ceux qui ont contribué, de près ou de loin, à la bonne réussite de ma thèse, tant scientifiquement que personnellement. Merci Frank (Balestro) pour m'avoir aidé et donné un coup de pouce moral.

Contents

1 Micromagnetism: concepts and numerics **17**
1.1 Nanomagnetism . . . 18
1.1.1 The various energies found in magnetic systems . . . 18
1.1.2 Characteristic lengths . . . 21
1.1.3 Critical single-domain size . . . 22
1.1.4 Reversal modes . . . 23
1.1.5 Landau-Lifshitz-Gilbert equation . . . 24
1.2 Domain walls in one-dimensional systems . . . 26
1.2.1 General features of domain walls . . . 26
1.2.2 One dimensional model - The Bloch domain wall . . . 28
1.2.3 Domain walls in strips . . . 31
1.2.4 Domain walls in wires: theory . . . 34
1.3 Micromagnetism - Numerics . . . 37
1.3.1 Overview of numerical simulations . . . 37
1.3.2 Methods to compute the demagnetizing field in FEM . . . 39
1.3.3 The home-made finite element code FeeLLGood . . . 43
1.3.4 Towards second order . . . 47
1.3.5 About the norm of the magnetization . . . 48

2 Phase diagram of domain walls: from nanostrips to nanowires **49**
2.1 Why does it seem interesting and relevant to build a phase diagram? . . . 50
2.2 Domain wall topology . . . 51
2.2.1 Transverse versus vortex wall . . . 51
2.2.2 Bloch point walls . . . 52
2.3 Phase transitions . . . 52
2.3.1 Definitions . . . 52
2.3.2 Discussion about the first-order transition between TW and VW . . . 52
2.3.3 TVW-BPW . . . 56
2.3.4 Asymmetries . . . 56
2.4 Micromagnetic simulations . . . 57
2.4.1 First-order transitions . . . 57
2.4.2 Second-order transitions and estimators for their order parameter . . . 58
2.5 Scaling law for domain wall energy and width . . . 63

3 Shadow XMCD-PEEM: evidencing domain wall types in magnetic cylindrical wires **67**
3.1 Principle of the microscopy technique . . . 68
3.1.1 Dichroism in $3d$ ferromagnetic elements . . . 68
3.1.2 From atomic absorption to measuring absorption on a material . . . 70
3.1.3 The Photo-Emission-Electron-Microscope . . . 70
3.2 Experimental imaging . . . 72
3.2.1 Samples . . . 72

3.2.2 Set-up . . . 73
3.2.3 Measurements . . . 73
3.3 Developing simulations for the quantitative analysis of shadow XMCD-PEEM . . 74
3.3.1 Absorption model . . . 74
3.3.2 Numerical implementation . . . 76
3.3.3 Test cases . . . 78
3.4 Comparing simulations and experiments . . . 81
3.5 Discussion about the experimental contrast and resolution . . . 83
3.5.1 Microscope settings (start voltage, plane of focus) . . . 83
3.5.2 Photon energy . . . 87
3.5.3 Background level in PEEM imaging . . . 87
3.5.4 Scattering effects . . . 88
3.5.5 Electric field distortion . . . 88
3.6 Conclusion . . . 89

4 Conclusion **91**

5 Perspectives **93**

6 Appendix **95**
A Some FeeLLGood modifications . . . 95
A - 1 Speed optimization of the demagnetizing field calculation . . . 95
A - 2 Modification of the formulation used in FeeLLGood: framework with the domain wall . . . 95
B Numerical tool development . . . 97
B - 1 Ray tracing . . . 97
B - 2 Surface magnetization maps . . . 101
B - 3 Computation of a discrete vector field curl . . . 103
B - 4 Estimation of the domain wall width . . . 105
B - 5 Analytical test cases for XMCD . . . 106
C Simulation of the MFM contrast . . . 111
C - 1 Phase contrast in MFM imaging . . . 112
C - 2 MFM models . . . 112
C - 3 Simulations and results . . . 113

Introduction

In 2008 Parkin proposed [1] a concept for a three-dimensional (3D) data storage device, in which series of magnetic domain walls (DWs) act as bits to be moved along vertical nanowires. This concept answers the rising problem of volume of stored data and the increase of their density. The 3D data storage thus appears as a promising solution. So far, physics has been essentially based on flat strips which are easier to fabricate using lithography. However, recent improvements in fabrication techniques enable to address fundamental questions concerning domain walls in cylindrical nanowires. Indeed, this geometry is the required geometry for the race track memory proposed by IBM. Not only to integrate DWs in memories is of great interest, DWs are associated with new physics dealing with their magnetization configuration, spin-polarized currents or spin-Hall current.

As will be explained in this manuscript, in this type of geometry several types of DWs exist. Their existences are linked to the dimensions and geometry of the system. Moreover the speeds of these different DWs are not all similar and can reach 1000 m/ sec for the BPW with an applied field of about 5 mT [2]. As will be shown later, this latter DW is thus of great interest. To obtain the desired type of DW, the system needs to be properly designed but its magnetic history has a large impact on the type of DW. The construction of a phase diagram of DWs in a geometry ranging from nanostrips to nanowires appears as a crucial tool for this aim. Not only the type of DW according to geometry can be studied but also various physical features characterizing DWs.

With a phase diagram it is then possible to design the system in order to favor the nucleation of the desired DW. In a second step I applied simulations to experiments I took part in and more precisely to image DWs in nanowires, systems with few experimental studies. The most accessible imaging method at the laboratory is the magnetic force microscopy (MFM). However the spatial and temporal resolutions of this method are too low and do not enable to discriminate between different types of DWs. Improvements on the spatial resolution are ongoing work. An alternative imaging technique is the X-ray Magnetic Circular Dichroism Photo Emission Electron Microscopy (XMCD-PEEM). This tool appears as crucial in nanomagnetism and spintronics. Its good enough spatial resolution make possible the study of DWs.

This manuscript is organized as follows. First are presented the studied systems with the physical background. The second part presents an extended phase diagram of magnetic domain walls in a geometry ranging from nanostrips to nanowires. This phase diagram is supported by physical features describing DWs. The third part is dedicated to the application of simulations on XMCD PEEM imaging. Analysis of experimental contrasts is supported by simulations of the XMCD contrast. Technical aspects of the shadow XMCD-PEEM technique are presented and discussed. At the end of the manuscript, perspectives of the numerical study about the motion of DW in cylindrical nanowires are presented. Details about simulation aspects are explained in the appendix.

Introduction (Français)

En 2008, Parkin a proposé [1] un concept de dispositif en 3D pour le stockage de la mémoire dans lequel des séries de parois de domaines magnétiques (DWs) jouent le rôle de bits qui seront déplacés le long de l'axe du fil. Ce concept répond au problème grandissant du stockage de données et de l'augmentation de leur densité. Dans cet optique, le stockage 3D de la mémoire apparait comme une solution prometteuse. Jusqu'à présent, les études se sont essentiellement basées sur les bandes plates, lesquelles sont plus faciles à fabriquer en utilisant la technique de lithographie. Cependant, de récentes avancées dans les techniques de fabrication permettent de traiter des questions fondamentales à propos des parois de domaines dans les nanofils cylindriques. En effet, cette géométrie est très pertinente pour le concept de mémoire proposé par IBM. Cependant, ce n'est pas uniquement l'application pour les mémoires que ces parois de domaine suscitent de l'intérêt. En effet, ces parois sont associées à une nouvelle physique en rapport avec leur configuration micromagnétique, le courant polarisé en spin et l'effet Hall de spin.

Comme il sera expliqué dans ce manuscrit, plusieurs types de paroi existent dans les nanofils. Leur existence est liée à la géométrie et aux dimensions du système, or les vitesses de ces parois diffèrent. Cette vitesse peut atteindre 1000 m/sec pour une paroi de type point de Bloch sous champ magnétique d'environ 5 mT [2]. Ce dernier type de paroi présente un grand intérêt, ce qui sera expliqué au cours de ce manuscrit. Pour obtenir le type de paroi souhaité, les dimensions du système doivent être correctement définies. Cependant, l'histoire magnétique du système joue également un rôle important pour le choix du type de paroi par le système. La construction d'un diagramme de phase des parois de domaines magnétiques semble alors un outil clé pour choisir les dimensions du système en fonction du type de paroi souhaité. Dans cette construction, ce n'est pas uniquement le type de paroi qui a été étudié, mais aussi des aspects physique caractérisant les parois de domaine.

Grâce à un diagramme de phase, il est alors possible de dimensionner le système pour favoriser la nucléation du type de paroi de domaine souhaité. L'étape suivante sera alors d'observer ces parois en utilisant des techniques d'imagerie. La technique d'imagerie la plus accessible au laboratoire est la microscopie à force magnétique (MFM). Cependant, les résolutions spatiale et temporelle de cette technique sont trop faibles et ne permettent pas de différencier les différents types de paroi. Des améliorations sur la résolution spatiale de la MFM. Une technique alternative est le dichroisme circulaire magnétique des rayons X couplé à la Microscopie par émission de photo-électrons (XMCD-PEEM). Cet outil apparait comme crucial en nanomagnétisme et spintronique avec des résolutions spatiale et temporelle suffisantes permettant l'étude des parois de domaine.

Le manuscrit est organisé ainsi. Premièrement, les systèmes étudiés ainsi que les bases physiques nécessaires sont présentés. La seconde partie présente une diagramme de phase étendu des parois de domaine magnétique pour une géométrie allant des nanobandes aux nanofils. Ce diagramme de phase est complété par des aspects physiques décrivant les parois. La troisième partie est dédiée à l'observation des parois par en utilisant la technique XMCD-PEEM. L'analyse des résultats expérimentaux est étayée par des simulations du contraste dichroique. A la fin de ce manuscrit, des perspectives sur l'étude numérique sur la propagation des parois de domaine dans les nanofils est présentée. Les détails concernant les simulations sont expliqués en annexe.

Résumé 1^{er}chapitre (Français)

Les concepts du nanomagnétisme sont connus depuis longtemps. L'existence de parois de domaine séparant des zones à aimantation uniforme ou bien les principes du ferromagnétisme sont connus depuis le début du 20eme siècle et ont été étudiés depuis les années 1960 REF. Au cours des deux dernières décennies, de nombreux développements expérimentaux ont été effectués grâce, en partie, aux progrès en nanofabrication et en imagerie.

Au cours des dernières années, la dynamique des parois de domaine connait un intérêt grandissant. Le but est d'en faire l'ingrédient principal de nouvelles mémoires magnétiques. Cependant ce n'est pas seulement leur application dans ces dispositifs qui en fait des objets intéressants. La physique liée à ces objets, particulièrement dans les systèmes compacts avec une section carrée ou circulaire connait un intérêt grandissant.

En nanomagnétisme, il y a quatre énergies qui sont l'énergie d'échange, l'énergie d'anisotropie magnétocristalline, l'énergie Zeeman et l'énergie dipolaire ou magnétostatique. L'énergie d'échange est une énergie à courte portée et tend à aligner les moments magnétiques. L'énergie Zeeman entre en jeu lorsqu'un champ magnétique extérieur est appliqué sur le système. Elle tend à aligner l'aimantation avec le champ magnétique. L'énergie d'anisotropie magnétocristalline provient des différentes orientations cristallines d'un solide et du champ cristallin. Cela va donc créer des axes faciles ou difficiles selon lesquels il sera, ou non, favorable d'orienter l'aimantation. Enfin, l'énergie dipolaire vient du champ de fuite de chacun des moments magnétiques qui tend à changer l'orientation des moments magnétiques voisin. Cette énergie est à longue portée.

Lorsque ces énergies entrent en compétition dans un système, on définit des longueurs caractéristiques. Si l'énergie magnétocristalline et l'échange sont présentes, on définit la longueur d'échange d'anisotropie Δ_{u}. Lorsque seules l'énergie dipolaire et l'énergie d'échange sont en compétition, on définit la longueur d'échange dipolaire Δ_{d}. Parce que les constantes d'échange et dipolaire varient peu pour les matériaux doux communs, $\Delta_{\mathrm{d}} \sim$ 3-5 nm.

Dans une nouvelle partie, sont présentés les modes de renversement. Le mode le plus simple conserve l'aimantation uniforme au cours de la rotation. Ce modèle a été proposé par Stoner et Wohlfarth et est applicable pour les petites particules seulement. Il existe d'autres modèles pour lesquels l'aimantation ne reste pas uniforme. Ce sont des cas extrêmes, pas nécessairement les plus pertinents expérimentalement.

La suite de ce chapitre est dédiée à la dynamique d'aimantation et à la dérivation de l'équation Landau-Lifshitz-Gilbert.

La deuxième section est consacrée aux parois de domaine dans les systèmes unidimensionnels. Après une présentation des parois de Bloch et de Néel pour les films minces, nous verrons le modèle unidimensionnel de Bloch incluant le profil d'aimantation, l'énergie, la largeur de paroi et la dynamique. Nous traiterons ensuite de la statique et de la dynamique des parois dans les bandes, à savoir des systèmes avec une section rectangulaire et relativement plate. Les parois sont de deux types, la paroi transverse pour les petites dimensions et la paroi vortex pour les grandes dimensions. Enfin, les parois dans les nanofils, à savoir des systèmes compacts ayant une section carrée ou circulaire, seront présentées. Dans de tels systèmes, on retrouve la paroi de type transverse, comme dans les bandes. Il existe un nouvel objet micromagnétique dans les fils par rapport aux bandes, la paroi point de Bloch.

La troisième partie est consacrée au micromagnétisme numérique. Après une présentation

des différentes méthodes de simulations (Monte Carlo, minimisation de l'énergie et intégration de l'équation LLG). C'est cette dernière que nous utilisons. Une présentation brève de la méthode des différences finies est présentée puis nous nous focaliserons sur la méthode des éléments finis qui est utilisée par la suite. Ensuite, un point important et couteux du micromagnétisme numérique est abordé, le calcul du champ démagnétisant qui requiert le plus de temps de calcul. La méthode des intégrales aux frontières est présentée, puis nous passerons aux détails de la méthode finalement utilisée, les méthodes multipolaires rapides, plus rapide que la première méthode. La fin de cette partie est dédiée au code développé au laboratoire pour la résolution de l'équation LLG et basé sur les éléments finis. Tout d'abord, il s'agit d'expliquer comment on passe de la formulation forte et locale à une formulation faible, dite intégrale. La première n'est pas utilisable en éléments finis puisque le Laplacien n'est pas défini aux noeuds du maillage. On aboutit donc à un schéma dit explicite, relativement classique. Une fois cette formulation faible obtenue, on peut aborder la discrétisation temporelle et la présentation du θ-schéma. Ce schéma, suivant la valeur de θ choisie est inconditionnellement stable. Ceci est liée à la dissipation d'énergie qui est abordée par la suite. Etant donné qu'en micromagnétisme la norme de l'aimantation est conservée, la variation temporelle de l'aimantation est perpendiculaire à l'aimantation, on appelle cela le plan tangent. L'idée est alors de projeter l'équation LLG sur ce plan tangent. Enfin, on abordera rapidement l'ordre 2 en temps.

Résumé 2^{eme}chapitre (Français)

Un diagramme de phase des parois de domaines magnétiques est une représentation dans le plan (épaisseur, largeur) de la paroi de plus basse énergie. Le but de ce diagramme est de comprendre les parois dans les systèmes unidimensionnels. Les simulations seront donc effectuées pour des géométrie allant des bandes aux fils, ces derniers ayant une section carrée ou circulaire. De plus, il semblerait que la physique liée aux bandes est différente de celle des fils. Or, si on augmente continument l'épaisseur d'une bande, on obtient un fil à section carrée. Les deux physiques devraient donc est similaires d'où le souhait de proposer une vision unifiée de ces systèmes. Enfin, les parois transverses dans les fils sont parfois nommées *pseudo-transverse* ou *paroi hélical*. La paroi point de Bloch a aussi été nommée paroi vortex. Cette occurrence du mot *pseudo* signifie le développement d'aspects de la distribution d'aimantation qui ne sont pas compris. Afin de mieux décrire les configurations micromagnétiques, des estimateurs on définit des estimateurs basés sur des grandeurs physiques. Au début de ma thèse, le diagramme de phase connu était celui présenté par Thiaville [3].

Avant de s'intéresser précisément au diagramme et aux transitions de phases, on s'intéresse à la topologie. Si on fait deux coupes perpendiculaires d'une paroi transverse dans un fil à grand diamètre, on peut observe à la fois une distribution de type transverse, similaire à celui des bandes et une distribution de type vortex comme dans les bandes. Les parois transverses dans les fils peuvent donc présenter les deux caractéristiques. En terme de topologie, la paroi transverse et la paroi vortex partagent la même classe topologique et le fait que le flux magnétique traverse le fil ou la bande suivant le diamètre ou la largeur. Pour cela, on nommera ces parois transverse-vortex quand cela à lieu d'être. La paroi point de Bloch fait partie d'une autre classe puisque l'aimantation est toujours parallèle à la surface. Une manière de vérifier cette topologie est de regarder la projection de l'aimantation sur la normale locale à la surface dans un plan (θ, z). Pour cela j'ai développé un code qui est un post-traitement des configurations micromagnétiques obtenues avec FeeLLGood. Ces cartes d'aimantation de surfaces confirment les classes topologiques établies. Avec des considérations de symétrie et de topologie, on peut proposer un diagramme de phase pour la transition du premier ordre entre la paroi vortex et la paroi transverse. Dans les bandes, l'épaisseur et la largeur sont équivalentes. La diagonale du diagramme est donc un axe de symétrie. De plus, en partant d'une paroi transverse dans une bande, en augmentant continument l'épaisseur de la bande tout en maintenant la direction de la paroi, on obtient une paroi de type vortex. Comme la transformation se fait de façon continue, sur la diagonale, les deux parois sont dégénérées. Enfin pour transformer la paroi vortex, avec un coeur suivant x par exemple, en une paroi transverse suivant y, la direction de la paroi doit changer d'orientation. Cela signifie que le système doit passer une barrière d'énergie avec deux minima de part et d'autre. La transformation est donc de premier ordre.

Comme on l'a vu, dans les bandes, une paroi est du type soit transverse soit vortex. Cela n'a pas été quantifié auparavant parce que cet circulation de l'aimantation autour du coeur de la paroi transverse n'est pas toujours présent. J'ai donc souhaiter quantifier cette circulation. Pour cela j'ai utilisé le rotationnel de l'aimantation. Comme il s'agit d'un vecteur, il est possible de le projeter sur une base orthonormale pertinente incluant la direction de la paroi transverse et l'axe du fil. Alors que nous nous intéressions au développement de la circulation autour de l'axe de la transverse, la projection sur l'axe du fil montre aussi un développement de la

circulation de l'aimantation le long de l'axe du fil. La circulation dans les deux directions de la circulation, transverse et longitudinale, apparait, dans les deux cas, à partir de 7 fois la longueur d'échange dipolaire. Le curling longitudinal se développe pour diminuer l'énergie magnétostatique proportionnelle à la densité de charges volumiques en répartissant ces charges. Ces charges sont dues au caractère tête-à-tête de la paroi transverse et donc proportionnelles à la section du fil. Le curling transverse sert à diminuer l'énergie dipolaire due aux charges de surfaces. De plus, le vortex qui se développe autour de l'axe de la transverse peut être vu comme deux parois transverses asymétriques de polarités opposées et en ce sens comme une brisure de symétrie. Le développement de la circulation est donc une transition de phase du 2ème ordre. Cela signifie qu'il n'y a pas de métastabilité de part et d'autre de la transition.

On peut maintenant revenir à la paroi point de Bloch et à la transition avec la paroi transverse vortex. Pour des raisons de symétrie, nous prévoyons que la zone de stabilité de la paroi point de Bloch ne se limite pas à la diagonale du diagramme mais s'étendent pour les bandes épaisses. En effet, une déformation infinitésimale du fil, qu'il soit à section carrée ou circulaire, ne peut pas conduire à un changement de topologie de la paroi. De plus, nous confirmons la transition de la paroi transverse à la paroi point de Bloch à 7 fois la longueur d'échange dipolaire.

Des aspects plus fins sur la circulation sont développés ainsi que sur le développement d'asymétries tant dans les parois transverse que point de Bloch.

Résumé 3^{eme}chapitre (Français)

Le chapitre précédent était dédiés principalement théorique. Dans ce chapitre sur la technique d'imagerie XMCD-PEEM en transmission, le but est d'appliquer les simulations à des expériences auxquelles j'ai pris part. Afin d'observer la structure des parois, la résolution doit être inférieure à 50 nm. Parmi les techniques offrant cette résolution spatiale, on peut citer le SPLEEM (Spin Polarized Low Electron Emission Microscopy) et le SEMPA (Scanning Electron Microscopy with Polarization Analysis) qui sondent les couches atomiques de surface. Cependant, avec le SEMPA il est possible d'utiliser des électrons de plus haute énergie qui permet d'entrer plus profondément dans le matériau. Il existe aussi des techniques qui sondent le volume de l'échantillon. Ce sont des techniques de transmission qui donnent donc accès à des informations moyennées le long du trajet du faisceau. On peut citer par exemple l'holographie, la microscopie de Lorentz, le (S)TXM (Scanning Transmission X-ray Microscopy). La technique de XMCD-PEEM (X-ray Magnetic Circular Dichroism-PhotoElectron Emission Microscopy) se pose comme intermédiaire. Ce n'est pas une technique de surface à proprement parlé mais elle ne permet pas de sonder le magnétisme en profondeur. C'est cette technique qui est retenue pour sa versatilité et l'expérience que nous avons avec au laboratoire.

La technique XMCD-PEEM a récemment été appliquée à des objets en trois dimensions. Avec ce type de systèmes, on a accès à l'ombre du fil projetée sur le substrat. Nous ne sommes pas les premiers à utiliser cette technique qui a été nommée *shadow XMCD-PEEM* [4] et utilisée ensuite par plusieurs auteurs [4–8]. Avec cette technique, comme les rayons X sont absorbés le long de leur trajet dans l'objet en fonction de leur hélicité et de l'aimantation locale, le contraste ne peut pas être interprété facilement. Afin d'aider à la compréhension des résultats, Streubel *et al.* [9, 10] ont simulé le contraste dans l'ombre pour des tubes enroulés, donc proches de systèmes 2D. De plus, le contraste à la surface des tubes n'étaient pas simulé. Dans le cadre de ce travail, la simulation du contraste est basée sur des configurations micromagnétiques 3D obtenues par relaxation de l'aimantation.

La première partie de ce chapitre présente le principe de la microscopie XMCD-PEEM. Cela commence par une description du dichroïsme dans les matériaux ferromagnétiques $3d$, le décalage des bandes spin up et spin down. Ensuite la présentation aborde le processus qui permet de passer de l'absorption atomique des photons à la mesure de l'absorption par le matériau et notamment la production de photo-électrons. Ces photons électrons sont conduits jusqu'au capteur à l'aide de lentilles qui permettent de collimater le faisceau. Le contraste magnétique vient de la différence d'intensité des photo-électrons produits pour chacune des hélicités. La technique XMCD-PEEM permet de choisir l'énergie des photons incidents et l'intensité résultante est différente suivant les éléments chimiques. Pour chaque éléments, l'absorption résonante donne lieu à deux pics aux seuils L2 et L3. De plus, l'imagerie XMCD est sensible à l'aimantation puisque l'absorption des photons dépend de l'orientation relative de l'aimantation locale et de la polarisation des photons. Le contraste magnétique est ensuite calculé en faisant le ratio de la différence sur la somme des intensités des photo-électrons pour chacune des polarisations.

Les fils utilisés sont produits en collaboration avec le département de chimie de l'université d'Erlangen (Allemagne). Le principe de base pour produire des fils est d'anodiser une membrane d'alumine et de remplir les pores par électro-déposition. Pour produire des fils avec des modulations de diamètre, il est possible d'utiliser soit l'anodisation pulsée [11] soit l'anodisation

en trois étapes. La matrice d'alumine est ensuite dissoute et les fils dispersés sur un substrat de silicium.

Pour imager une paroi, nous procédons en deux étapes. Premièrement, les fils sont alignés avec le faisceau incident. Un changement de contraste de noir vers blanc indique un changement d'orientation de l'aimantation et donc la présence d'une paroi. Afin de regarder la structure de la paroi, l'échantillon est tourné de 90° hors du microscope, ce qui requiert beaucoup de temps. Une fois le faisceau perpendiculaire au fil, nous avons accès à la structure de la paroi. Il est fondamental de constater qu'il y a du contraste dans l'ombre du fil, alors qu'il n'y a pas de matériau magnétique à cet endroit. Les simulations qui s'ensuivent vont permettre de comprendre ces contrastes, très différents d'une paroi à l'autre. Ensuite, après une présentation du modèle d'absorption et de ses hypothèses, le code est vérifié en utilisant des cas tests dont on peut calculer la solution analytique afin de comparer les résultats. Le premier cas test est un fil uniformément aimanté avec l'aimantation parallèle au faisceau. Le second cas test est plus réaliste avec du curling orthoradial sur toute la longueur du fil. Ce dernier sera utile pour l'identification de la paroi point de Bloch. Dans les cas, on obtient un excellent accord entre les deux résultats. La comparaison des simulations avec l'expérience pour le point de Bloch montre un bon accord qualitatif. On a donc identifié une paroi point de Bloch. Cette identification a été confirmée avec les simulations. Cette observation est la première après une dizaine d'années de simulations. L'application de ce code de simulation du contraste XMCD-PEEM à une paroi transverse obtenue par simulations micromagnétiques montre aussi une très bon accord. Cependant, comme une paroi transverse n'est pas symétrique par rotation autour de l'axe du fil, il est important de pouvoir tourner le fil afin d'obtenir un accord avec l'expérience. De plus, le contraste dans l'ombre informe sur la direction du coeur de la paroi et sur les deux sens de rotation des circulations transverse et longitudinale.

Enfin, afin d'être plus quantitatif et d'obtenir des contrastes plus précis révélant au lieux le magnétisme, nous avons étudier l'influence des paramètres expérimentaux tels que la tension d'extraction des électrons, le focus et le signal de fond.

Conclusion (Français)

L'étude des parois de domaine dans les nanofils a connu un intérêt grandissant après la proposition par IBM d'une mémoire 3D. Dans cette application, les bits sont les parois de domaine. Cependant, au-delà de l'application pour le dispositif, de nombreux aspects physiques liés à ces parois sont d'un grand intérêt.

Il demeure de nombreux aspects physiques et numériques à étudier sur le sujet des parois de domaine magnétique. Cependant, nous avons continué le diagramme de phase des DWs pour une géométrie allant des nanobandes aux nanofils magnétiques. Sur la diagonale, les transitions de phase de premier et second ordre ont été recherchées. Cependant la transition de phase de second ordre entre les parois TVW et ATW n'a pas été trouvée. En effet, la paroi ATW n'est pas l'état fondamentale pour les fils avec les dimensions considérées, c'est-à-dire en-dessous de 150 nm. La paroi point de Bloch, prédit pour les fils à sections carrée et circulaire, donc sur la diagonale uniquement, étend son domaine d'existence sur une région autour de la diagonale. De plus, au-dessus de $7\Delta_{\mathrm{d}}$ pour TVW, un curling à la fois transverse et longitudinal se développe, le premier autour de l'axe de la paroi, le second le long de l'axe du fil. Ces deux directions de curling apparaissent comme une méthode pour diminuer l'énergie dipolaire pour les fils à large diamètre. Cette possibilité de développer du curling autour de deux directions est une explication pour l'existence du domaine de stabilité du BPW autour de la diagonale, le système préférant fermer son flux magnétique dès que les dimensions le permettent. Le curling semble alors une méthode plus efficace que l'asymétrie pour diminuer l'énergie magnétostatique. De plus, une loi d'échelle sur la largeur de paroi est établie.

L'étude des parois continue avec leur observation en utilisant l'imagerie. Afin d'obtenir une résolution spatiale suffisante, la technique XMCD-PEEM est choisie. L'observation des nanofils à section circulaire a été réalisée au cours de trois temps de faisceau durant ma thèse. Les conditions expérimentales, telles qu'un angle rasant de 16 ° permettent l'accès à l'ombre du fil, projetée sur le substrat. Cependant l'observation de la totalité de l'ombre est possible uniquement pour les fils suspendus au-dessus du substrat, soit parce qu'ils sont courbés, soit parce que les bouts de fil sont plus larges. L'ombre du fil contient des informations à propos de l'aimantation dans le volume du fil, moyennée le long du trajet du rayon X dans le fil. Cette technique donc une technique de surface, l'utilisation classique du XMCD-PEEM et une technique de surface, grâce à l'utilisation novatrice des informations contenues dans l'ombre.

Pour aider la compréhension du contraste magnétique qui s'avère complexe, un outil basé sur les simulations numériques a été développé. Cet outil permet de différencier la paroi TVW de la paroi BPW, ce qui n'est actuellement pas possible avec la MFM. Nous pouvons donc affirmer que la paroi point de Bloch a été observée pour la première fois. La comparaison entre le contraste simulé et le contraste expérimental montre un bon accord qualitatif. Les différences quantitatives peuvent provenir, par exemple, du signal de fond dans l'ombre non pris en compte dans les simulations. Ce signal doit en effet être évalué pour chaque série d'images.

Des paramètres expérimentaux tels que la tension d'extraction des photoélectrons, le plan de focus, le niveau de fond, ont été étudiés afin d'extraire un signal le plus physiquement pertinent.

L'étude de la propagation des parois de domaine sous champ magnétique fait partie du travail de thèse d'Alexis Wartelle. La relation entre la circulation du BPW et la direction du champ magnétique appliqué a été confirmée lors d'un temps de faisceau. L'étude numérique de cette

propagation sera une partie de la thèse de Beatrix Trapp.

Chapter 1

Micromagnetism: concepts and numerics

Concepts in nanomagnetism have been known for a long time. The existence of domain walls separating areas of uniform magnetization or principles of ferromagnetism are known since the early 20th century and have been studied from 1960s [12, 13]. Over the last two decades, several experimental developments were partly accomplished thanks to progresses in nanofabrication and imaging.
For the last years, the dynamics of magnetic domain walls has been of increasing interest. The goal is to make them part of new magnetic memory devices. However, not only the applications for memories are interesting but also their physical features, especially for compact systems with square or disk based cross-section, are of rising interest.
After a short description of the different energies involved in nanomagnetism, the characteristic lengths and the reversal modes, we will consider the Landau Lifshitz Gilbert equation describing precessional magnetization dynamics. This will be followed by a description of domain walls in almost dimensional systems and the Bloch model. Then, I will present cylindrical nanowires and their domain walls, with the promising new kind of domain wall, the Bloch point wall. The last part is dedicated to micromagnetism and numerics with a description of the fast multipole method and a presentation of the home-made finite element code FeeLLGood.

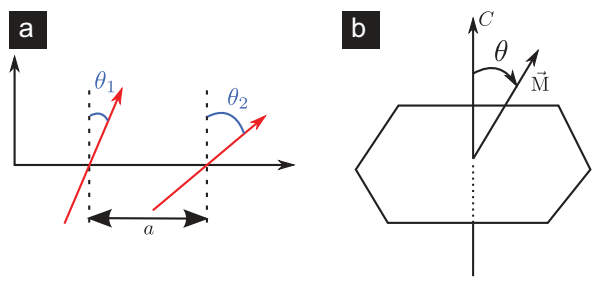

FIGURE 1.1: **Schematic for the energies**.(a) Exchange energy. (b) Uniaxial magnetocrystalline anisotropy in an hexagonal lattice.

1.1 Nanomagnetism

1.1.1 The various energies found in magnetic systems

In magnetism, there are various sources for the energy. They can be local (Zeeman and magnetocrystalline energy), short-ranged (exchange energy) or long-ranged (magnetostatic energy). Two or more of them often compete to reduce the total energy of the system leading to characteristic quantities such as length or energy.

The theory of micromagnetism does not consider each atom separately because it would be useless and give rise to a too large amount of data to describe them all due to the large number of atoms. Thus instead of the magnetic moment of one atom, another vector is considered, the magnetization vector which is a average of the magnetic moments over a small volume. It is a continuous theory meaning that the magnetization vector, note we speak about magnetization vector and not magnetic moment, varies continuously within a magnetic material. Moreover, the magnetization magnitude is kept constant in time in the usual frameworks.

Exchange energy

It is a short range energy between close neighbors. In most cases, its result is to favor parallel alignment of neighbors moments. In a ferromagnetic material, the exchange energy favors moments with a same direction and therefore uniform magnetization. In an antiferromagnetic material, exchange energy favors anti-parallel orientation of magnetic moments. Let us now make the link between the atomistic and micromagnetic models. In the Heisenberg model the exchange between two neighbor moments is :

$$\mathcal{E}_{12} = -J\mathbf{S}_1.\mathbf{S}_2 \tag{1.1}$$

with $J > 0$ for ferromagnetic materials and $J < 0$ for antiferromagnetic materials. To link the Ising model to the continuous theory, we use, as an example, the one-dimensional case of a spins whose only parameter is the angle θ. The scalar product between the two magnetic moments gives rise to a small variation of θ, $\delta\theta$ (Figure 1.1a). A continuous and smooth variation of the orientation of the magnetization between neighbors allows to write the expansion of the energy to the second order in θ:

$$\begin{aligned}
\mathcal{E}_{12} &= -J\mathbf{S}_1.\mathbf{S}_2 \\
&= -JS^2\cos(\theta_1-\theta_2) \\
&= -JS^2\cos(\delta\theta) \\
&\cong -JS^2\left[1-\frac{\delta\theta^2}{2}\right] \\
&= C + JS^2\frac{\delta\theta^2}{2}
\end{aligned} \tag{1.2}$$

Thus, removing the constant that is only an offset, the calculations leads to:

$$\begin{aligned}
\mathcal{E}_{12} &= \frac{1}{2}JS^2a^2\left(\frac{\delta\theta}{a}\right)^2, \quad \text{where } a \text{ is the distance between the spins} \\
\mathcal{E}_{12} \text{ vs } \mathcal{E}_{\text{ex}} &= \frac{JS^2a^2}{2}\left(\frac{\mathrm{d}\theta}{\mathrm{d}x}\right)^2 \\
&= \underbrace{\frac{JS^2}{2a}}_{A}\ a^3\left(\frac{\partial\theta}{\partial x}\right)^2
\end{aligned}$$

For a 3D case, we first need a volume normalization $\mathcal{E}_{\text{ex}}/a^3 = (JS^2/2a)(\partial\theta/\partial x)^2$. Moreover, since spins can also point along the three directions of space, and vary along the three directions. Thus the exchange energy volume density is written:

$$E_{\text{ex}} = A(\nabla\mathbf{m})^2 \tag{1.3}$$

where $\mathbf{m}$ is the magnetization vector and $(\nabla\mathbf{m})^2$ stands for $\Sigma_i\Sigma_j(\partial m_i/\partial x_j)^2$. A is the exchange stiffness and $A \cong JS^2/2a$, its unit is J/m. For most of the materials discussed in this thesis, Fe and Ni, A is of the order of 10^{-11} J/m.

Magnetocristalline anisotropy energy

This energy arises from the difference of direction between the magnetization and crystalline directions of the solid. This effect comes from crystal-field effects (coupling electron orbitals with the lattice) and spin-orbit effects as most of the magnetization in 3d metals arises from the spin. Some crystalline directions are more favorable than others so that the effect of the magnetocrystalline energy is to align the magnetization with one of them. There are also easy planes and to the contrary, hard axis along which alignment of the magnetization is prohibitively costly. E_{mc} is a function of the type $Kf(\theta,\varphi)$ with f a dimensionless function. Only even terms are considered for the suitability of the time-reversal symmetry. For an hexagonal symmetry:

$$E_{\text{mc,hex}} = K_1\sin^2\theta + K_2\sin^4\theta + ... \tag{1.4}$$

where θ is the angle between $\mathbf{M}$ and the c axis of the hexagonal lattice (see Figure 1.1b). With hexagonal symmetry, anisotropy is mostly uniaxial. For simple consideration, in many cases one considers a second-order uniaxial energy:

$$E_{\text{mc}} = K_{\text{u}}\sin^2\theta \tag{1.5}$$

Uniaxial anisotropy can may originate from sample shape or from material composition. Shape anisotropy comes from dipolar field as will be discussed in the following (sec Dipolar or

magnetostatic energy). In that case, uniaxial anisotropy is not an intrinsic property as it depends on sample shape. Material composition can also induce such anisotropy. For example, annealing permalloy can create an atomic-scale texture which produces a weak uniaxial anisotropy.

Zeeman energy

The Zeeman energy is the energy of a system in an external magnetic field. Minimization of this energy tends to align magnetic moments along the applied magnetic field $\mathbf{H}_{\text{ext}}$. The volume density of this energy is given by:

$$E_{\text{Z}} = -\mu_0 \mathbf{M}.\mathbf{H}_{\text{ext}} \tag{1.6}$$

This term contributes to the system's energy similarly to the pV term in the enthalpy defined in thermodynamics as $H = U + pV$, where U is the internal energy, p the external pressure and V the volume of the system. Within the same principle that a system under pressure reduces its size and increases its energy, a magnetic moment tends to align along the field and reduces its energy (through damping, for example). Enthalpy for a system under a magnetic field is $H = U - \mu_0 \mathbf{M}.\mathbf{H}_{\text{ext}} + pV$, thus the Zeeman energy adds a term to the enthalpy and in this sense is an external energy.

Dipolar or magnetostatic energy

The two names, dipolar or magnetostatic, are equivalent and both will be used in this manuscript. The dipolar energy has the same physical origin as the Zeeman energy, however it does not imply an applied field but the dipolar field $\mathbf{H}_{\text{d}}$ of the magnetic moments of the system itself.

$$\mathcal{E}_{\text{d}} = -\frac{\mu_0}{2} \iiint_V \mathbf{M}.\mathbf{H}_{\text{d}} \mathrm{d}V \tag{1.7}$$

The $\frac{1}{2}$ factor comes from the mutual feature of this energy and prevents from double counting. We define the dipolar constant $K_{\text{d}} = \frac{1}{2}\mu_0 M_{\text{s}}^2$.

For a given distribution of $\mathbf{M}$, it is therefore necessary to know the resulting distribution of $\mathbf{H}_{\text{d}}$ to evaluate $\mathcal{E}_{\text{d}}$. To do this, one solution is an analogy with electrostatics, considering magnetic charges. These are pseudo-charges and are not to be linked with particles like electrons in electrostatics as they are the source of $\mathbf{H}_{\text{d}}$, not of $\mathbf{B}$ the magnetic induction. According to the Maxwell equation $\operatorname{div} \mathbf{B} = 0$ (no magnetic monopole), the relationship between the magnetic field and magnetic induction is:

$$\mathbf{B} = \mu_0(\mathbf{H}_{\text{d}} + \mathbf{M}) \tag{1.8}$$

and then

$$\operatorname{div} \mathbf{H}_{\text{d}} = -\operatorname{div} \mathbf{M} \tag{1.9}$$

To compute the dipolar energy in practice, a method consists in using the magnetic scalar potential ϕ_{d}, derived from the dipolar field $\mathbf{H}_{\text{d}} = -\mathbf{grad}\ \phi_{\text{d}}$. We note $\rho = -\operatorname{div} \mathbf{M}$ the volume charges and $\sigma = \mathbf{M}.\mathbf{n}$ the surface charges ($\mathbf{n}$ being the outward normal to the surface of the volume) so that ϕ_{d} is:

$$\phi_{\text{d}}(\mathbf{r}) = \iiint \frac{\rho(\mathbf{u})}{4\pi\|\mathbf{r}-\mathbf{u}\|}\ \mathrm{d}V_u + \oiint_{\partial V} \frac{\sigma(\mathbf{u})}{4\pi\|\mathbf{r}-\mathbf{u}\|} \mathrm{d}S_u \tag{1.10}$$

With this formula for the magnetic potential, the dipolar energy is:

$$\mathcal{E}_{\text{d}} = \frac{1}{2}\mu_0 \left(\iiint_V \rho\phi_{\text{d}} \mathrm{d}V + \oiint_{\partial V} \sigma\phi_{\text{d}} \mathrm{d}S \right) \tag{1.11}$$

This latter equation highlights the fact that the effect of the dipolar energy is to tend to reduce the volume and surface charges of system, even to free the system from charges if only the dipolar energy is considered.

To deal with the magnetostatic energy, we can use the formalism of demagnetizing factors. This formalism uses the strong hypothesis that $\mathbf{M}$ is uniform, so that is there is no divergence, $\mathbf{M} = \Sigma_{i=1}^{3} M_i \mathbf{u}_i$. The dipolar field is then given by:

$$\mathbf{H}_{\mathrm{d}}(\mathbf{r}) = \Sigma_{i=1}^{3} M_i \iint \frac{(\mathbf{u}_i \cdot \mathbf{n}')(\mathbf{r}-\mathbf{r}')}{4\pi\|\mathbf{r}-\mathbf{r}'\|^3} \, \mathrm{d}S' \tag{1.12}$$

so that the dipolar energy is:

$$\begin{aligned} \mathcal{E}_{\mathrm{d}} &= -\iiint \frac{1}{2}\mu_0 M_i M_j \, \mathrm{d}V \iint \frac{(\mathbf{u}_i \cdot \mathbf{n}')(\mathbf{r}-\mathbf{r}')}{4\pi\|\mathbf{r}-\mathbf{r}'\|^3} \, \mathrm{d}S' \\ &= K_{\mathrm{d}}(N_{ij} \, m_i \, m_j)V \ , \ m_i = \frac{M_i}{M_{\mathrm{s}}} \end{aligned} \tag{1.13}$$

where N_{ij} are geometrical coefficients in the range $[0, 1]$. Let us define the demagnetizing field which is the dipolar field within a system. There is no approximation in these calculations. We can write:

$$< \mathbf{H}_{\mathrm{d}} >= -\overline{\overline{N}} \, \mathbf{M} \tag{1.14}$$

where $\overline{\overline{N}}$ and $\mathbf{M}$ are the demagnetizing tensor and the magnetization vector, and $< \mathbf{H}_{\mathrm{d}} >$ the volume average of $\mathbf{H}_{\mathrm{d}}$, which for most geometries is not uniform. For the $\overline{\overline{N}}$ matrix, $\mathrm{Tr}(\overline{\overline{N}}) = 1$. Moreover, it is always possible to diagonalize this matrix so as to find three main axes. The only cases where the demagnetizing field is perfectly homogeneous are the ellipsoids, cylinders, slabs,... If we take the example of the cube, axes are equivalent so that $N_x = N_y = N_z = 1/3$ and the dipolar energy is $\mathcal{E}_{\mathrm{d}} = K_{\mathrm{d}} \frac{1}{3}(m_x^2 + m_y^2 + m_z^2) = \frac{K_{\mathrm{d}} V}{3}$

Let us now take the example of an infinite cylinder along the z axis. Thus there is no end charges and the demagnetizing factor N_z along z is zero. To follow the rule $\mathrm{Tr}(\overline{\overline{N}}) = 1$, $N_x + N_y = 1$. Moreover, x and y directions are equivalent for the cylinder so demagnetizing factors along x and y are equal, $N_x = N_y = 1/2$. Thus in a cylinder, the magnetization is along the axis direction where the demagnetizing factor is zero, creating as less charges as possible. This is what is called sample shape effect.

When magnetization is not uniform, the evaluation of $\mathbf{H}_{\mathrm{d}}$ and $\mathcal{E}_{\mathrm{d}}$ is the most computational time consuming among all energies since there is interaction of all the magnetic moments of a system between each other.

1.1.2 Characteristic lengths

When dealing with real systems, in many cases, several energies compete. Take the example of a system with a magnetocrystalline anisotropy and a domain wall. Within the domain, magnetization is aligned with the easy axis. This is no more the case in the wall. The magnetocrystalline anisotropy tends to decrease the width of a wall, so as to decrease the length over which magnetization is not aligned along an easy axis, implying a cost of energy. However a sharp rotation increases the exchange energy (larger angle between two neighboring moments). In such systems, we define $\Delta_{\mathrm{u}} = \sqrt{\frac{A}{K}}$. This is the length over which the magnetization can rotate away from the easy axis. This length is called anisotropy exchange length. It is also called Bloch parameter or wall width. For hard magnetic materials K is high whereas it is small for soft magnetic materials. As a result, Δ_{u} ranges from 1 nm (*e.g.* $SmCo_5$) to 1 µm (*e.g.* $Fe_{20}Ni_{80}$).

For cases dipolar and exchange energies compete, the characteristic length is the dipolar exchange length and is given by: $\Delta_{\mathrm{d}} = \sqrt{\frac{2A}{\mu_0 M_{\mathrm{s}}^2}}$. This quantity is the relevant one to consider as

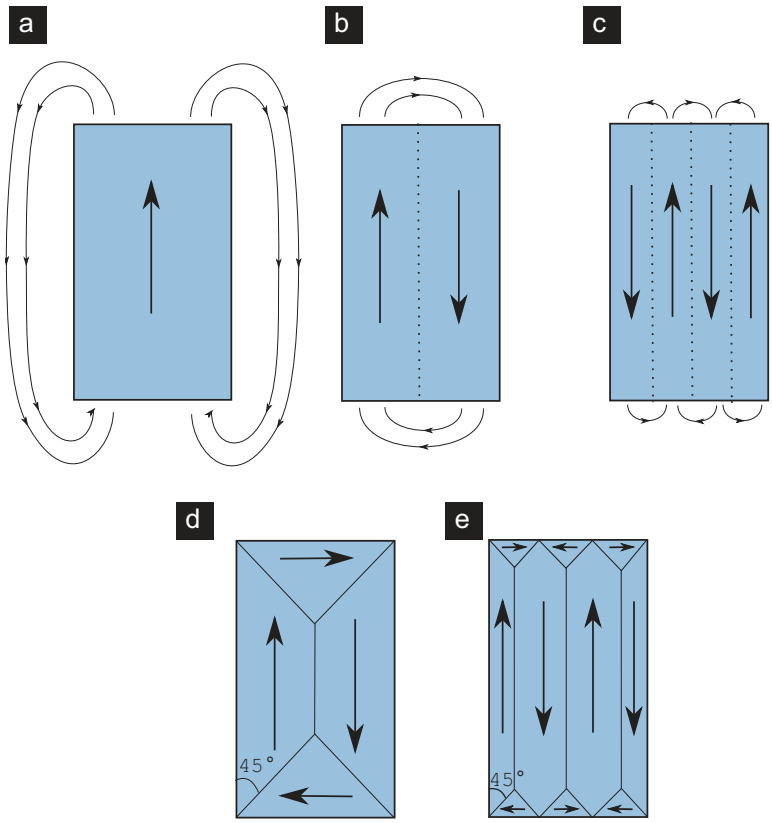

FIGURE 1.2: **Schematic for domains.** Sketches for (a)-(c) open domains, (d)-(e) perfect flux-closure domains.

the critical single-domain size for soft magnetic material (see 1.1.3). It is also called exchange length. A and M_s are rather similar for common soft magnetic materials thus the order of magnitude for Δ_d is 3 to 5 nm. However in a ferrimagnetic garnet, $M_s = 1/100\ M_{s,Fe}$ so that $\Delta_{d,garnet} \sim$ hundreds of nanometers.

1.1.3 Critical single-domain size

In this section we are looking for the critical size under which a sample is uniformly magnetized. Over this size, domain walls are created for a better flux-closure (Figure 1.2). Consider a sample with a compact structure, of lateral size R, demagnetizing coefficients N are thus 1/3. We define l_{SD}, the critical single domain size. Estimation of the critical single domain size depends on whether the material is soft or hard. Here we deal only with soft magnetic materials for which the magnetization rotates gradually, that is a collective magnetization distribution. To determine l_{SD}, the relevant quantities are the dipolar and exchange energies so that l_{SD} is expected to be linked with the dipolar exchange length Δ_d. Under l_{SD}, energy $\mathcal{E}_{SD}$ of a uniformly magnetized system is nearly NK_dR^3.

For soft magnetic materials, the volume density of exchange energy scales like $E_{ex} = A\left(\frac{\pi}{2R}\right)^2$ thus the exchange energy $\mathcal{E}_{ex} \sim AR$. To find the critical single domain size, we solve $\mathcal{E}_{ex} \cong \mathcal{E}_{SD}$ that is $AR \cong NK_dR^3$ thus $R \cong 1/\sqrt{N}\sqrt{A/K_d}$

In the case of a cube, simulations give the result of $l_{SD} \approx 7\Delta_d$ whereas for spheres, $l_{SD} \approx 4\Delta_d$ [14]. However l_{SD} is more difficult to estimate for non-compact systems such as wires or strips. We can take the example of a disk and estimate the transition between the uniform case (Figure 1.3a) and the vortex state (Figure 1.3b). The total energy of the uniform state is $\mathcal{E}_{SD} \approx NK_dtd^2$, with d the diameter and t the thickness. The in-plane demagnetizing factor is $\sim t/d$. A rough estimation of the energy $\mathcal{E}$ of the vortex state takes into account the dipolar

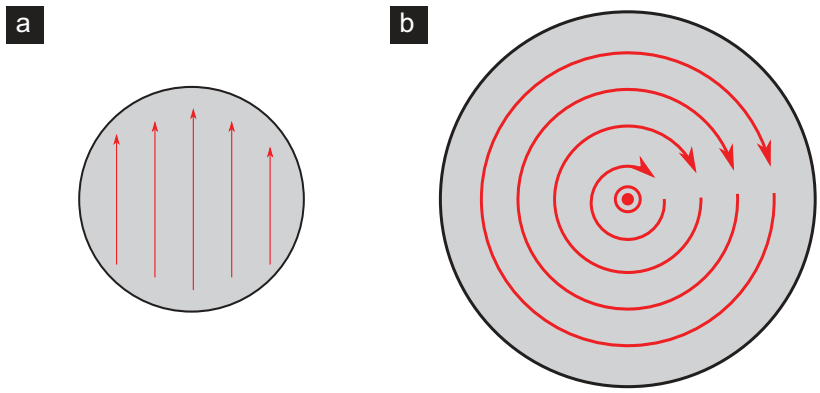

FIGURE 1.3: **Schematic for the magnetization in a disk** (a) Uniform state for small R. (b) Vortex state for large R.

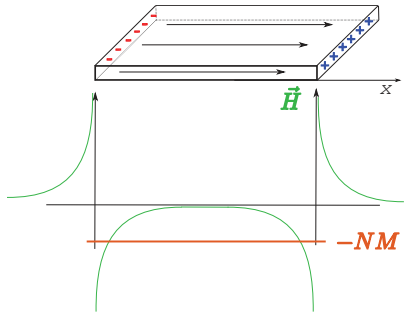

FIGURE 1.4: **Schematic for the demagnetizing field in a finite strip**.

and exchange energies: $\mathcal{E}_{\mathrm{V}} \sim 10\Delta_{\mathrm{d}}^2 t K_{\mathrm{d}} \sim At$. Finally, the critical single domain size is found with the equality $\mathcal{E}_{\mathrm{SD}} = \mathcal{E}_{\mathrm{V}}$ leading to $td = 10\Delta_{\mathrm{d}}^2$. Numerical simulations yielded a change of state for $td = 20\Delta_{\mathrm{d}}^2$ [15], which is of the same order or magnitude but refines the result.

However, even under the critical size l_{SD}, samples may not be perfectly uniformly magnetized. A demagnetizing field homogeneous and aligned with the uniform magnetization is valid only for ellipsoid, infinite cylinder with elliptical cross-section, slabs with infinite lateral dimensions, which is not the case when dealing with strips and wires. If we take the example of a thin film element, the demagnetizing field is highly inhomogeneous (see Figure 1.4). In the middle of the strip, it is lower than the average value $< \mathbf{H}_{\mathrm{d}} >= -\overline{\overline{N}}\,\mathbf{M}$ (see equation 1.14) while it is very high at the edges (up to $M_{\mathrm{s}}/2$). This field creates a torque on the magnetization at the edges giving rise to areas called end domains. In elongated systems, these domains may assume either an 'S' or a 'C' shape (Figure 1.5a,b). Another type of end domain is the curling which is a method to close the magnetic flux, and decrease magnetostatic energy. It is also named circulation of magnetization. Circulation is equivalent to curling which refers to the curl operator and is related to the circulation of the magnetization along a close path (Stokes theorem). The name curling was also used in the reversal mode and nucleation theory (see sec.1.1.4). Thus it is not only an equilibrium state but can also be a transient one. More details about the circulation of the magnetization can be found in chap.2. For more compact systems, these end domains are flower or leaf states (Figure 1.5c,d).

1.1.4 Reversal modes

In this section we present reversal modes for systems for which the demagnetizing field may be homogeneous and collinear so that no spatially dependent torque acts on the magnetization. The simplest mode keeps $\mathbf{M}$ uniform during the rotation (Figure 1.6b). This model of coherent

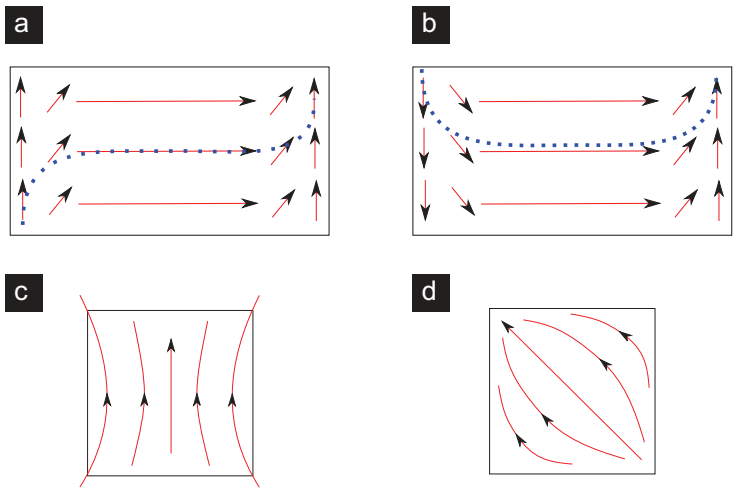

FIGURE 1.5: **Schematic for the end domains due to the demagnetizing field.** (a) 'S' state. (b) 'C' state. (c) Flower state. (d) Leaf state.

rotation was proposed by Stoner and Wohlfarth in 1948 to describe the angular dependence of the magnetization reversal [16, 17]. This model is valid under the strong hypothesis of a uniform magnetization. With such hypothesis, the model is applicable to very small particles only. However it has some generalities (exponents, angular dependance) applicable with care to larger systems.

In the following, we will try to describe reversal modes for large systems where the demagnetizing field is not homogeneous. The key term of the magnetization reversal is the energy barrier.

Under an applied field, for sufficiently large systems (see sec.1.1.3), the magnetization may deviate from the uniform state. Notice also that a system can be uniform in statics but this does not mean its reversal is uniform. Various models have been proposed to describe non-uniform magnetization switching. These models are extreme cases which are not necessarily the most relevant experimentally. Here we deal only with the case of wires. The first reversal mode is the magnetization curling (Figure 1.6a). This reversal mode starts with an orthoradial curling around the initial direction of magnetization (along the cylinder axis) giving rise to some vorticity. The angle between the moment direction and the cylinder axis is solely a function of the radius solely thus there is only one degree of freedom [18]. Since the magnetization is parallel to the lateral surface of the cylinder, there are no surface charges. However the system pays exchange over the diameter. The second mode is the magnetization buckling that is a periodic deviation of the magnetization from its initial direction, along the wire axis (Figure 1.6c).

Let us define the parameter $\rho = R/\Delta_{\mathrm{d}}$. For the case of an infinite cylinder, if $\rho < 1.1$ buckling is the favored mechanism, for $\rho > 1.1$ it is the curling and the rotation in unison (Stoner-Wohlfarth model) occurs for dimensions $\rho \ll 1$. Calculations can be found in the paper of E. H. Frei *et al.* [18]

1.1.5 Landau-Lifshitz-Gilbert equation

Now that we have detailed static or quasistatic magnetic aspects, we can then deal about magnetization dynamics which becomes precessional at nanosecond time scale. Let us start with a magnetic moment $\boldsymbol{\mu}$ (see Figure 1.7a).

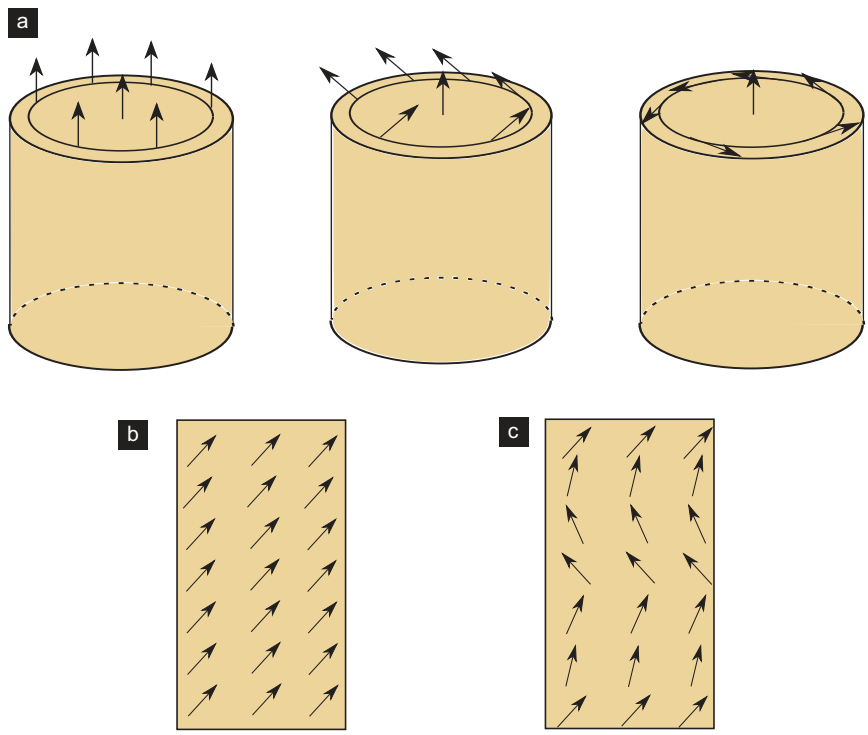

FIGURE 1.6: **Schematic for curling reversal in a wire**.(a) Magnetization curling. (b) Spin rotation in unison or coherent rotation. (c) Magnetization buckling

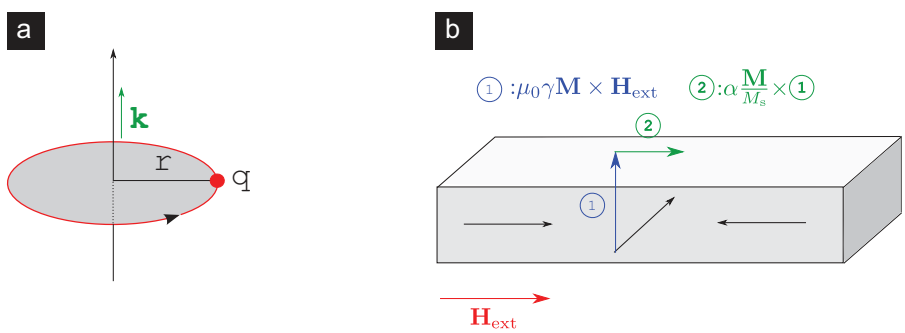

FIGURE 1.7: **Schematics for the LLG section**.(a) Scheme for the angular moment of a magnetic moment. (b) Description of the different terms of the LLG equation. The first term $\mu_0\gamma\mathbf{M}\times\mathbf{H}_{\mathrm{ext}}$ rotates the magnetization out of the plane of the domain wall and induces a precession of the magnetization around the applied magnetic field. The second term $\alpha\frac{\mathbf{M}}{M_s}\times\frac{\mathrm{d}\mathbf{M}}{\mathrm{d}t}$ tilts the magnetization and leads to the motion of the domain wall.

$$\begin{aligned}
\boldsymbol{\mu} &= I\mathbf{S} \text{ with } \mathbf{S} \text{ the vector area normal to the loop of current} \\
\boldsymbol{\mu} &= \frac{q}{2\pi r/v}\pi r^2\mathbf{k} \\
\boldsymbol{\mu} &= \frac{q}{2m}\boldsymbol{\ell}
\end{aligned}$$

with $\boldsymbol{\ell} = m\mathbf{r} \times \mathbf{v}$ is the angular momentum for a point particle. From quantum mechanics, the angular momentum is quantized with $\hbar$ thus the Bohr magneton is quantized with $(e/2m_\mathrm{e})\hbar$. More generally, we define $\gamma = gq/2m$ the gyromagnetic ratio with g the Landé factor ($g = 2$ for spin) so that $\boldsymbol{\mu} = \gamma\boldsymbol{\ell}$. As indicated at the beginning, we are interested in the time evolution of the magnetic moment under an applied field. Mechanics governs the time evolution of the angular moment, giving rise to $\boldsymbol{\mu}$:

$$\begin{aligned}
\frac{\mathrm{d}\boldsymbol{\ell}}{\mathrm{d}t} &= \boldsymbol{\mu} \times \mu_0\mathbf{H} \\
\frac{\mathrm{d}\boldsymbol{\mu}}{\mathrm{d}t} &= \boldsymbol{\mu} \times \mu_0\gamma\mathbf{H}
\end{aligned}$$

Notice that $\gamma < 0$ for an electron. This equation stands for a single magnetic moment. However, we are in the framework of micromagnetism, the magnetization $\mathbf{M}$ is the average over a small volume. This leads to the so-called called Landau-Lifshitz equation [19]:

$$\frac{\mathrm{d}\mathbf{M}}{\mathrm{d}t} = \gamma\mu_0\mathbf{M} \times \mathbf{H} \tag{1.15}$$

For a field applied along the z direction, the time derivative of the three components of the magnetization are :

$$\begin{cases}
\dot{m}_x &= +\mu_0\gamma m_y H \\
\dot{m}_y &= -\mu_0\gamma m_x H \\
\dot{m}_z &= 0
\end{cases} \tag{1.16}$$

Derivative of the z-component of the magnetization shows that the trajectory is energy conservative and thus it is a purely precessional movement. However it was observed in matter that magnetic moments lose energy and there is some damping of the magnetization dynamic. Moreover, as in quasistatics, in the end the magnetization is parallel to the applied field. To account for this, a phenomenological term was added by Gilbert [20] $\alpha\mathbf{M}/M_\mathrm{s} \times \mathrm{d}\mathbf{M}/\mathrm{d}t$ which dissipates energy. Finally, the time evolution equation is the Landau Lifchitz Gilbert equation (Figure 1.7b):

$$\frac{\mathrm{d}\mathbf{M}}{\mathrm{d}t} = \underbrace{\mu_0\gamma\mathbf{M} \times \mathbf{H}}_{\text{precession}} + \underbrace{\alpha\frac{\mathbf{M}}{M_\mathrm{s}} \times \frac{\mathrm{d}\mathbf{M}}{\mathrm{d}t}}_{\text{damping}} \tag{1.17}$$

α is the damping parameter. It is an dimensionless term of the order of 10^{-3} to 10^{-2} in most systems, so that in practice many precessions occur before the system is at rest. The experimental technique called FerroMagnetic Resonance allows to estimate the value of α .

1.2 Domain walls in one-dimensional systems

1.2.1 General features of domain walls

Bloch versus Néel wall

There are various reasons for a sample to be divided into domains. It may happen in order to decrease its energy, limiting charges and stray field (see Figure 1.2). Creation of domains may

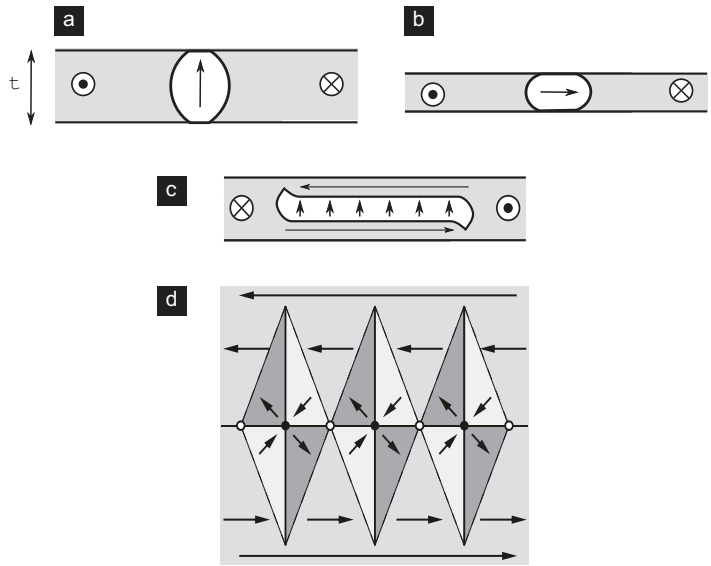

FIGURE 1.8: **Domain walls in thin film.** (a) Bloch wall. (b) Néel wall. (c) Bloch wall with a Néel cap. (d) Cross-tie wall

also come from history of the sample. All these reasons boil down to minimizing energy to the lowest energy state or metastable state. At areas separating these domains, domain walls are located.

For very thin film, magnetization is parallel to the surface (Figure 1.8b). Although this configuration gives rise to volume charges, there is no surface charge given by $\mathbf{M}.\mathbf{n}$, where $\mathbf{n}$ is the outward normal to the surface. This is the Néel wall. For thicker films, magnetization lies in the plane of the domain wall so $-\mathrm{div}\,\mathbf{M} = 0$. There are no volume charges but surface charges. This DW is called Bloch wall. The case of very thick film is a combination of both Bloch and Néel type (Figure 1.8c). The Bloch wall lies in the bulk whereas the rotation of the magnetization at the surface towards a Néel cap limits surface charges. If we note t the thickness of the film then for $t \gtrsim \Delta_\mathrm{u}$, the Bloch domain wall (Figure 1.8a) is favored whereas for $t \lesssim \Delta_\mathrm{u}$ it is the Néel wall which is favored.

Angle of walls

Domains and domain walls are 3D objects thus the domain walls are limited by planes defining the shape of the domain wall. Generally these planes tend to bisect magnetization in each domain to avoid locally net charges. Let us take a head-to-head DW as in Figure 1.9. Surface charges on the planes defining the DW are given by the scalar product $\mathbf{M}.\mathbf{n}$. First let us have a look at the left part of the DW $\mathbf{M}_1.\mathbf{n}_{12} = (1/\sqrt{2})M_\mathrm{s}$ and $\mathbf{M}_2.\mathbf{n}_{21} = -(1/\sqrt{2})M_\mathrm{s}$. Second, on the right part we have $\mathbf{M}_3.\mathbf{n}_{32} = (1/\sqrt{2})M_\mathrm{s}$ and $\mathbf{M}_2.\mathbf{n}_{23} = -(1/\sqrt{2})M_\mathrm{s}$. Hence we see this configuration of the planes gives rise to no net charges.

Cross-tie domain wall

As said above, the domain wall direction tends to bisect that of magnetization in neighboring domains. Thus unstable 180 ° Néel wall can be replaced by composite domain walls with smaller angle even if this implies an increase of the total domain wall length. An example of these composite DWs is the cross-tie wall. This domain wall occurs only in soft magnetic materials where no increase of anisotropy energy is induced. Note that 180 ° Bloch walls are replaced with cross-tie for thickness larger than that predicted for the cross-over between Bloch and Néel walls.

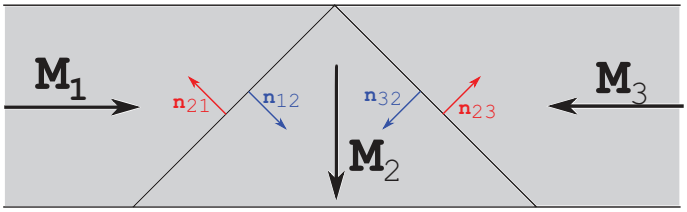

FIGURE 1.9: **Scheme for the planes delimiting the TW.** Black arrow are the magnetization vectors, red and blue arrows are the normal to the surface of the planes delimiting the TW.

FIGURE 1.10: **Scheme of a TW in a 1D system.** The colors indicates the magnetization direction along the z axis.

1.2.2 One dimensional model - The Bloch domain wall

Let us now turn to a 1D model which we can describe using previously addressed concepts, as an application of what has been explained before.

Magnetization profile

Let us consider a system whose magnetization varies along the x-axis as a chain of spins. The magnetization profile of this system may be described by one variable, the angle θ between the magnetization direction and the x-axis (Figure 1.11). This model was described by Bloch [21] with the boundary conditions $\theta(x = \pm\infty) \equiv 0 \mod \pi$. Within the Bloch domain wall, the magnetization lies in the plane of the domain wall thus without dipolar field. Two energies then compete, exchange energy and anisotropy energy which is assumed to be uniaxial for the simplest case.

The total energy is given by:

$$E = A\left(\frac{\mathrm{d}\theta}{\mathrm{d}x}\right)^2 + K_\mathrm{u}\sin^2\theta \tag{1.18}$$

It is possible to determine the profile of the 1D domain wall minimizing this energy. The exact profile is given by minimization of the total energy, making use of the Euler-Lagrange equation:

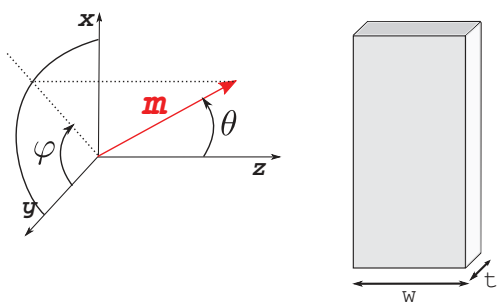

FIGURE 1.11: **Definition of the axis and the strips orientation**

$$\frac{\partial E}{\partial \theta} = \frac{\mathrm{d}}{\mathrm{d}x}\left[\frac{\partial E}{\partial(\frac{\mathrm{d}\theta}{\mathrm{d}x})}\right] \tag{1.19}$$

Applying this energy minimization to Eq. 1.18 leads to:

$$A\frac{\mathrm{d}^2\theta}{\mathrm{d}x^2} = K_\mathrm{u}\sin\theta\cos\theta \tag{1.20}$$

Mutliplying Eq. 1.20 by $\mathrm{d}\theta/\mathrm{d}x$ and integrating with the conditions $\mathrm{d}\theta/\mathrm{d}x(\infty) = 0$ and $\theta(\infty) = 0$, we get:

$$A\left(\frac{\mathrm{d}\theta}{\mathrm{d}x}\right)^2 = K_\mathrm{u}\sin^2\theta \tag{1.21a}$$

$$\mathrm{d}x = \pm\sqrt{\frac{A}{K_\mathrm{u}}}\frac{\mathrm{d}\theta}{\sin\theta} \tag{1.21b}$$

This is valid for systems of infinite size. Integration of this equation gives rise to the following solutions:

$$\begin{gathered}\theta(x) = 0 \text{ and } \theta(x) = \pi \\ \theta(x) = \pm 2\mathrm{Arctan}\left[\exp\left(\frac{x-q}{\Delta}\right)\right]\end{gathered} \tag{1.22}$$

which can be written in term of components of the magnetization along both axes:

$$m_x = \tanh(x/\Delta) \text{ and } m_\mathrm{t} = 1/\cosh(x/\Delta) \tag{1.23}$$

q is the integration constant corresponding to the position of the DW center along the x axis, and Δ the domain wall width or Bloch parameter defined previously(sec.1.1.2). The system can be uniformly magnetized in one direction or the other (the first two solutions) or there can be a DW of either circulation (the two other degenerate solutions).

In 1D systems, a transverse anisotropy can be responsible of a dipolar field and is of the form:

$$K_0\sin^2\theta\cos^2\varphi \tag{1.24}$$

φ defining the orientation of magnetization in space. Minimization of the energy, taking into account this new rotation in space, leads to $\mathrm{d}\varphi/\mathrm{d}x = 0$ and $\varphi(x) = C^\mathrm{ste}$ set by anisotropy, or as we will see later, reflect dynamic conditions.

Energy

As can be seen from Eq. 1.21a, for all positions x, exchange and anisotropy energies are equal, meaning there is an equipartition of the energy at any part. Thus to calculate the total energy of the system, only one of either energies needs to be integrated twice:

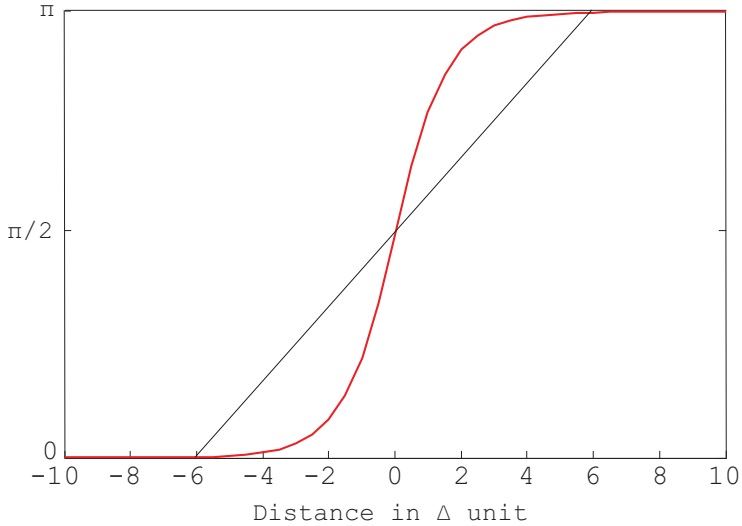

FIGURE 1.12: **Domain wall width.** Domain wall profile given by equation 1.22. Exact solution for the profile of the Bloch domain wall (red line) and the lowest-energy solution of the variational model in black line.

$$
\begin{aligned}
\mathcal{E} &= 2\int_{-\infty}^{+\infty} A(\mathrm{d}\theta/\mathrm{d}x)^2 \,\mathrm{d}x \\
&= 2\int_{-\infty}^{+\infty} E_\mathrm{a} \,\mathrm{d}x \\
&= 2\int_{-\infty}^{+\infty} \sqrt{E_\mathrm{a}(\theta)A\left(\frac{\mathrm{d}\theta}{\mathrm{d}x}\right)^2} \,\mathrm{d}x \\
&= 2\int_{-\infty}^{+\infty} \sqrt{E_\mathrm{a}(\theta)A}\frac{\mathrm{d}\theta}{\mathrm{d}x} \,\mathrm{d}x \\
&= 2\int_{\theta(x=-\infty)}^{\theta(x=+\infty)} \sqrt{E_\mathrm{a}(\theta)A} \,\mathrm{d}\theta \\
&= 2\sqrt{A}\int_{\theta(x=-\infty)}^{\theta(x=+\infty)} \sqrt{K_\mathrm{u}+K_0}\sin\theta \,\mathrm{d}\theta \\
\mathcal{E} &= 4\sqrt{A(K_\mathrm{u}+K_0)} \qquad (1.25)
\end{aligned}
$$

Width

There exists several definitions of the domain wall width. A first method is based on the intercept between asymptotes of the $\theta(x)$ function in the domain and in the wall (Figure 1.12). Lilley [22] proposed a definition for any functional of anisotropy however there exists simple formula for common anisotropies. For example, for the common case of uniaxial anisotropy this definition leads to $W_{\mathrm{L,uni}} = \pi\sqrt{A/K_\mathrm{u}} = \pi\Delta_\mathrm{u}$. Another method uses the asymptotes of the $\cos\theta(x)$ function, related to the magnetization within the domains and their intersection with tangent of the curve at DW center. The width is then $W = 2\sqrt{A/K_\mathrm{u}}$. Another series of definitions is based on integration rather than tangent. First, this can be applied to more general cases than to simple uniaxial anisotropy. Second, it is less sensitive to noise, as all data points are taken into account: $W_\mathrm{J} = \int_{-\infty}^{+\infty}\sin^2[\theta(x)]\mathrm{d}x$. The flux of magnetization may also be used in the integral and the width is $W_\mathrm{F} = \int_{-\infty}^{+\infty}\sin[\theta(x)]\mathrm{d}x$.

A third definition was proposed by Thiele [23], and is more relevant for DW under precession, as will be discussed below, $W_\mathrm{T} = 2S/\int_{-\infty}^{+\infty} \left|\frac{\mathrm{d}\mathbf{m}}{\mathrm{d}x}\right|^2 \mathrm{d}x$.

Dynamics

Even when dealing with simple one-dimensional systems, solving a functional with the LLG equation is too complex. Instead, the problem may be reduced to describe the DW with three parameters only: the domain wall center position along the system axis q, the DW width Δ and the azimuthal angle of the DW ϕ [21] (see Figure 1.11 for the angle definition). With these three parameters it is possible to describe the time-evolution of the magnetization profile:

$$\theta(x,t) = 2\mathrm{Arctan}\left[\exp\left(\frac{x-q(t)}{\Delta(t)}\right)\right] \tag{1.26a}$$

$$\varphi(x,t) = \phi(t) \tag{1.26b}$$

Slonczewski proposed a simple view of the dynamic of a DW under field [24]. This method consists in projecting the LLG equation (1.17) onto the longitudinal and transverse axis. The system of equation takes into account the time evolution of the wall width Δ. This leads to:

$$\alpha\frac{\dot{q}}{\Delta} + \dot{\phi} = \gamma_0 H_\mathrm{ext} \tag{1.27a}$$

$$\frac{\dot{q}}{\Delta} - \alpha\dot{\phi} = \gamma_0 H_\mathrm{K}\frac{\sin 2\phi}{2} \tag{1.27b}$$

$$\dot{\Delta} = \frac{12\gamma_0}{\alpha\mu_0 M_\mathrm{s}\pi^2}\left[\frac{A}{\Delta} - (K_\mathrm{u} - K_0\sin^2\phi)\Delta\right] \tag{1.27c}$$

K_0 is the first perpendicular anisotropy constant and K_u is the longitudinal anisotropy constant.

This last equation shows that the DW width evolves with a steady-state value,

$$\Delta = \sqrt{\frac{A}{K_\mathrm{u} + K_0\sin^2\phi}} = \frac{\Delta_0}{\sqrt{1+\kappa\sin^2\phi}}, \quad \text{with } \Delta_0 = \sqrt{\frac{A}{K_\mathrm{u}}} \tag{1.28}$$

Δ_u is the anisotropy exchange length and $\kappa = K_0/K_\mathrm{u}$. When some anisotropy is present in the system, the mobility depends on the applied field. Walker introduced [25] a field called Walker field $H_\mathrm{W} = \alpha H_\mathrm{K}/2$, with H_K the anisotropy field. Under this value, the speed increases linearly with the applied field. This regime is a steady-state DW motion. The wall velocity is:

$$\dot{q} = \gamma_0\Delta(\phi)H_\mathrm{a}/\alpha \tag{1.29}$$

Below the Walker field, the speed is thus proportional to $1/\alpha$. Above the Walker field, there is no longer a steady-state value for the angle ϕ. Instead, the DW undergoes a periodic angular precession. Because of the anisotropy term, this precession is not linear and the velocity scales like α.

1.2.3 Domain walls in strips

I designate by strip systems with a rectangular and rather flat cross-section. In strips the known domain walls are the transverse wall (TW) (Figure 1.13a) and the vortex wall (VW) (Figure 1.13b) as first described by R. McMichael and M. Donahue [27]. In both cases, magnetization remains mostly in plane.

The transverse wall (Figure 1.13a) has been given this name because magnetization lies in plane along the direction transverse to the strip. Its shape is roughly triangular in order to form globally uncharged 90° walls and reduce the magnetostatic energy.

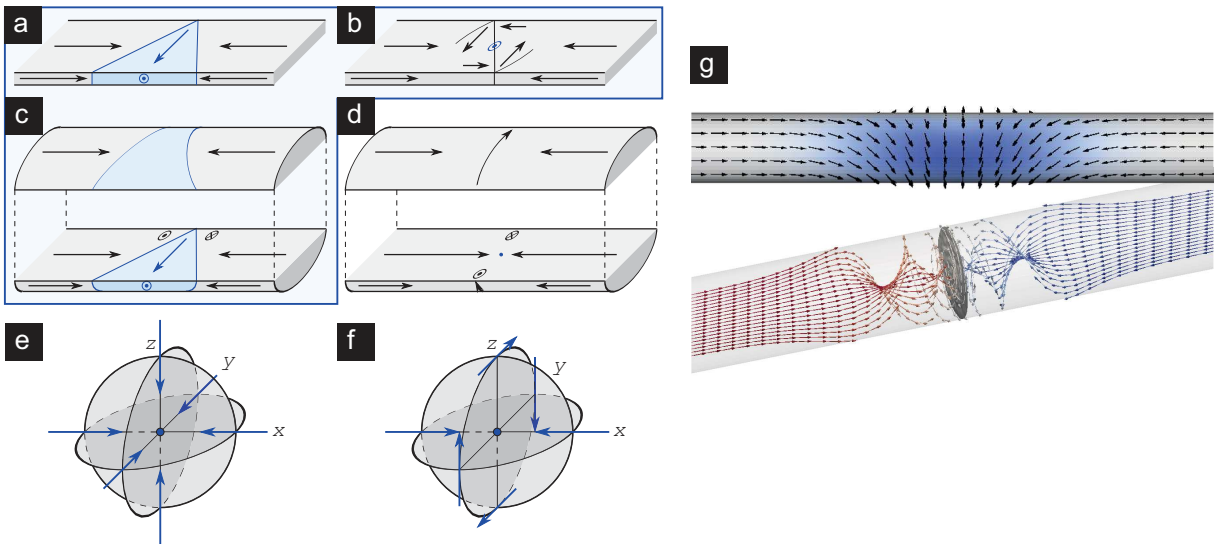

FIGURE 1.13: **Domain walls in 1D systems.** (a) Transverse wall in strip. (b) Vortex wall in strip. (c) Transverse wall in wire. (d) Bloch point wall in wire. (e)-(f) Bloch points of type hedgehog and curling. (g) Bloch point wall: surface magnetization presented with black arrows (top) and magnetization flux in the volume (bottom).

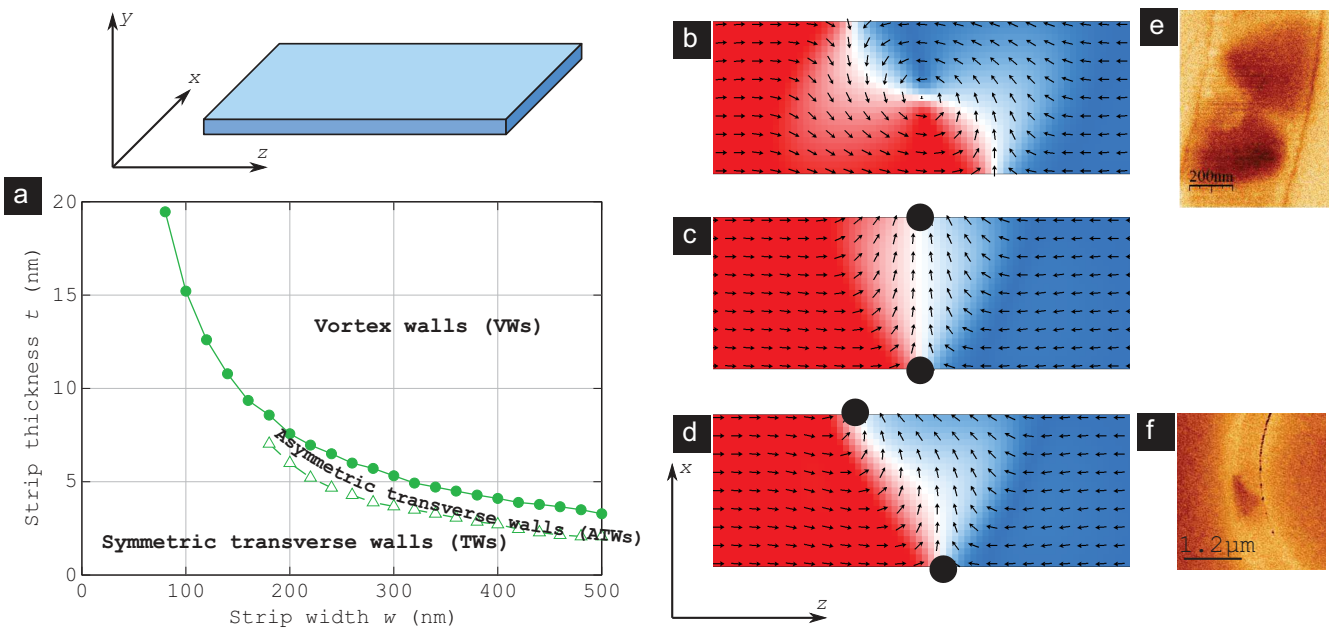

FIGURE 1.14: **Domain wall in strips - Simulations.** (a) Known phase diagram for strips. Full green dots are for first-order phase transition between the VW and the TW. Green triangles are for second-order phase transition between TW and ATW [3]. Micromagnetic configuration of a (b) VW, (c) TW and (d) ATW. The dark dots on (c) and (d) locate the entry and exit places of the magnetic flux. The right column is MFM images of (e) a VW and (f) a ATW [26].

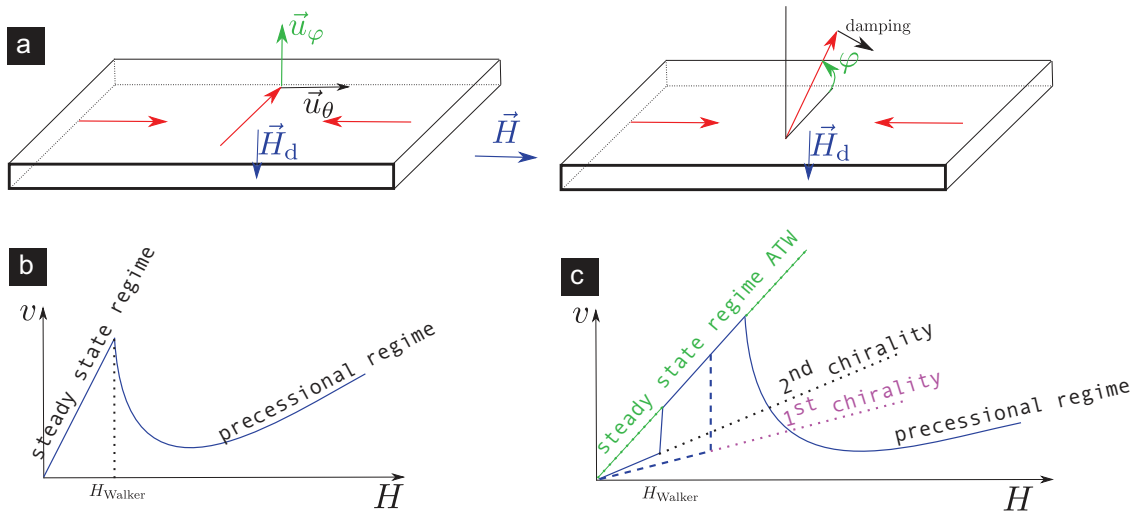

FIGURE 1.15: **Domain wall motion in strips** (a) Fields acting on the magnetization leading to the propagation of the DW. The red arrows are the magnetization vector. The field is applied along the strip length. First the torque between the applied field and the magnetization tilts the magnetization out of plane. Then, due to the damping, the magnetization is tilted along the strip length leading to the propagation of the DW. (b) $v = f(H_\mathrm{ext})$ for a TW. There are two modes, a steady state regime with a mobility proportional to $1/\alpha$ below H_W and a precessional regime above it, with a mobility proportional to α. (c) $v = f(H_\mathrm{ext})$ for a VW. There are three regimes. First a regime where the VW propagates with a mobility related to its chirality, second, the regime of the ATW after the transformation of the VW into a ATW and third a precessional regime.

For the VW (Figure 1.13b), magnetization rotates around a small area called the vortex core and of dimensions $\sim 3\Delta_\mathrm{d}$. The fine structure of a VW shows $90\,^\circ$ sub-walls.

For all soft ferromagnetic materials, the magnetic configuration is determined by a competition between exchange and magnetostatic energies. At low dimensions, simulation shows that for a thickness t and a width w such that $tw \lesssim 61\Delta_\mathrm{d}^2$, the TW is lower in energy than the VW. Thus this is the ground state. With increasing dimensions, magnetostatic energy prevails due to a larger cross-section and VW is more favorable. No transverse flux is leaking and head-to-head charges are more spread out. However the two DWs remain metastable on either sides of the transition, characterizing a first order phase transition. A later refined study [3] showed a transition of TW for large width from a symmetric shape to an asymmetric one (Figure 1.14a). This type of DW is named asymmetric transverse wall (ATW). A micromagnetic configuration of this DW is presented on Figure 1.14d. Since there is no metastability for the transition between symmetric and asymmetric TW, it is a second order phase transition. This type of DW has been observed experimentally (Figure 1.14f) [26].

Domain wall dynamics can be studied using either a magnetic field or through injection of an electric current. First, let us deal with the transverse wall (Figure 1.15a-b). A magnetic field induces a precession of magnetization around this field. This precession is responsible for a demagnetizing field stopping precession around the applied field and thus for the propagation of the DW to a speed proportional to $1/\alpha$ (see 1.29).

For high magnetic field, magnetic configuration starts to be non uniform along the width of the strip, defining the Walker field of the DW. Instead of a uniform precession of the DW core, an antivortex is injected in the wall, from one edge of the strip. It goes through the strip, reversing the direction of the transverse component. Since this antivortex costs less in energy than the precession of the magnetization of the anticore, the Walker field in a strip is lower than the predictions of the 1d model. Second, let us consider dynamics of vortex wall (Figure 1.15c). In the first stage, instead of a precession of magnetization around the direction of propagation,

the vortex core is laterally displaced, depending on chirality. For large enough field, once the vortex core is expelled from the strip, the configuration is the one of a ATW. Then the behavior of the DW is the one of the TW above the Walker field, with a vortex instead of an antivortex.

Similarly, a DW is propagated through injection of an electric current. LLG equation Eq. 1.17 is modified with the addition of two terms. Let us define $\mathbf{u}$ such that:

$$u = \frac{JPg\mu_{\mathrm{B}}}{2eM_{\mathrm{s}}}$$

with J is the spin polarized current density, P is the polarization and $g\mu_{\mathrm{B}}/2$ is the magnetic moment of the electron spin. Modified LLG equation reads:

$$\frac{\mathrm{d}\mathbf{M}}{\mathrm{d}t} = \mu_0\gamma\mathbf{M}\times\mathbf{H} + \alpha\frac{\mathbf{M}}{M_{\mathrm{s}}}\times\frac{\mathrm{d}\mathbf{M}}{\mathrm{d}t} - (\mathbf{u}.\nabla)\mathbf{M} + \beta\mathbf{M}\times[(\mathbf{u}.\nabla)\mathbf{M}] \tag{1.30}$$

The first added term is derived from the local form of the adiabatic spin transfer [28]. The second term is a phenomenological non-adiabatic term [29]. β is a dimensionless constant of the same order of magnitude as α. Through an injected current the DW is propagated with the adiabatic spin transfer torque in the direction of the electron flow. As with a magnetic field, the damping (α) tends to make magnetization precess around the propagation direction. To the contrary, the non-adiabatic spin transfer (β) leads to a precession in the other way. Combination of these two terms results in a torque (only if $\alpha \neq \beta$) acting like a magnetic field, inducing a speed proportional to β/α at high current. Thus, for $\beta > \alpha$, such as for permalloy, the behavior of a domain wall is similar as under field. These theoretical predictions have been confirmed experimentally.

1.2.4 Domain walls in wires: theory

I name wires compact systems with a disk or square cross-section.

Transverse vortex wall

In nanowires, it has been predicted that there exists a DW similar to the TW (Figure 1.13c) found in strips and also called transverse since the main component of the wall is perpendicular to the wire axis. At small diameters the configuration of this TW is close to the one-dimensional model (Figure 1.10). This type of domain wall is the most stable for diameter below $\approx 7\Delta_{\mathrm{d}}$.

Let us now discuss the dynamics of the TW. The 1D model (1.27), under the hypothesis of a uniform magnetization across the section, provides a qualitative approximation of DW dynamics. This approximation becomes more and more quantitative at small diameter. Indeed, in this case magnetization does not have the freedom to rotate within the cross-section, since it is prohibitively costly in exchange energy. Without perpendicular anisotropy (see 1.28), DW width is fixed, proportional to Δ_0. For this case, angular and longitudinal propagation speeds under magnetic field reach a steady state.

$$\dot{\phi} = \frac{1}{1+\alpha^2}\gamma_0 H_{\mathrm{a}} \tag{1.31a}$$

$$\dot{q} = \frac{\alpha}{1+\alpha^2}\gamma_0\Delta_0 H_{\mathrm{a}} \tag{1.31b}$$

Since $\alpha \ll 1$, mobility is similar to 1D DW far above Walker field, approximately $\alpha\gamma_0\Delta_0 H_{\mathrm{a}}$ whereas the angular speed is circa $\gamma_0 H_{\mathrm{a}}$. Let us take the example of Permalloy ($\alpha \approx 10^{-2}$), with a 35 nm-wire-diameter with an applied field of 5 mT:

$$\dot{\phi} = \frac{1}{1+10^{-4}} \times 2.21.10^5 \times 5.10^{-3} \cong 1.1 \times 10^2 \,\mathrm{rad.\,sec}^{-1} \tag{1.32}$$

$$\dot{q} = \frac{10^{-2}}{1+10^{-4}} \times 2.21.10^5 \times \sqrt{\frac{10^{-11}}{1/2 \times 1.050}} \times 5.10^{-3} = 4.8 \times 10^{-5}\mathrm{m.\,sec}^{-1} \tag{1.33}$$

Bloch point wall

Another type of DW that does not exist in strips has been predicted in wires. The main feature of this second type of domain wall (Figure 1.13d-g) is the curling of magnetization. The third dimension allows for a circulation of magnetization around the wire axis, enabling a flux-closure. This is made possible at somewhat large diameter, making the cost of exchange energy acceptable when compared with the cost in magnetostatic energy.

Topology of this domain wall is different from all others. Indeed, let us consider $\mathbf{M}.\mathbf{n}$, the surface charge density. The transverse flux of transverse wall leads to $\pm M_\mathrm{s}$ at entering (-) and exit points (+) of flux. For the BPW, magnetization remains mostly parallel at any point of the surface. As a consequence, if we consider the $M_x = 0$ surface, due curling within this surface, the M_y and M_z components must also vanish in one point. Thus, all three components of $\mathbf{M}$ must vanish. This object is called Bloch point and was predicted early in the theory of magnetism [30, 31] and its existence was suspected from examination of boundary conditions at surfaces of 3D samples [24], then investigated numerically for disk [32, 33] and square [2] cross-sections. Two equivalent configurations at rest of a BPW are presented in Figure 1.13e,f. However, it will be explained hereafter these two configurations are not equivalent during steady state motion. The name of BPW was used by some authors ([34],[35]) to avoid any confusion with the VW in strips. BPW was found to be more stable than TVW for dimensions above $\approx 7\Delta_\mathrm{d}$, both for square and disk cross-sections [2].

A Bloch point wall can hold either a positive (head-to-head) or a negative (tail-to-tail) charge (Figure 1.16a) and for each charge there are two possible chiralities (Figure 1.16b). These four configurations are degenerated at steady state. Moreover, at the steady state, magnetization is radially tilted. Indeed, the head-to-head, or tail-to-tail charge, induces a demagnetizing field which acts as a torque on the radial component of the magnetization (Figure 1.16a). A positive charge tilts the magnetization away from the axis so as to reject the positive charges at the surface and decrease the overall magnetostatic energy of the domain wall. For a negative charge domain wall, it is the reverse.

The propagation of a BPW under a magnetic field works as follows. First the applied field exerts a torque on magnetization ($\gamma_0 \mathbf{m} \times \mathbf{H}$, 'precession' part of the equation 1.17). This torque induces a time-variation of magnetization so that another torque is applied ($\alpha \mathbf{m} \times \mathrm{d}\mathbf{m}/\mathrm{d}t$). In steady-state regime, both torques compensate each other. Similarly to dynamics in strips, the tilt of magnetization induces a demagnetizing field leading to a torque along the wire axis, propagating the domain wall. Chirality should be right with the direction of domain wall propagation, thus if the field is applied the other way, above a given applied field, chirality switches. This switching is clearly visible on the plot of the speed versus the applied field. For a circulation left with the applied field direction, speed is low (mobility very low) and above a given applied field, corresponding to the energy barrier needed to switch chirality, the speed increases sharply (large mobility) to reach the high speed regime (almost zero mobility) (see Figure 1.16d) highlighting the fact that the BPW releases spin waves. The Walker breakdown thus exhibits a higher value, larger than interesting fields used for propagation . This feature makes it a good candidate for magnetic memory devices.

An applied field can enhance or reduce the spiraling angle (Figure 1.16c). With a sufficient applied field, the dipolar field maintaining a given chirality of the BPW is outmatched so that

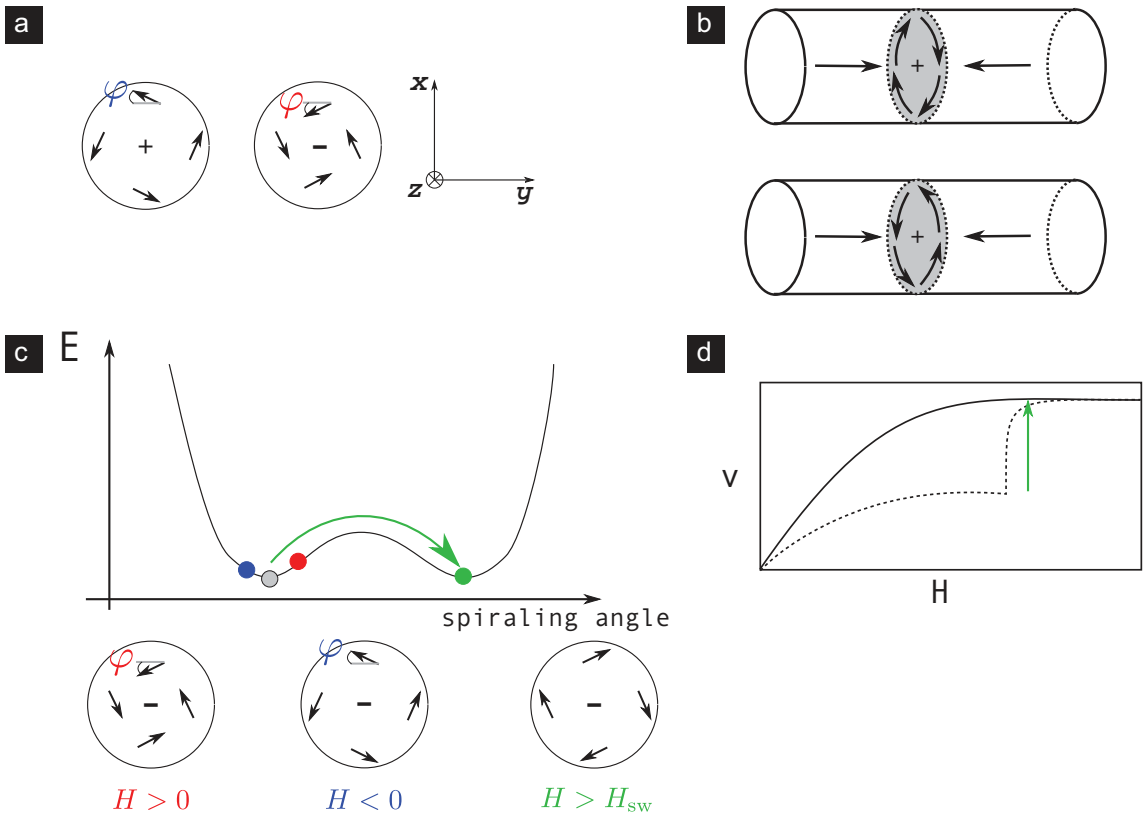

FIGURE 1.16: **Bloch point wall charge and chirality.** (a) Polarity of a Bloch point. (b) The two chiralities for a same polarity. (c) Effect of the applied field on the spiraling angle. (d) Speed versus applied field. Full line: the field compatible with the BPW with favored circulation. Dotted line: field with the unappropriated direction to propagate the BPW. The green arrow stands for the change of chirality.

the spiraling angle is not only slightly increased or reduced but the chirality is reversed (green arrow on Figure 1.16c and d).

The BPW does not enter standard micromagnetism theory with $|\mathbf{m} = 1|$, since magnetization vanishes at the Bloch point. This will raise some numerical problems as presented by Thiaville *et al.* in [36], such as a potential landscape arising from the mesh. Indeed, the center of each mesh cell is like a tiny potential barrier for the Bloch point. Thus, the system requires to be meshed with an even number of cells in every directions so that the Bloch point lies in the center of the sample.

A large number of publications considered magnetization reversal in magnetic nanowires. However, the vast majority is concerned with the full magnetization reversal, starting from nucleation and ending in fully-reversed wires. Thus, they do not deal with details of domain walls. Besides, only a handful of these considered single wires, while most consider large and dense arrays of wires. The most important experimental part concerns magnetization reversal, done through domain wall nucleation at one end of the wire.

Apart from our work to be reported in chapter 3, to my knowledge there exists only one report of the inner structure of a domain wall in cylindrical nanowires. It was based on electron holography, revealing a transverse wall, and was published in 2013 by Bizière *et al.* [37], during my PhD and slightly before our own manuscript reporting TW and BPW [8].

To conclude, DW dynamics in nanostrips and nanowires have both similarities and differences. In both cases, the dynamics of TW can be described using the 1D model presented in sec.1.2.2. Above a given field, called Walker field, the mobility drops. Then, a new regime starts where the transverse component of TW rotates around the axis of the strip and the width

oscillates. The speed of these domain walls is of several meters per second. The case of BPW, thus only for wires, is different. It is topologically protected and thus does not exhibit Walker breakdown. Its speed is predicted to reach almost 1 km/s. Under this field the velocity of the VW is lower than that of the TW because of energy dissipation at the vortex core. Above 9 mT, the vortex core is expelled due to the gyrotropic force, thus both velocities become similar. This marks the transition from symmetric TW to ATW.

1.3 Micromagnetism - Numerics

1.3.1 Overview of numerical simulations

In micromagnetism, except for simple systems, there are generally no analytical solutions. This lack of analytical solutions justifies the use of simulations to solve micromagnetic problems. There are several methods in numerical simulations to find the equilibrium state of a system.

First are Monte Carlo simulations. The system is randomly modified by changing the local magnetization at one site to obtain a new state. A variation of energy E is associated with this modification of magnetization. If the system reduces its energy, the new state is accepted. If the change increases energy of the system, the new state is accepted with a probability $P = \exp(\frac{-\Delta E}{k_\mathrm{B}T})$, with T is the temperature of the system and k_B is the Boltzmann constant. Such simulations can deal with nucleation and propagation of DWs through wires [38].

The second method is minimization of energy by using genetic algorithms [39]. The direction of magnetization is defined using Euler angles. Theses angles are coded on an integer. Each bit corresponds to one allele in genetics. We consider an ensemble of magnetic systems, each of their state being presented as a set of chromosomes. In genetic algorithm, each state is called population. Using operations such as crossover and mutations of genes in chromosomes within population, it is possible to reach the global minimum of the whole system.

The third one is the integration of the LLG equation (see equation 1.17). This latter technique enables to deal with terms that do not derivate from an energy such as the spin transfer torque. They are included in the effective field of the LLG equation 1.17. This later method also enables to describe precessional dynamics under field which is not properly described by the two former.

Let us now focus on LLG equation. Numerics requires the use of a discretization technique, both spatially and temporally. Regarding temporal discretization, it consists of a division of time into small time steps. At each step, the micromagnetic configuration is computed. In the following, we will write $\mathbf{m}^n$ the magnetization at time step n, and k the time step. A temporal scheme is of p-order if the local error from the exact solution is in $\mathcal{O}(k^{p+1})$. Thus, starting from the step 0, it is expected the overall error is in $\mathcal{O}(k^p)$. We are interested in a temporal scheme of order larger than one. Indeed, for a given time step, schemes of large order increase the accuracy of the solution. As a comparison, a Taylor expansion is closer to the solution when higher orders in the expansion are taken into account. First order can have only a tangential description, second order can describe parabola, and so on. A few schemes do not amplify error, they are said to be stable. To the contrary, numerically unstable schemes inject artificial energy which tends to destabilize the system. These systems cannot be used in practice and we will use only a stable scheme.

Spatial discretization can be of two types. Finite differences method uses a prismatic lattice mesh and fields are evaluated at nodes. Nodes correspond to a grid where are defined approximative values of the unknown of the equation. The unknown is sampled at the nodes of a grid. Discretization consists in substituting partial derivatives of the quantity by their Taylor expansions. This estimation at each node is obtained through a Taylor expansion of the unknown quantity from neighbor nodes. Thanks to the translational symmetry of the lattice it is possible to use Fast Fourier Transforms to compute demagnetizing field, which nevertheless remains the most time-consuming step. Moreover, thanks to the precision arising from the regular lattice,

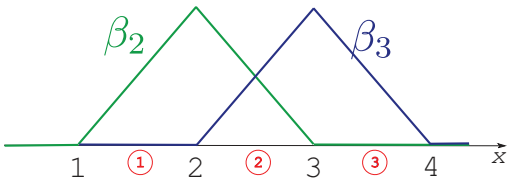

FIGURE 1.17: **Triangular functions and tangent plane.** (a) Triangular functions used for the interpolation of magnetization. In black are numbered the nodes of the mesh. The red rounded numbers stand for the cells. β_i are the triangular functions related the nodes i.

TABLE 1.1: **Advantages and disadvantages of the finite differences and finite elements methods.**

	Finite Difference Method	Finite Element Method
Advantages	- Mesh most often regular - Derivates evaluated at nodes → possibility to use the FFT method - Fine tuning of parameters to evaluate variations of the energy	- Systems with complex shapes thanks to mesh -Interpolation at each point in space (but $\lvert\mathbf{M}\rvert$ is not kept)
Weaknesses	- Only basic system shape	- No translational symmetry of the mesh→ not possible to use the FFT - Derivatives not defined at nodes

finite differences method is useful when we are interested in the estimation of the variation of the energy of a system according to various parameters, for instance, to build a phase diagram. Codes such as the public OOMMF and our own GL-FFT use these techniques [40, 41]. However this type of mesh can induce numerical anisotropy when it is used for systems with curved surfaces [42].

Finite element method (FEM) appears as a solution for these systems. The system is discretized into continuous polyhedrons (tetrahedron, prism, hexahedron), without overlap. Magnetization is sampled at each node of this mesh. Nodes correspond to the vertices of the polyhedrons. Inside each element, magnetization and its time derivative are linearly interpolated. The mesh can be either regular over the whole system or be refined around areas of interest such as boundaries. In our case, we use tetrahedrons, which fit curved systems better, and the mesh is regular over the whole system. The solution of LLG equation is searched within a space of continuous functions that are polynomial in each element (polyhedron). The LLG equation is not solved locally but with its integral form, the so-called weak formulation, relying on integration technique, such as the Gauss technique. Indeed, FEM is an integral method for which functions, such as magnetization, are assimilated to an operator associating a scalar product to a test function w. A test function, or projected function, is a function that is non-zero over the elements sharing a node (Figure 1.17a). The function space, the space of functions containing the solutions of the LLG equation, needs to be carefully chosen, taking into account the properties of magnetization and boundary conditions (natural conditions). As an example in micromagnetism, the time derivative of $\mathbf{m}$ must be orthogonal to $\mathbf{m}$ at nodes. According to the Galerkin method, the space of test functions corresponds to the space of solution functions. Moreover, FeeLLGood has been developed with, among others, the request that the magnetization norm is 1 and the system is stable, in other words, that is it dissipates energy. Advantages and disadvantages of the two methods are summarized in Table 1.1

In the following, we will use a finite element method. The use of a non-symmetric mesh with FEM makes the computing of demagnetizing field more complicated since it is no more possible to estimate the Laplacian of magnetization by Taylor expansion as used in the finite difference

approach. There are several other methods, and particularly multipole methods described in the following. Here is a non exhaustive list of micromagnetic codes: LLG Micromagnetics Simulator [43], Nmag [44], Vampire [45] and Mumax [46].

1.3.2 Methods to compute the demagnetizing field in FEM

The demagnetizing field is the most time-consuming step since it results from long range pair interaction involving all magnetic moments. Its direct calculation needs N^2 operations where N is the number of moments. In the continuous approach, there are several methods to compute this term. The idea is to deal first with the magnetic pseudo-potential ϕ_d:

$$-\Delta\phi_\mathrm{d} = -\nabla \cdot \mathbf{M} \tag{1.34}$$

which is continuous at the border ∂D of the sample and whose normal derivatives are subject to a jump condition across ∂D:

$$\left[\frac{\partial\phi_\mathrm{d}}{\partial n}\right] = -\mathbf{n} \cdot \mathbf{M} \tag{1.35}$$

The potential also is required to vanish at infinity.

A method to compute the potential is the one proposed by Fredkin *et al.* [47] and is based on the boundary integral method (BEM). The potential ϕ_d is written as the sum of two parts such that:

$$\phi_\mathrm{d} = \phi_\mathrm{d}^1 + \phi_\mathrm{d}^2 \tag{1.36}$$

where:

1. ϕ_d^1 only defined inside the sample is solution of the inhomogeneous Neumann problem:

$$-\Delta\phi_\mathrm{d}^1 = -\nabla \cdot \mathbf{M} \tag{1.37}$$

with the boundary condition:

$$\frac{\partial\phi_\mathrm{d}^1}{\partial n} = \mathbf{n} \cdot \mathbf{M} \tag{1.38}$$

2. ϕ_d^2, defined everywhere, is solution of the harmonic Laplace equation:

$$\Delta\phi_\mathrm{d}^2 = 0 \tag{1.39}$$

with the boundary condition:

$$[\phi_\mathrm{d}^2] = \phi_\mathrm{d}^1 \quad \text{and} \quad \left[\frac{\partial\phi_\mathrm{d}^2}{\partial n}\right] = 0 \tag{1.40}$$

In practice, ϕ_d^1 is first calculated by using a finite element calculation, then ϕ_d^2 is estimated by a boundary integral at every point of the bounded domain D:

$$\phi_\mathrm{d}^2 = \iint \phi_\mathrm{d}^1 \frac{\partial G}{\partial n}\,\mathrm{d}S \quad \text{with} \qquad G(\mathbf{r}) = -\frac{1}{2\pi}\ln|\mathbf{r}| \quad \text{in 2D} \tag{1.41}$$

$$\text{and} \qquad G(\mathbf{r}) = -\frac{1}{4\pi}\frac{1}{|\mathbf{r}|} \quad \text{in 3D} \tag{1.42}$$

ϕ_d^2 can be seen as a perturbation to the solution ϕ_d and corrects the result obtained at the first stage. This method prevents to mesh outside the sample, improving computing time which, however, remains of the order of $N^{4/3}$ in 3D where N is the number of calculation points. These

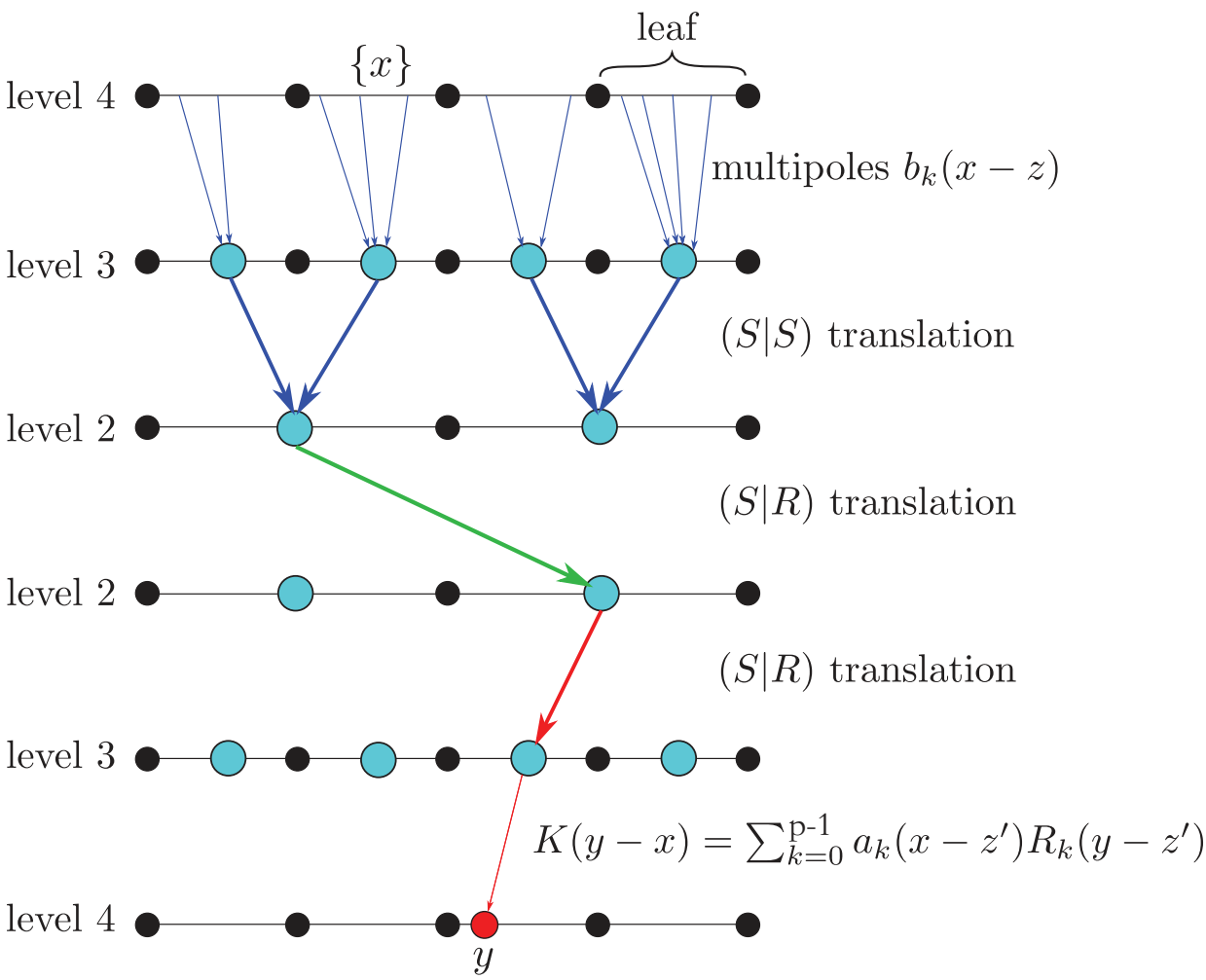

FIGURE 1.18: **Schematic for the Fast Multipole Method in one dimension.** The blue dots are the expansion centers. The arrows present the translations. This scheme is in 6 lines to make it clearer however, in the real space, all the lines are merged. At the top are the sources, $\{x\}$. The target y is at the bottom. The z and z' abscissae are the large blue dots. For the $(S|S)$ translations, z is the point of the high level ($e.g.$ level 3) and z' the point of lower level ($e.g.$ level 2). In case of $(S|R)$ translation it is the reverse. z' is the point of the high level ($e.g.$ level 3) and z the point of lower level ($e.g.$ level 2). For both types $(S|S)$ and $(R|R)$, translation is done from z to z'.

points can be either sources or targets. The second method, detailed in the following is more powerful. It is the one implemented in our code.

We use fast multipole methods for the fast computation of the demagnetizing field. Long range interactions are not sensitive to local variations of the magnetic potential. Thus contributions to this potential are grouped in boxes. These boxes are hierarchically ordered, each box containing information about smaller contained boxes. Thus for each place the magnetic potential is computed, contributions to the latter are not computed again for all sources.

The main idea of the fast multipole method (FMM) is to transform a node-to-node interaction into a cell-to-cell interaction. Each FMM-cell is divided until it contains at the most a defined number of nodes. Thus the system is put into a computation box which is divided into smaller and smaller boxes or segments, as presented in the 1D case in Figure 1.18. Two multipole methods exist, the hierarchical and the fast multipole methods. The first one is in $\mathcal{O}(N \log N)$, and the second, which is an improvement of the first one, is in $\mathcal{O}(N)$.

The computing of the magnetic pseudo-potential leading to the demagnetizing field is computing time-consuming. The idea is thus to use the Fast Multipole Method (FMM) to compute the magnetic pseudo-potential using a faster method:

$$\phi_{\mathrm{d}}(\mathbf{r}) = \sum_j \frac{q_j}{|\mathbf{r} - \mathbf{r}_j|} \tag{1.43}$$

In practice, the system is divided with a dyadic partition in order to get elements (segments in 1D, squares in 2D and cubes in 3D), containing a limited number of targets or sources. Within this partition, level n has 2^n cells along one direction. For each cell of level n and of center z, multipolar moments associated to z are calculated. Then information is propagated from level n to level $n-1$, writing the multipoles associated to the level $n-1$ as a function of those of level n and so on until level 2 (there is no level 1). The maximum number of elements a FMM-cell can contain is constrained. The system is then divided until boxes contain, at maximum, the defined number of elements. The next step is to propagate information towards the target (the place where we want to compute the magnetic potential). Using an identification between far field and near field expansion (detailed in the following), multipoles are translated from far cells to the cell containing the target.

For sake of simplicity, let us go deeper into the explanation of FMM and take the example of the Cauchy kernel to describe the potential. Even though it has no physical meaning, its writing down is easier than others with a logarithmic kernel for example. In one dimension, it reads:

$$K(y - x) = \frac{1}{y - x} \tag{1.44}$$

where sources are at positions x and targets y. Let us define the two notions of far field and near field expansions. For that, x and y are separated by a third point z, inducing a Taylor expansion depending on position z:

$$K(y - x) = \frac{1}{y - z + z - x} \tag{1.45}$$

Far field: Let us assume that z is close to x. Then the kernel becomes:

$$K(y - x) \cong \frac{1}{y - z} \sum_{k=0}^{p-1} \left(\frac{x - z}{y - z} \right)^k \tag{1.46}$$

by neglecting the terms of order larger than p. Convergence is possible for $\left| \frac{x-z}{y-z} \right| < 1$

Near field: in that case z is close to y:

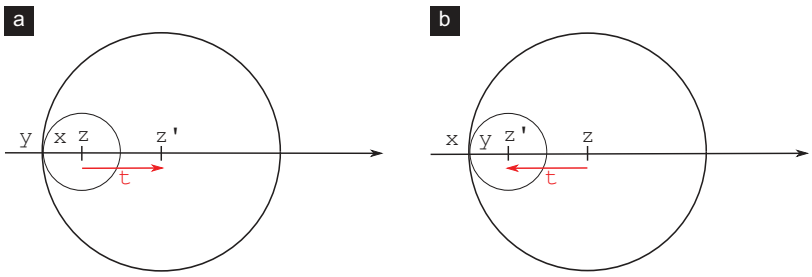

FIGURE 1.19: **Far field and near field translation.** t is the translation vector from z to z'. (a) Far field. $\{x\}$ is accessible after the translation. (b) Near field. $\{y\}$ is accessible after the translation.

$$K(y-x) \cong \frac{-1}{x-z}\sum_{k=0}^{p-1}\left(\frac{y-z}{x-z}\right)^k \tag{1.47}$$

after truncation. Convergence is possible for $\left|\frac{y-z}{x-z}\right| < 1$. In both cases, p is the order of the multipolar expansion.

As said above the first step is to write down multipoles, that is to say to transfer information from leaves to expansion points (from level 4 to level 3 in Figure 1.18). An expansion point is the center of a cell, collecting information from the higher level. This is done using a direct calculation. These multipoles are then translated from level n to level $n-1$. This translation, called multipole-multipole translation and written $(S|S)$ uses the far field expansion, so that:

$$\begin{aligned} K(y-x) &= \sum_{k=0}^{p-1}(x-z)^k\left(\frac{1}{y-z}\right)^{k+1} \\ &= \sum_{k=0}^{p-1}\underbrace{b_k(x-z)}_{\text{regular}}\underbrace{S_k(y-z)}_{\text{singular}} \end{aligned} \tag{1.48}$$

where the $b_k(x-z)$ are the multipole moments. To increase the convergence of the sequence, z the center of a cell of level $n-1$ is translated to z' at level n (Figure 1.19a). The new multipole, after the translation, is written $\tilde{b}_k(x-z')$ and can be written as a function of $b_k(x-z)$:

$$\begin{aligned} \tilde{b}_k(x-z') &= (x-z-t)^k = \sum_{m=0}^{k}\underbrace{\binom{k}{m}(-1)^{k-m}t^{k-m}}_{(S|S)}\underbrace{(x-z)^m}_{b_m(x-z)},\ t = z'-z \\ \tilde{b}_k(x-z') &= \sum_{m=0}^{k}(S|S)_{km}\ b_m(x-z) \end{aligned} \tag{1.49}$$

The following aspect of the expansion is the downward pass, that is to say the transfer from the expansion centers to the target, starting from cells of the lowest level (level 2). This expansion follows the same principle as the $(S|S)$ translation but in near field. They are called local-local translation and written $(R|R)$. Let start from the kernel and derive it:

$$\begin{aligned} K(y-x) &= -\sum_{k=0}^{p-1}\left(\frac{1}{x-z}\right)^{k+1}(y-z)^k \\ &= -\sum_{k=0}^{p-1}a_k(x-z)R_k(y-z) \end{aligned} \tag{1.50}$$

In the same manner, moments are translated from z to z' with z the center of the cell of level $n-1$ and z' the center of the cell of level n (Figure 1.19b):

$$
\begin{aligned}
K(y-x) &= \sum_{k=0}^{p-1} \tilde{a}_k(x-z')R_k(y-z') && (1.51)\\
\tilde{a}(x-z') &= \left(\frac{1}{x-z'}\right)^{k+1} = \left(\frac{1}{x-z-t}\right)^{k+1}, \; t = z'-z \\
\tilde{a}(x-z') &= \left(\frac{1}{x-z}\right)^{k+1} \left(\frac{1}{1-\frac{t}{x-z}}\right)^{k+1} \\
\tilde{a}(x-z') &= \sum_{m=k}^{p-1} \underbrace{\binom{k}{m} t^{m-k}}_{(R|R)} \underbrace{(x-z)^m}_{a_m(x-z)} \\
\tilde{a}(x-z') &= \sum_{m=k}^{p-1} \binom{k}{m} (R|R)\; a_m(x-z) && (1.52)
\end{aligned}
$$

Now we are able to translate moments from one level to another, for up and downward passes. The last step to explain is the transition from the $(S|S)$ to $(R|R)$ translations. The goal is the write the $a_k(x-z')$ from the $b_k(x-z)$, thus to equate far field and near field expansions.

$$
\begin{aligned}
\tilde{a}_k(x-z') &= \left(\frac{1}{x-z'}\right)^{k+1} = \left(\frac{-1}{t}\right)^{k+1} \left(\frac{1}{1-\frac{x-z}{t}}\right)^{k+1} \\
\tilde{a}_k(x-z') &= \sum_{m=0}^{p-1} (-1)^k \binom{m+k}{k} t^{-m-k-t}(x-z)^m \\
\tilde{a}_k(x-z') &= \sum_{m=0}^{p-1} (S|R)_{km}\; b_m(x-z) && (1.53)
\end{aligned}
$$

Standard calculation of the magnetic potential requires N^2 operations, if N is the number of sources and targets. Lets have a look at the number of required operations with FMM. For that, we discard the convergence radius of the sequence so that all sources and targets are considered. This explanation is based on the Figure 1.18:

$$
\begin{aligned}
Np + \sum_{k=0}^{p-1} k^2 + N \times 2^2 \times 2^2 p^2 + \sum_{k=0}^{p-1} + Np &= Np + \frac{N(p-1)p(2p-1)}{6} \\
&\quad + N \times 2^2 \times 2^2 p^2 + \frac{N(p-1)p(2p-1)}{6} + Np \quad (1.54)\\
&\propto N \quad (1.55)
\end{aligned}
$$

The most important point to decrease the number of operations is the $(S|R)$ translation. This translation plays the role of the 'middleman' through which all information passes.

1.3.3 The home-made finite element code FeeLLGood

This section is dedicated to the home-made finite element code FeeLLGood based on the integration of the LLG equation. First, I present the transformation of the LLG equation to the weak formulation used in the code.

Explicit scheme and weak formulation

The crucial property of the LLG equation is $\mathbf{m}.\frac{\mathrm{d}\mathbf{m}}{\mathrm{d}t} = 0$. The norm of magnetization is therefore fixed and $\frac{\mathrm{d}\mathbf{m}}{\mathrm{d}t}$ belongs to the tangent plane of $\mathbf{m}$. Let us go back to the LLG equation (1.17), in which the effective field may be split as:

$$\mathbf{H}_{\mathrm{eff}} = \mathbf{H}_{\mathrm{exc}} + \mathbf{H}_{\mathrm{d}} + \mathbf{H}_{\mathrm{ext}} + \mathbf{H}_{\mathrm{K}} \tag{1.56}$$

where $\mathbf{H}_{\mathrm{exc}}$ is the exchange field, $\mathbf{H}_{\mathrm{d}}$ is the dipolar field, $\mathbf{H}_{\mathrm{ext}}$ is the applied field and $\mathbf{H}_{\mathrm{K}}$ is the anisotropy field. With FEM, it is not possible to write the local expressions of the differential equation, the so-called strong formulation (it is not possible to derive used the functions at nodes). The equation is thus projected onto test functions (numerical approximation of a distribution function), giving rise to the weak formulation. A proper sum of weighted test functions is assumed to be a good approximation of the solution. All the code is based on test functions $\mathbf{w}_i$. They are linked to triangular functions that provide a spatial size. The vector gives the direction. This weak formulation is therefore used in FeeLLGood. For example, let us use the exchange field closely related to: $\mathbf{m}$: $\mathbf{H}_{\mathrm{exc}} = [(2A)/(\mu_0 M_{\mathrm{s}})]\,\Delta\mathbf{m}$. The constant $2A/\mu_0 M_{\mathrm{s}}$ is set to 1 for calculations and the LLG equation becomes:

$$\mathbf{v} = -\mathbf{m} \times \Delta\mathbf{m} + \alpha\mathbf{m} \times \mathbf{v} \tag{1.57}$$

where $\mathbf{v} = \mathrm{d}\mathbf{m}/\mathrm{d}t$ is the unknown variable. In cartesian coordinates, using Einstein notation:

$$\mathbf{v} = -\mathbf{m} \times \Delta m_i \mathbf{e}_i + \alpha\mathbf{m} \times \mathbf{v} \tag{1.58}$$

$$\mathbf{H}_{\mathrm{ex}} = \begin{cases} \Delta m_x \\ \Delta m_y \\ \Delta m_y \end{cases} \tag{1.59}$$

At this stage the goal is to rebuild a heat-like equation $\mathrm{d}T/\mathrm{d}t = D\Delta T$, so as to determine the exchange energy. This is achieved by doing the cross product "$\mathbf{m} \times \mathbf{LLG}$":

$$\begin{aligned} \mathbf{m} \times \mathbf{v} &= -\mathbf{m} \times (\mathbf{m} \times \mathbf{H}) + \alpha\mathbf{m} \times (\mathbf{m} \times \mathbf{v}) \\ \mathbf{m} \times \mathbf{v} &= -(\mathbf{m} \cdot \mathbf{H}) \cdot \mathbf{m} + \mathbf{H} + \alpha(\mathbf{m} \cdot \mathbf{v}) \cdot \mathbf{m} - \alpha\mathbf{v} \\ \alpha\mathbf{v} + \mathbf{m} \times \mathbf{v} &= \mathbf{H} - (\mathbf{m} \cdot \mathbf{H}) \cdot \mathbf{m} \end{aligned} \tag{1.60}$$

Let us concentrate on the exchange term of the latter equation: $\mathbf{m} \cdot \mathbf{H} = m_x \Delta m_x + m_y \Delta m_y + m_z \Delta m_z$ with $\Delta = \mathrm{div}\,(\mathbf{grad})$

$$\begin{aligned} \mathbf{m} \cdot \mathbf{H} &= m_i\ \partial_x^2 m_i + m_i\ \partial_y^2 m_i + m_i\ \partial_z^2 m_i \\ &= \underbrace{\partial_x(m_i\ \partial_x m_i)}_{=0} - (\partial_x m_i)(\partial_x m_i) \\ &+ \underbrace{\partial_y(m_i\ \partial_y m_i)}_{=0} - (\partial_y m_i)(\partial_y m_i) \\ &+ \underbrace{\partial_z(m_i\ \partial_z m_i)}_{=0} - (\partial_z m_i)(\partial_z m_i) \end{aligned} \tag{1.61}$$

Thus $\mathbf{m} \cdot \mathbf{H} = -(\vec{\nabla}\mathbf{m})^2$. If we go back to equation Eq. 1.60, we get:

$$\alpha\mathbf{v} + \mathbf{m} \times \mathbf{v} = \vec{\Delta}\mathbf{m} + \underbrace{(\vec{\nabla}\mathbf{m})^2}_{\text{Lagrange multiplier}} \mathbf{m} \tag{1.62}$$

The Lagrange multiplier is used to check whether time derivative of magnetization is still in the tangent plane. Since it is not possible to use local equations, weak (or projective) formulation

is required. An example of the types of function used to transform the formulation into a weak formulation is the distribution:

$$\Delta_{\mathbf{r}} f(\mathbf{r}) = \int \mathrm{d}^3\mathbf{r}\ \delta(\mathbf{r}-\mathbf{r}')\Delta_{\mathbf{r}'} f(\mathbf{r}') \tag{1.63}$$

The best numerical approximation of distribution function is triangular function β (Figure 1.17a) so that equation 1.63 becomes:

$$\Delta_{\mathbf{r}} f(\mathbf{r}) \to \int \mathrm{d}^3\mathbf{r}\ \beta_i(\mathbf{r}-\mathbf{r}')\Delta_{\mathbf{r}'} f(\mathbf{r}') \tag{1.64}$$

With finite element method the local formulation is turned into a weak formulation weighted with test functions β_i. To weigh these local equations we project equation onto vectorial functions, the $\mathbf{w}_i$ functions. Strong formulation 1.62 is transformed as follows:

$$\forall\ \mathbf{w} \perp \mathbf{m}\ ,\ \int \mathrm{d}^3\mathbf{r}\ \mathbf{w}.\alpha\mathbf{v} + \int \mathrm{d}^3\mathbf{r}\ \mathbf{w}.(\mathbf{m}\times\mathbf{v}) = \underbrace{\int \mathrm{d}^3\mathbf{r}\ \Delta m_i \mathbf{w}.\mathbf{e}_i}_{1} - \int \mathrm{d}^3\mathbf{r}\ (\mathbf{m}^n_\beta.\Delta m_i \mathbf{e}_i)\underbrace{\mathbf{m}_\beta.\mathbf{w}}_{=0} \tag{1.65}$$

There is no boundary conditions that only generate surface terms. Term 1 can be written as:

$$\begin{aligned}
\Delta m_\beta \mathbf{w}.\mathbf{e}_\beta &= \mathrm{div}(\nabla m_\beta) w_\beta \\
(\Delta m_\beta).w_\beta &= -\nabla m_\beta.\nabla w_\beta + \mathrm{div}(\mathbf{w}.\nabla m_\beta) \\
\int \mathrm{d}^3 r\ \Delta m_\beta.w_\beta &= -\int \mathrm{d}^3 r\ \nabla m_\beta.\nabla w_\beta + \oiint w_\beta \underbrace{\mathbf{n}.\nabla m_\beta\ \mathrm{d}\mathbf{S}}_{\frac{\partial \mathbf{m}}{\partial \mathbf{n}}=\mathbf{0}}
\end{aligned} \tag{1.66}$$

$$\int \alpha\mathbf{w}.\mathbf{v} + \int \mathbf{w}.(\mathbf{m}\times\mathbf{v}) = -\int \nabla w_\beta.\nabla m_\beta \tag{1.67}$$

Equation Eq. 6.3 is a typical weak formulation for an explicit scheme. Note that we take only the exchange into account. It is an integral form of LLG equation, weighted by test functions.

We discretize into time step t so that for all times t, there is an integer n such that $t = n/\Delta t$, this weak formulation, so that the explicit scheme becomes:

$$\int \alpha\mathbf{w}.\mathbf{v} + \int \mathbf{w}.(\mathbf{m}^n\times\mathbf{v}) = -\int \nabla w_\beta.\nabla m^n_\beta \tag{1.68}$$

Temporal scheme - θ-scheme

Starting from the weak formulation obtained above, the next step consists in setting up a temporal scheme. The time-derivative of magnetization is in fact different from $\mathbf{v} = \mathrm{d}\mathbf{m}/\mathrm{d}t$ since it is not possible to get $\mathrm{d}t \to 0$. Thus, we write $\Delta\mathbf{m}/\Delta t$. The explicit scheme (6.3) is associated with a stability condition of the type $\Delta t/(\Delta x)^2 < \rho_c$.

To stabilize the scheme, we derive a θ-scheme. This scheme follows the same idea as those derived for heat-like equation. However in the present case, the value of θ has nothing to do with the order of the method as it is in mechanics. Indeed, our method is a first order method since we removed the Lagrange multiplier. We thus have:

$$\int \alpha\mathbf{w}.\mathbf{v} + \int \mathbf{w}.(\mathbf{m}^n\times\mathbf{v}) = -\int \nabla w_\beta.\nabla m^{n,\theta}_\beta \tag{1.69}$$

with:

$$\begin{cases} \theta &= 1: \text{ implicit} \\ \theta &= 0: \text{ explicit} \end{cases}$$

$\theta = 1$ being equivalent to equation Eq. 1.68, and

$$\mathbf{m}^{n,\theta} = \mathbf{m}^n + \theta \mathbf{v} \Delta t, \ \theta \in [0,1]$$

Magnetization is normalized to 1 to follow the theory of micromagnetism. Magnetization we would like to be $\mathbf{m}^{n+1}$ is then:

$$\mathbf{m}^{n+1} = \frac{\mathbf{m}^{n,1}}{|\mathbf{m}^{n,1}|} = \frac{\mathbf{m}^n}{\sqrt{1 + v^2 \Delta t^2}}$$

Taking into account this scheme, LLG equation 1.68 is now:

$$\int \alpha \mathbf{w}.\mathbf{v} + \int \mathbf{w}.(\mathbf{m} \times \mathbf{v}) = -\int \nabla w_\beta . \nabla m_\beta^{n,\theta}$$

Error is in Δt^2 which is negligible since we consider first order. Thus, the formulation which is kept is:

$$\int \alpha \mathbf{w}.\mathbf{v} + \int \mathbf{w}(\mathbf{m} \times \mathbf{v}) + \theta \Delta t \int \nabla w_\beta . \nabla v_\beta = -\int \nabla w_\beta . \nabla m_\beta^n \tag{1.70}$$

Energy dissipation

For the system to relax towards equilibrium there is a need to dissipate energy, otherwise magnetization remains on iso-energy lines. If we take into account only exchange energy, to dissipate energy the weak formulation needs:

$$\begin{aligned} E^{n+1} - E^n &= \int |\nabla \mathbf{m}^{n+1}|^2 - \int |\nabla \mathbf{m}^n|^2 \\ &= 2\Delta t \int \nabla \mathbf{v}.\nabla \mathbf{m}^n + \Delta t^2 \int (\nabla \mathbf{v})^2 < 0 \end{aligned} \tag{1.71}$$

This is granted by the following relation, valid with a continuous scheme and under some conditions with a discrete scheme (Bartel's theorem):

$$\int |\nabla(\mathbf{m}^{n+1})|^2 \leq \int |\nabla(\mathbf{m}^{n,1})|^2 \tag{1.72}$$

For instance, for tetrahedrons, dihedral angles must be lower than $\pi/2$ and for a hexahedral mesh, prisms must be right. Now equation 1.71 is going to be written using only $\mathbf{v}$. If we replace $\mathbf{w}$ by $\mathbf{v}$ in equation 1.70, which is allowed since the time-derivative of magnetization and test functions come from the same function space:

$$\begin{aligned} \int \alpha v^2 + \theta \Delta t \int |\nabla(\mathbf{v})|^2 &= -\int \nabla v_\beta . \nabla m_\beta^n \\ \Delta E \leq -2\Delta t \left[\int \alpha v^2 + \theta \Delta t \int |\nabla(\mathbf{v})|^2 \right] &+ \Delta t^2 \int |\nabla \mathbf{v}|^2 \\ \Delta E \leq -2\Delta t \int \alpha v^2 + (1 - 2\theta) \Delta t^2 \int |\nabla(\mathbf{v})|^2 \end{aligned}$$

The first term of the right hand side is the physical dissipation of energy. This latter equation shows that:

- $\theta \geq 1/2$ the scheme is energetically stable whatever Δt is

- $\theta = 0$ the scheme is stable under conditions

In our simulations, we use $\theta = 1/2$ which is the most stable case. Because of the normalization of magnetization, it is possible to show that $\theta = 1/2$ does not correspond to a second-order scheme.

Tangent plane

From LLG equation 1.17, we can note that $\mathbf{m} \cdot \partial\mathbf{m}/\partial t = 0$, meaning the time derivative of $\mathbf{m}$ lies in the tangent plane of $\mathbf{m}$. This ensures that the norm of $\mathbf{m}$ is maintained during the time evolution. The use of the tangent plane was introduced by Alouges [48]. At each point the test function and the time derivative of the magnetization are orthogonal to the magnetization. This tangent plane is built at each step.

$$\begin{aligned} \mathbf{e}_\mathrm{p} &= \mathbf{r} \times \mathbf{m} \\ \mathbf{e}_\mathrm{q} &= \mathbf{m} \times \mathbf{e}_\mathrm{p} \end{aligned}$$

where $\mathbf{r}$ is the position vector. Thus $(\mathbf{m}, \mathbf{e}_\mathrm{p}, \mathbf{e}_\mathrm{q})$ is an orthogonal basis and $(\mathbf{e}_\mathrm{p}, \mathbf{e}_\mathrm{q})$ is the plane base.

In practice, to construct the system of linear equations from the Alouges equation 1.62, first there is a projection with vectorial function $\mathbf{w} = \beta_i \mathbf{e}_\mathrm{p}$ then $\mathbf{w} = \beta_i \mathbf{e}_\mathrm{q}$. Thus after assembling matrices, the system of linear equations has 2N equations with 2N unknown factors. At each node of the finite element mesh, times derivative of magnetization $\mathbf{v}$ has two scalar components $(v_\mathrm{p}, v_\mathrm{q})$.

1.3.4 Towards second order

As a reminder, we said that the θ-scheme does not signify a second order scheme due to the normalization of magnetization vector.

$$\alpha \int \mathbf{v}.\mathbf{w} + \int (\mathbf{m}^{n,\theta} \times \mathbf{v}).\mathbf{w} = \int \mathbf{H}^{n,\theta}.\mathbf{w} - \int \lambda^{n+\theta} \mathbf{m}^{n,\theta}.\mathbf{w} \tag{1.73}$$

where field at time n is $\mathbf{H}^{n,\theta} = \mathbf{H}^n_\mathrm{ext} + \theta \Delta t \vec{\Delta} \mathbf{v}$ and $\lambda = \mathbf{m} \cdot \mathbf{H}$ is the Lagrange multiplier. Then:

$$\int \mathbf{H}^{n,\theta}.\mathbf{w} = -\int \vec{\nabla}\mathbf{m}^n.\vec{\nabla}\mathbf{w} - \theta\Delta t \int \vec{\nabla}\mathbf{v}.\vec{\nabla}\mathbf{w} \tag{1.74}$$

Following the same principle as before, we get the following θ-scheme:

$$\begin{aligned} \alpha \int \mathbf{v}.\mathbf{w} + \int (\mathbf{m}^n \times \mathbf{v}).\mathbf{w} + \theta\Delta t \int \vec{\nabla}\mathbf{v}.\vec{\nabla}\mathbf{w} = & - \int \vec{\nabla}\mathbf{m}^n.\vec{\nabla}\mathbf{w} \\ & - \theta\Delta t \int \lambda^{n+\theta}\mathbf{v}.\mathbf{w} + \vartheta(\Delta t^2) \qquad (1.75) \\ & - \int \lambda^{n+\theta}\mathbf{m}^n.\mathbf{w} \qquad (1.76) \end{aligned}$$

The latter scheme is of $\vartheta(\Delta t^2)$ precision. It is possible to switch $\lambda^{n+\theta}$ to λ^n. To stabilize the scheme, λ is chosen so that $\lambda^n = \mathbf{H}^n_\mathrm{ext}.\mathbf{m}^n = -(\vec{\nabla}\mathbf{m}^n)^2$

We can write equation Eq. 1.75 in another form:

$$\int \left[(\alpha - \theta\Delta t(\vec{\nabla}.\mathbf{m}^n)^2\right] \mathbf{v}.\mathbf{w} + \int (\mathbf{m}^n \times \mathbf{v}).\mathbf{w} + \theta\Delta t \int \vec{\nabla}\mathbf{v}.\vec{\nabla}\mathbf{w} = -\int \vec{\nabla}\mathbf{m}^n.\vec{\nabla}\mathbf{w} \tag{1.77}$$

One possibility to get a unique solution for this equation is to keep $[(\alpha - \theta\Delta t(\vec{\nabla}.\mathbf{m}^n)^2] > 0$. A first solution is to limit Δt. A second solution is to define :

$$\tilde{\alpha} = \frac{\alpha}{1 + \frac{\theta\Delta t}{\alpha}(\vec{\nabla}.\mathbf{m})^2} \tag{1.78}$$

We chose this latter solution.

1.3.5 About the norm of the magnetization

Theory of conventional micromagnetism states that $|\mathbf{m}| = 1$. However, with FEM, magnetization is computed at nodes of tetrahedrons, thus implying that the norm is not conserved inside due to linear interpolation. In the same manner, the study of a Bloch point wall raises some problems. Indeed, theory does not include any point where magnetization vanishes. In practice, Bloch point is not well described by the FEM approach. One observes that it lies in the middle of a cell [36, 49] , as far as possible from nodes where magnetization is necessarily equal to 1.

Chapter 2

Phase diagram of domain walls: from nanostrips to nanowires

As seen previously (sec.1.2), DWs in strips are of two forms: transverse wall (TW) (Figure 2.1d) and vortex wall (VW) (Figure 2.1c), initially described by R. McMichael and M. Donahue [27]. Both types of DWs have a magnetic charge $2twM_s$ with t the thickness of the strip and w its width. TWs and VWs have been numerically investigated until $w = 500\,\mathrm{nm}$ and $t = 20\,\mathrm{nm}$ [3]. A later study [3] showed a transition of TW from a symmetric shape to an antisymmetric one (ATW) for large width. TW is of lower energy and thus more favourable than the VW for dimensions $tw \lesssim 61\Delta_d^2$. Regarding nanowires, simulations began later, pioneered by R. Hertel [33, 50] and H. Forster [32, 51]. In such geometries, there are, as in strips, TWs (see Figure 2.3) but also Bloch point walls (BPW) (see Figure 2.2d-g). Existence of the latter is made possible in nanowires of sufficient large diameter thanks to the larger third dimension compared to strips, enabling a flux-closure of magnetization.
A phase diagram is a two-dimension plot presenting areas of the domain walls of the lowest energy. Instead of presenting liquid, solid and gas phases in a (Pressure, Temperature) diagram, here phases are the different types of domain walls and (t, w) stands for (P, T). The two dimensions are thickness t and width w. Lines separating each zones on diagram are phase transition lines. DWs separated by these lines are of the same energy on lines.

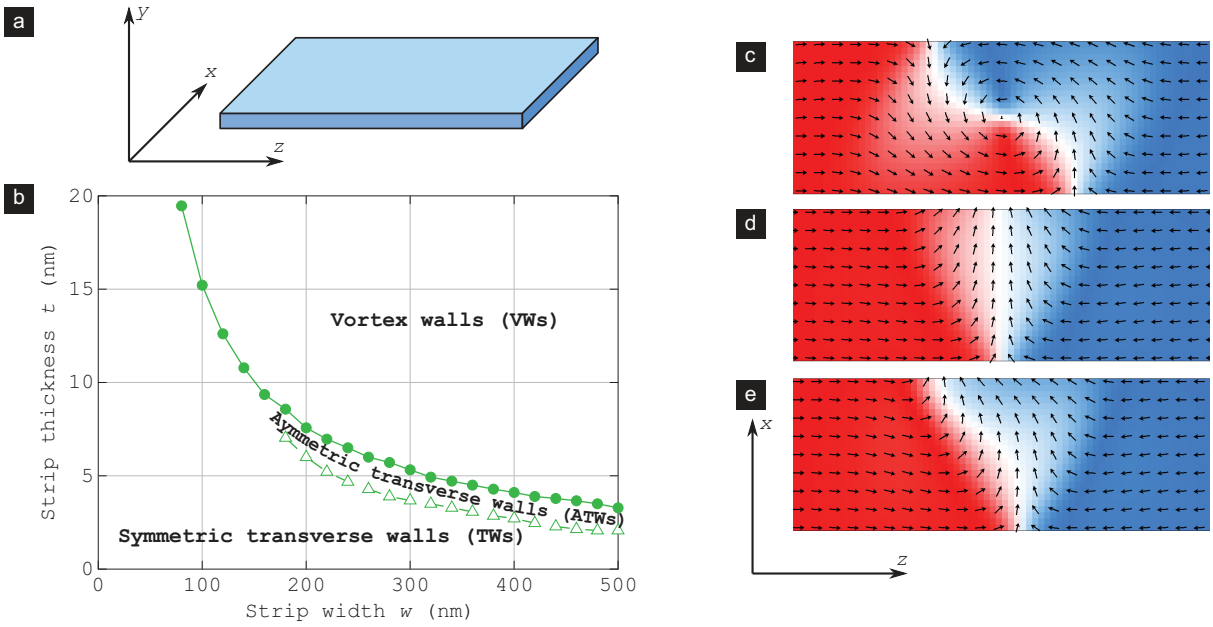

FIGURE 2.1: **Domain walls in strip**. (a) Coordinates used to describe strips, x and y along transverse directions, and z along strip length (or the wire length in case of wire). (b) Phase diagram of DWs in strips known to-date [3, 27] (c-e) Mid-height views of micromagnetic simulations of vortex (VW), transverse (TW) and asymmetric transverse (ATW) walls. Strip width is 100 nm and thickness 16 nm for c and d, 28 nm for e. Color codes magnetization component along z.

2.1 Why does it seem interesting and relevant to build a phase diagram?

So far, a small part of the (t, w) phase diagram has been explored, until $t = 20$ nm and $w = 500$ nm by Nakatani *et al.* [3]. However a larger range of geometries, not covered by this diagram, is experimentally achievable [52]. It is thus relevant to describe domain walls that can be found in such systems. Moreover, strips and wires have been considered as two different kinds of system and physics seems to be different. However, starting from a strip and increasing its width gives rise to a wire. Thus physics should be similar. Moreover, there has been no uniform thinking in the names given to the DWs. As an example various names have been given to refer to the same DW that can be conflicting whether you think for strip or for wire. For example, the names Bloch point wall (BPW) [2, 35], vortex wall (VW) [32, 53, 54] or pseudo-vortex wall [55] have been used to describe for the same object. However, the name VW refers to a type of DW in strip with a topology which is distinct from that of the BPW, raising a problem when, for example, dealing with a square wire that can be viewed as a wire or a thick strip. This is not the only example of confusion that appears when mixing names of DWs. There was a clear lack of a simple DW classification. The need for such a classification comes from the complexity of systems that can be found in 3D structures upon increasing their dimensions. The goal here is to provide a description, using simple characteristics, of a priori complex configurations. For this classification, we use topology, symmetries and we also introduce measurable quantities such as the circulation of the magnetization, asymmetry of a DW and the domain wall width. For this classification, second-order phase transitions and order parameters are linked. This approach was also done [56].

Finally, this phase diagram will be a tool for emerging experimental production of strips or wires with perfect rectangular or square cross section [52]. With a phase diagram, wires can be tailored with dimensions suitable for the desired DW or, conversely, it allows to determine the type of DW for a given geometry.

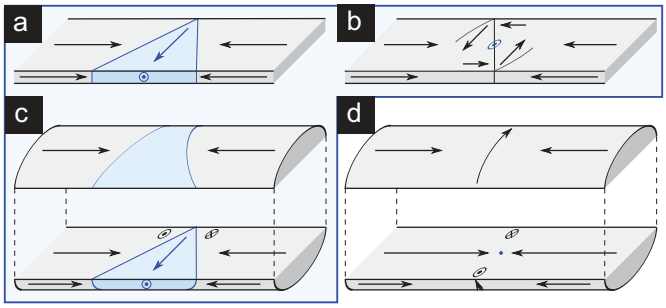

FIGURE 2.2: **Domain wall topology in one-dimensional structures** (a) Transverse wall (TW) and (b) Vortex wall (VW) in strip. (c) TW and (d) Bloch-point wall (BPW) in a cylindrical wire. (a-) share the same topology whereas (d) is of another type.

With these objectives in mind, concepts and simulations presented in this chapter concern systems with either square or circular cross section. As said above, the choice for square cross-section comes from the desire to span continuously the whole space from strips to wires with a geometry that is relevant for experimentalists using lithography. To the contrary, the circular cross-section is more relevant for bottom-up synthesis. All results stand for Permalloy ($Fe_{20}Ni_{80}$) however they can be renormalized with Δ_d to be applied to any other material without magnetocrystalline anisotropy.

Before we go into more details, let us define some notions that will be used in the following. The (t, w) plane is cut with the bisector $t = w$. The area above this line will be called *upper triangle* while the area under will be *lower triangle*.

I will also use the words *circulation* and *curling*. These words are interchangeable. The latter term refers to the curl operator and is related to circulation of magnetization along a close path (Stokes theorem). As seen in sec.1.1.4 and sec.1.1.3, the name curling as been used since the early days of micromagnetism to describe a certain type of reversal mode of magnetic system (Figure 1.6a). It also refers to magnetic textures with this sort of circulation. Curling is not only a transient state (nucleation, reversal) but also a steady state that can be a relevant magnetic configuration at rest (sec.1.1.3). The notion of curling is more general than the one of vortex which highlights the core structure and is related to a particular magnetic distribution, VW in strips.

2.2 Domain wall topology

2.2.1 Transverse versus vortex wall

Take the example of the TW and the VW in strips and examine them in more details (see Figure 2.1c-d). In both of these domain walls, a tube of magnetization goes though the strip. For the TW the tube goes from one edge to the other and at small diameter the configuration is close to the one-dimensional model as in disk-based nanowires of small diameter (Figure 2.3a). In the case of VW, the tube of magnetization goes from the bottom to the top along the thinest dimension. No matter how is the magnetic configuration in these DWs, they share the fundamental aspect that the tube of magnetization goes through the strip. Upon increasing diameter, or upon increasing the thickness towards a square base for strips, the magnetic configuration of the TW becomes more complex so that also curling is found (Figure 2.3). We will discuss this in details in the following. Let us just note for the moment that through a rotation of $\pi/2$ around the wire (be it disk or square-based) axis it should be possible to go from a TW (resp. VW) to a VW (resp. TW). That is in a square and circular nanowires of large enough size, a TW exhibits both a transverse aspect (a tube of magnetization that crosses the wire) (see Figure 2.3b) and a vortex aspect (circulation of the magnetization around the transverse com-

ponent) (see Figure 2.3c) and that the VW and the TW are then degenerate. This degeneracy is an important point enabling us to state they share the same topology and thus it is possible to go continuously from one to the other. In that sense, when a DW exhibits both of transverse and vortex features it is relevant to name it transverse vortex wall (TVW). For dimensions at which these DWs are only either transverse or vortex they may be named TW or VW to avoid any confusion. For a sake of clarity, the direction of the transverse (or vortex core) component is added to the name of the DW, for example, a x-TW for a TW with the transverse component along x-direction.

2.2.2 Bloch point walls

The main feature of the second type of DW is curling, as for a VW. But in the wire case, the curling is longitudinal, also called orthoradial curling, and allows a better flux-closure. This magnetic configuration is made possible in wires and not in strip thanks to a larger lateral dimension. In strips, the cost in exchange energy prevents the formation of such DW. Orthoradial curling prevents a radial component. Moreover, the head-to-head character of the DW forbids a longitudinal component within the wall. Since there is neither a longitudinal component nor a radial one, there must be a point where the magnetization vanishes. This point, predicted early in the theory of micromagnetism [24, 31, 57, 58] is called Bloch point. For this DW, there is no tube of magnetization going through the wire, and with this aspect is of another topology than TW and VW. Due to its very small size, the Bloch point has not been observed directly. The name of Bloch point wall was proposed later by A. Thiaville and Y. Nakatani [2] and is now used by several authors.

2.3 Phase transitions

2.3.1 Definitions

- **First-order transitions** separate two states that are stable or metastable on either side of the transition, leading to a hysteresis. There is not necessarily a breaking of symmetry. Across the transition, the order parameter changes abruptly. For instance the iso-energy line between the TW and the VW in strips is a first-order transition.

- **Second-order transitions** are associated with a continuous rise of an internal degree of freedom in the DW. This degree of freedom is characterized by an order parameter whose transition is continuous with energy and is associated with a breaking of symmetry. In this case, only one state exists on either side of the iso-energy line. As an example, one can think about the transition between TW and ATW in strips [3].

2.3.2 Discussion about the first-order transition between TW and VW

Let us now examine the known TW/VW first-order phase transition. In the lower triangle of the phase diagram (Figure 2.4a), it is known for w up to 500 nm and t up to 20 nm [3] that the x-TW is the most stable under the phase transition line (region 1). Since in strips thickness and width are equivalent, by symmetry versus the diagonal, a x-TW is transformed into a y-TW. Then by continuously increasing the width of the strip, keeping the same direction for transverse component, magnetization can be non uniform in the strip plane so that y-VW is the ground state (region 2). Through this continuous transition from a TW to a VW, three points can be highlighted. First, we see that (obtained through continuous deformation) these two DWs are topologically equivalent (Figure 2.3b,c). Second, both DWs have the same energy on the $t = w$ line, as a $\pi/2$-rotation around the length axis transforms a TW into a VW. Third, as an analogy, it behaves like the liquid-gas transition for which it is possible to find a path to go continuously from one state to the other around a critical point. The path, in the case of the DW, is the

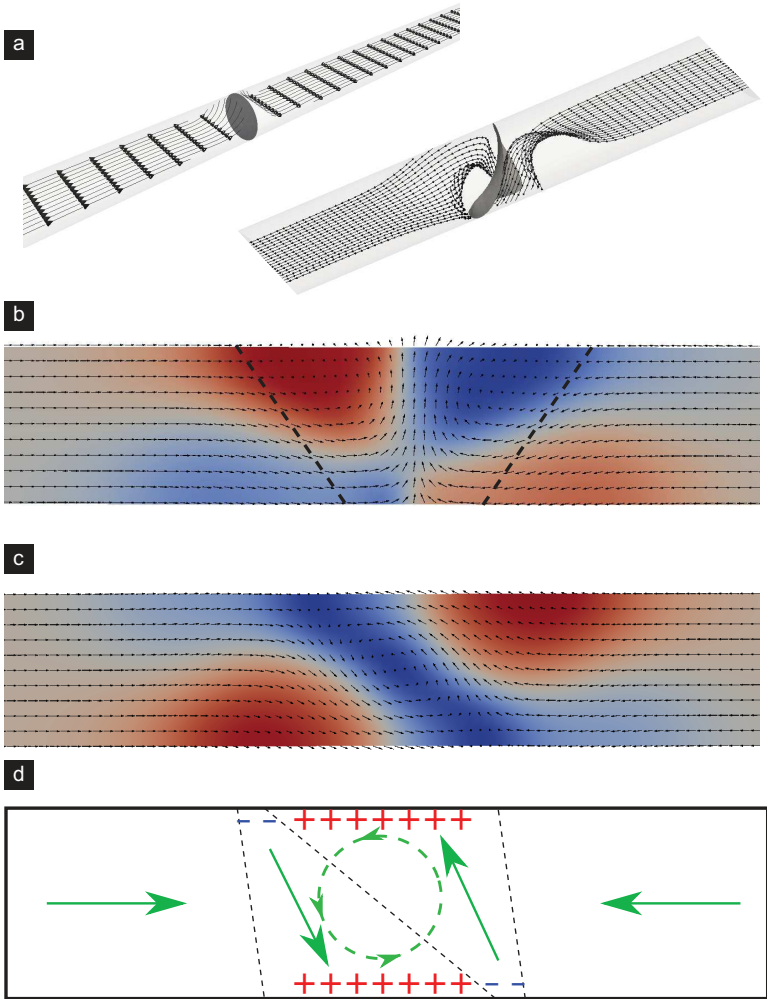

FIGURE 2.3: **Illustration of the transverse-vortex character of a TVW in disk based nanowires**. (a) left: open view of the micromagnetic configuration obtained with FeeLLGood for a 30 nm diameter nanowire. The surface of iso-value $\mathbf{m}_z = 0$ (grey disk) and lines of magnetization are displayed. Right: Open view of the micromagnetic configuration for a circular nanowire of 70 nm diameter. (b) Cross-section view of circular nanowire of 70 nm diameter. Transverse component of magnetization is pointing up. (c) Same micromagnetic configuration $\pi/2$-rotated so that the transverse part is pointing out, revealing the vortex feature of the TVW around the transverse part. (d) Scheme for a TVW with the curling part (dotted circle). Green arrows illustrate magnetization direction, red and blue signs are for the magnetic charges.

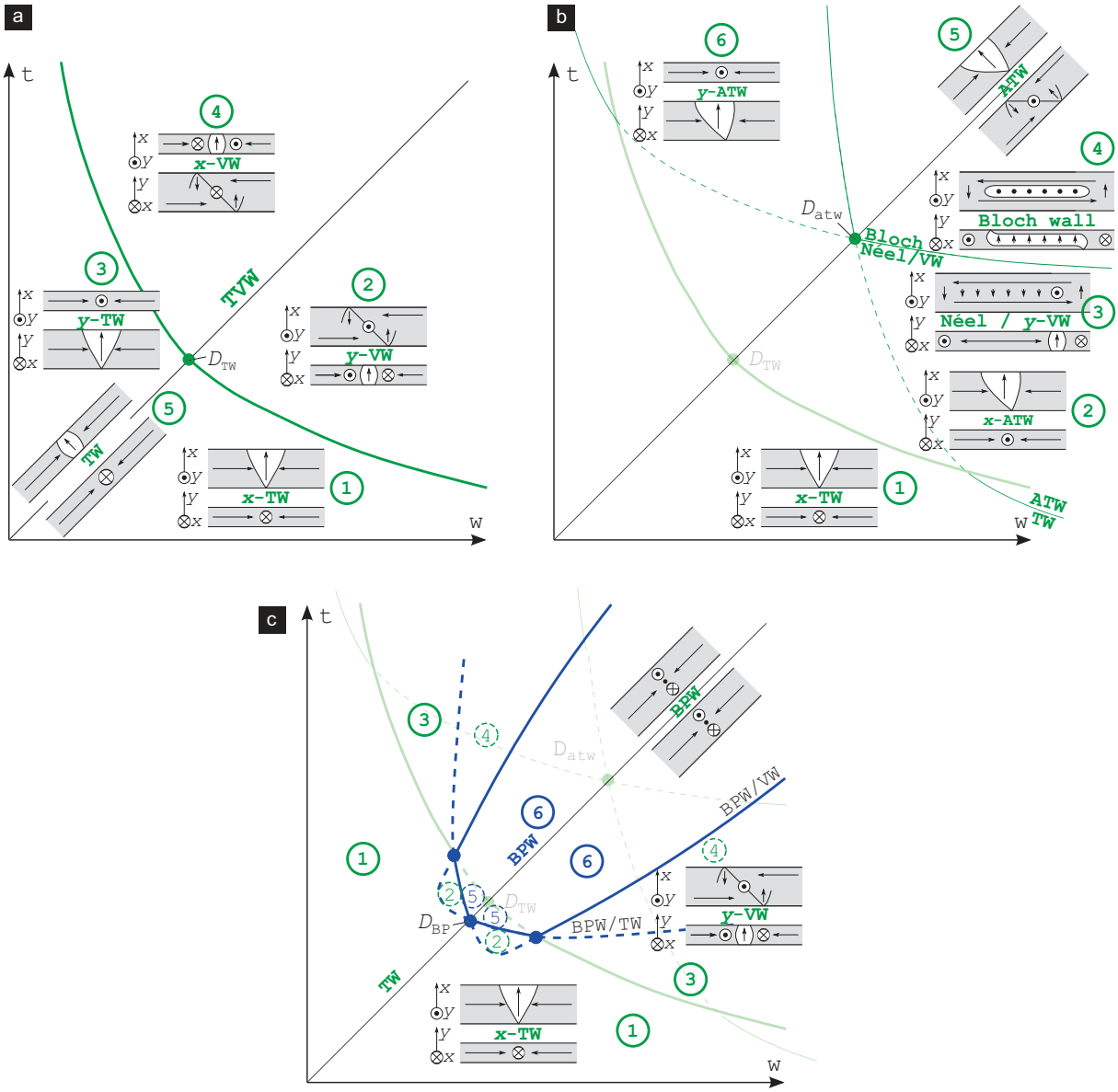

FIGURE 2.4: **Expected phase diagram** Sketches are based on existing knowledge extended by symmetry arguments. Bold (resp. thin) lines mark first (resp. second) order phase transition. Full lines are used to separated two states, one of them being the ground state. Doted lines are used when the two states considered are metastable , the ground state being another one. The phase diagram is built from (a) to (c) adding one by one transition line. (a) First-order transition line separating transverse walls and vortex walls. (b) Second-order phase transition between symmetric/asymmetric TWs, but also VWs from Bloch walls. (c) First-order phase transition separating the BPWs and the TVWs. Thus there are two lines, one separating BPW and VW, another line separating BPW and TW.

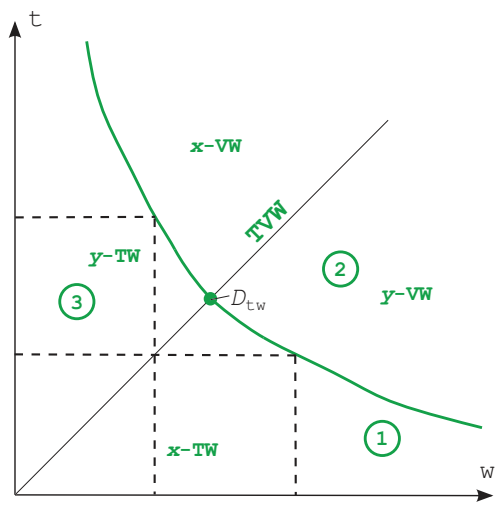

FIGURE 2.5: **Scheme explaining the right angle between the diagonal and the first-order transition line**.

line $t = w$. To close to loop and go back to a x-TW (region 1), transverse component need to rotate and the system to cross an energy barrier with two minima. Thus it is a first order phase transition.

The y-VW is the ground state above the line, in region 2. If we progressively distort a x-TW by increasing the thickness of the strip and decreasing its width we end up in region 3 with $t > w$. The obtained DW is a x-VW of higher energy than a y-TW. Through this continuous transition from a TW to a VW, three points can be highlighted. First, we see that (obtained through continuous deformation) these two DWs are topologically equivalent (Figure 2.3b,c). Second, both DWs have the same energy on the $t = w$ line, as a $\pi/2$-rotation around the length axis transforms a TW into a VW. Third, as an analogy, it behaves like the liquid-gas transition for which it is possible to find a path to go continuously from one state to the other around a critical point. The path, in the case of the DW, is the line $t = w$.

A question is whether the transition TV/VW line crosses the bisector at right angle at the point named D_{TW}. There is only one line of phase transition VW/TW. Let us name $\mathcal{E}(t, w)$ the difference of energy between the x-TW and the y-VW. E_x being the energy of a x-TW and E_y the energy of a y-VW. For any couple $(t, w) > 0$, $\mathcal{E} \in C^2(t, w)$. Thus it is possible to write the Taylor expansion around D_{TW}

$$
\begin{aligned}
E_{x-\mathrm{TW}} &= E_0 + (t-t_0)\partial_t E_{\mathrm{TW}}(t_0,w_0) + (w-w_0)\partial_w E_{\mathrm{TW}}(t_0,w_0) + \frac{1}{2}(u-u_0)^2\partial_{tt}E_{\mathrm{TW}}(t_0,w_0) \\
&\quad + \frac{1}{2}(w-w_0)^2\partial_{ww}E_{\mathrm{TW}}(t_0,w_0) + (w-w_0)(t-t_0)\partial_{wt}E_{\mathrm{TW}}(t_0,w_0) \\
E_{y-\mathrm{VW}} &= E_0 + (t-t_0)\partial_t E_{\mathrm{VW}}(t_0,w_0) + (w-w_0)\partial_w E_{\mathrm{VW}}(t_0,w_0) + \frac{1}{2}(u-u_0)^2\partial_{tt}E_{\mathrm{VW}}(t_0,w_0) \\
&\quad + \frac{1}{2}(w-w_0)^2\partial_{ww}E_{\mathrm{VW}}(t_0,w_0) + (w-w_0)(t-t_0)\partial_{wt}E_{\mathrm{VW}}(t_0,w_0) \\
\mathcal{E}(t,w) &= E_{x-\mathrm{TW}}(t,w) - E_{y-\mathrm{VW}}(t,w) \\
\mathcal{E}(t,w) &= (t-t_0)\mathcal{E}_t^{'}(t_0,w_0) + (w-w_0)\mathcal{E}_w^{'}(t_0,w_0) \\
&\quad + \frac{1}{2}(t-t_0)^2\mathcal{E}_t^{''}(t_0,w_0) + \frac{1}{2}(w-w_0)^2\mathcal{E}_w^{''}(t_0,w_0) \\
&\quad + (t-t_0)(w-w_0)\mathcal{E}_{tw}^{''}(t_0,w_0) \\
\text{where } \mathcal{E}_{\mathrm{i}}^{'}(t_0,w_0) &= (\partial_{\mathrm{i}}E_{x-\mathrm{TW}} - \partial_{\mathrm{i}}E_{y-\mathrm{VW}})(t_0,w_0),\ i = t, w
\end{aligned}
$$

$\mathcal{E}$ remains zero along both the diagonal and the iso-energy line and is non-zero along all

other directions pointing into regions. The swap of t and w is possible if $\mathcal{E}(t,w) = \mathcal{E}(w,t)$ and thus if the line crosses the diagonal at right angle.

2.3.3 TVW-BPW

So far the Bloch point wall has been described in literature for the geometry of wires for either disk [32, 33] or square cross section [2], that is $w = t$. The TVWs and the BPWs do not share the same topology, are separated by an energy barrier and are (meta)stable over a large range of diameters. Thus, the iso-energy line is of first-order. On the bisector, it is known that beyond a point called D_{BP}, located at $t = w \approx 7\Delta_{\mathrm{d}}$, the BPW becomes lower in energy than the TVW [2]. As the energy of a domain wall is continuous versus the system's dimensions, there should exist a region on either side of the diagonal where the BPW is of lower energy than the TVW. There is thus a line of first order transition between the TVW and the BPW associated with this region, on either side of diagonal.

Let have a look at this transition (see Figure 2.4c). On the lower triangle, the x-TVW (*ie* x-TW) and the y-TVW (*ie* y-VW) do not have the same energy so that there must exist two different first order transition lines, one for the x-TVW/BPW (thus x-TW/BPW) and another, for y-TVW/BPW (thus y-VW/BPW). As said before, on the diagonal, TW and VW are degenerate thus both first order lines should intercept on the diagonal at the same point already defined, D_{BP}. As the energy difference between TVW and BPW is differentiable with C^2, no kink is expected at D_{BP}, the two curves display complementary angles with the diagonal. The two lobes of the blue curve are for the continuity of the full line of the transition BPW/TVW.

2.3.4 Asymmetries

The asymmetry towards a slanted wall is reminiscent for the zig-zag domain wall found in extended thin film with uniaxial anisotropy [3]. It is characterized by the fact that the locus of entry and exit of the flux of magnetization on either edge of the strip are shifted along the length of the strip (see Figure 2.1e). This asymmetry has been detected by simulation by Thiaville *et al.* [3] in a refined phase diagram, between the TW and the VW in flat strips. Existence of this DW was permitted by application of a magnetic field along the strip length as a method to induce ATW. ATW remains once field is switched off, justifying the place of ATW in the phase diagram. Asymmetry can also appear spontaneously within a strip. Following this result, let us assume that this asymmetry exists for a broad range of geometries. In Figure 2.4b let us continue the transition line TW/ATW towards the diagonal, and beyond in the upper triangle. In this latter region, broad and narrow dimensions of rectangular cross-section are swapped with respect to region 1 so that starting from a DW with a dominating x-through flux along the transverse direction we still end with a DW with a x-through character but along the short dimension, and thus with a dominant x-VW character. Flux enters from one surface and exits from the other flat surface. Swapped back into the lower triangle this is a y-VW (3). Thus, depending the lateral size it is either a TW or an ATW. There is no metastability domain on either side of the transition line. All these characteristics make the transition TW/ATW a second-order phase transition (Figure 2.4b). Nevertheless the VW/ATW transition remains of first-order as it was previously the case for the transition TW/VW. Introduction of asymmetry in the entry/outlet transforms the VW into a Bloch wall of finite length terminated by a surface vortex at either of its ends (4) [59–62]. This type of asymmetry is related to the physics of the transition from a Néel wall to a Bloch wall upon, *e.g.* applying a magnetic field transverse to the wall [14, 61, 63]. For all cases, asymmetry appears progressively.

If we now focus again on the lower triangle and on the evolution of the microstructure of the lowest energy with the thickness . For a same strip width (for example 200 nm), an increase of the thickness may lead to find ATW (labelled 2) and VW (labelled 3) for small thicknesses and a transition from VW to Landau walls (labelled 3 and 4) for larger thicknesses. The latest transition has been detailed recently [64]. The occurrence of the Bloch wall allows to increase the

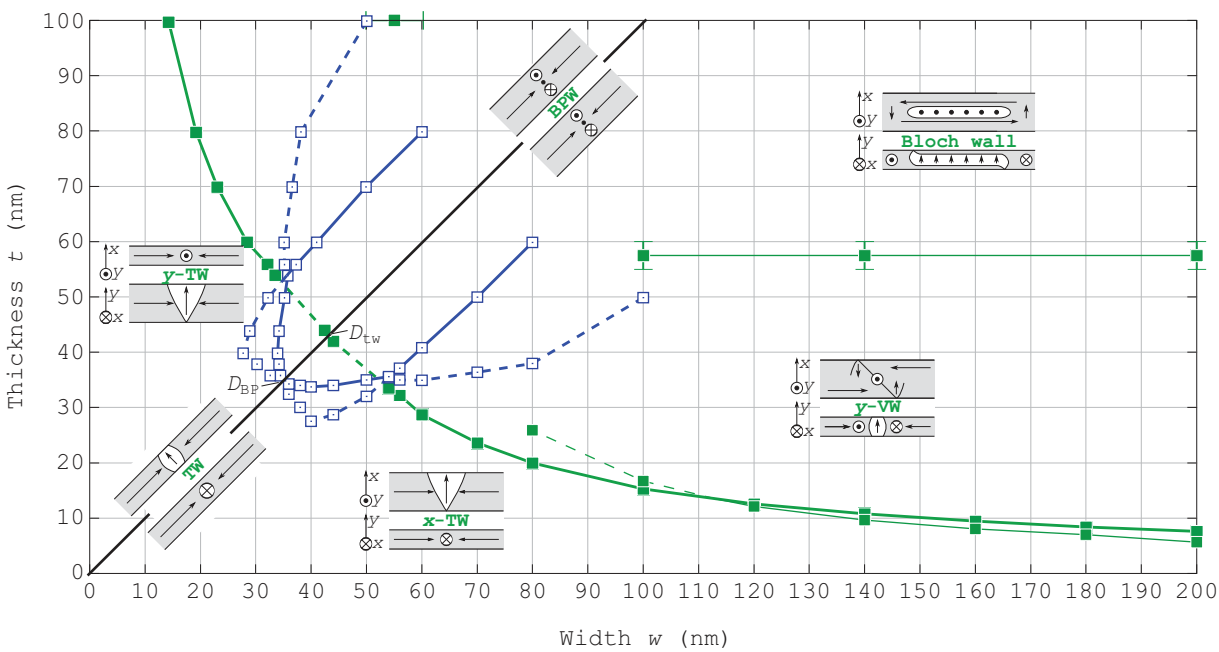

FIGURE 2.6: **Phase diagram obtained with micromagnetic simulations** Notations for the lines are the same as Figure 2.4.

length of the wall by giving an internal structure similar to a tilted Landau flux-closure pattern, illustrating once again similarity between the VW and the TW (see [65] for more details).

2.4 Micromagnetic simulations

Two micromagnetic codes were used to span the whole range of geometries from planar strips to square and cylindrical nanowires. The first code to be used is the finite difference code OOMMF [40] to cover continuously the phase diagram from rectangular strips to square nanowires. The cell size was $1 \times 1 \times 2\,\mathrm{nm}^3$ for strips of width smaller than 60 nm and $2 \times 2 \times 2\,\mathrm{nm}^3$ for strips with larger width, up to 100 nm, and $4 \times 4 \times 2\,\mathrm{nm}^3$ above. The damping parameter was set to 1 to speed convergence with no impact on equilibrium state since we study only states at remanence. Magnetic moments at ends of strips are fixed to prevent formation of end domains, and length of the strips is chosen so that the aspect ratio is at least 10. The second code is FeeLLGood, described previously. For these simulations, size of the tetrahedra is about 4 nm and the damping parameter is set to 1. Charges at ends are removed to simulate an infinite wire.

The parameters are those of Permalloy $Fe_{20}Ni_{80}$: $\mu_0 M_s = 1\,\mathrm{T}$ for spontaneous magnetization and $A = 10^{-11}\,\mathrm{J/m}$ for exchange stiffness. There is no magnetocrystalline anisotropy. For these parameters dipolar exchange length is $\Delta_d = 5\,\mathrm{nm}$. Moreover, since A and M_s are rather similar for common soft magnetic materials, Δ_d is of the order of $3 \sim 5\,\mathrm{nm}$. All simulations can be applicable to soft magnetic materials thus magnetocrystalline anisotropy.

Simulations for strips were done by Nicolas Rougemaille from the Néel Institute. I did the other simulations.

2.4.1 First-order transitions

Simulations were first used to prove the existence and refine the first order transition lines (Figure 2.6). For that, series of simulations of the two states to be compared were performed for a given strip width (along x) and variable thickness (along y). The thickness-dependent

TABLE 2.1: Summary of common features for first and second order phase transition from one micromagnetic state to another

	First order	Second order
Stability	Two states on either side, stable or metastable	Only one state on either side No metastability
Order parameter	Abrupt transition	Continuous transition, breaking of symmetry
Energy	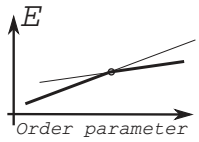	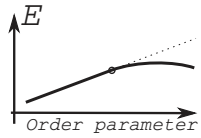

energy was fitted with a second-order polynomial. For first order transitions (x-TVW / y-TVW, x-TVW / BPW and y-TVW/ BPW) states are (meta)stables on either side of the line of equilibrium and their energies cross with different slopes (see Table 2.1) so that an accurate determination of the transition is possible.

For wires with disk and square cross-section, we determined the transition BPW/TW to be $\approx 6.2\,\Delta_\mathrm{d}$ for disk and $\approx 7.0\,\Delta_\mathrm{d}$ for square cross-section. Thus we confirm the magnitude $\approx 7.0\,\Delta_\mathrm{d}$ for the transition in square cross-section as found by Thiaville *et al.* in [2]. Prolongation of the known transition line TW/VW towards diagonal was predicted to be of the order of $43\,\mathrm{nm} \approx 8.5\Delta_\mathrm{d}$. Thanks to simulations, the fitted transition line (Figure 2.6) gives a transition for $t.w \approx 60\Delta_\mathrm{d}^2$ that is to say for a point on diagonal: $d = \sqrt{60}\Delta_\mathrm{d} \approx 7.7\Delta_\mathrm{d}$ meaning the approximation was rather good. Note that for all cases, $D_\mathrm{BP} < D_\mathrm{TW}$.

We are now going to explain this difference between the disk and square-based nanowire transition. Figure 2.10a shows the energy of the two types of DWs for both square and disk cross-sections, normalized by the section area. This normalization, as done in [2], has the advantage that energy converges towards a finite value at low diameter that is $4\sqrt{AK_\mathrm{d}/2}$. This value is obtained within the effective 1D model taking into account exchange and dipolar energies. A close look at curves shows that energy difference between the BPW and the TW is enhanced in disk-based wires compared to square ones. This will be dealt later.

Our simulations confirm that the BPW remains stable over a range of rectangular cross-sections, over both walls with a dominant TW or VW feature. Finally, the existence of two distinct lines for BPW/TW and BPW/VW transitions is confirmed. Since $D_\mathrm{BP} < D_\mathrm{TW}$, we can consider the transition line TW/BPW for small dimensions (up to $w = 50\,\mathrm{nm}$). For larger dimensions, it is the transition VW/BPW which is of interest. Moreover, this order between D_BP and D_TW gives rise to a triple point between the TW, BPW and VW.

2.4.2 Second-order transitions and estimators for their order parameter

For first order phase transition, states are metastable on either side of the transition. Energy curves cross with different slopes, allowing to define a precise intersection point. To the contrary, for second-order transitions, an initially symmetric state continuously develops a feature that breaks its symmetry. Parabolic energy curves of each state is defined on only one side of the transition and both energy curves share the same slope at the transition, making difficult to better determine accurately transition. In that case, there are two possibilities to determine the transition. The first is based on energy. The difference between the energy of one state with the extrapolation of the energy curve of the other state (an extrapolation is necessary because there is no metastability), is expected to scale with $(t - t_c)^{1/2}$ in the Landau theory, with m^2 and m^4 terms in the energy. t_c is the thickness for transition and m an order parameter characterizing the magnitude of breaking of symmetry. The 1/2 exponent was already reported for transitions in micromagnetics despite the complexity of the system [56]. Both branches are then fitted with

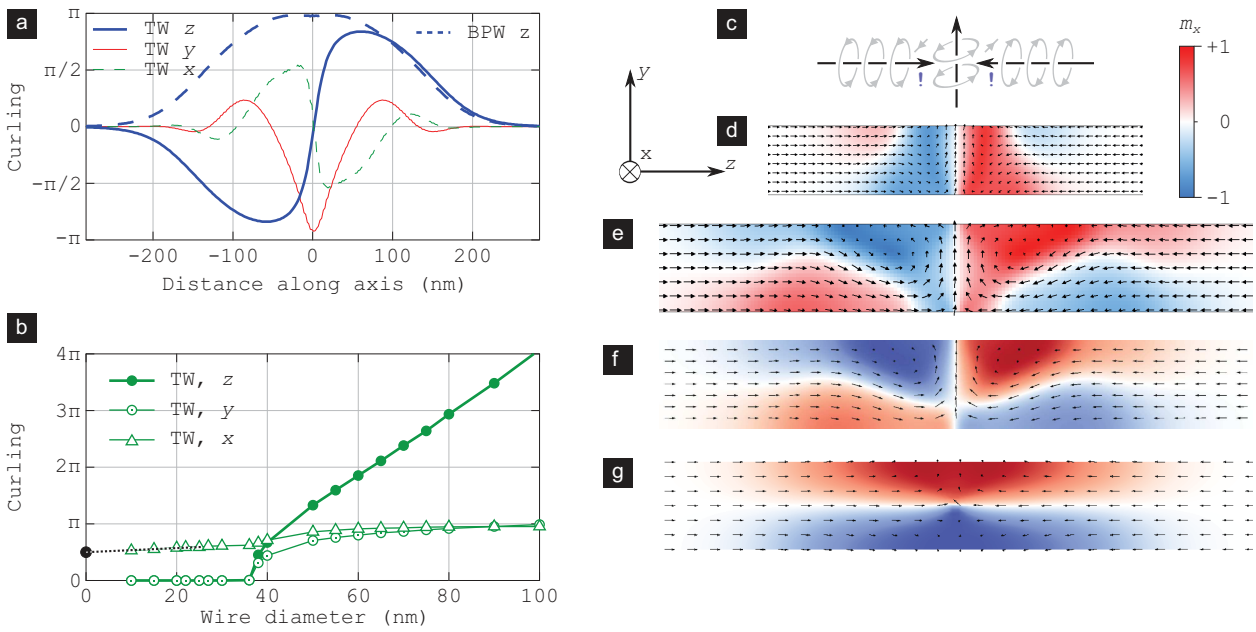

FIGURE 2.7: **Curling features** (a) The three components of the layer-resolved curling for a y-TVW, and the longitudinal component for a BPW, in a wire with a circular section of diameter 80 nm. (b) Integration along the wire axis of the layer-resolved curling for a y-TVW in a circular section wire. (c) Illustration of the competition of transverse with longitudinal curling for TVWs. The dark arrows stand for the mean direction of magnetization, while the light arrows stand for the curling part. Frustrated areas are highlighted with an exclamation mark. Cross-sections highlighting curling through coloring the x component for a y-TVW, for (d) 60×60 nm and (e) 80×80 nm square cross-sections, and (f) 80 nm-diameter disk cross-section of a y-TVW. The sign of the transverse curling is the same in all cases. (g) Longitudinal curling around a BPW for a 80 nm-diameter disk cross-section.

a parabola sharing the same slope at intercept, giving rise to a large uncertainty to determine transition which is thus very sensitive to noise. Thus, this method requires closely-spaced data points and a high accuracy in numerics. Second, an order parameter is defined, characterizing the amplitude of the breaking of symmetry. This order parameter is a (t, w) direction in the phase space. An extrapolation towards zero provides the locus of the transition. An exponent 1/2 is also expected from the Landau theory with m^2 and m^4 and has been reported [56, 66, 67]. It is also possible to find an exponent 1/6 as in [3]. At the transition, the second derivative of this order parameter is not continuous. In the following, we followed the method based on the energies. This procedure already enables us to prolongate the second-order known transition line TW/ATW. This line goes above the TW/VW transition line.

We expect the known transition line TW/ATW to continue until diagonal and above since there is, a priori, no reason for it to stop. Thus we look for its intersection with the diagonal, that is to say in circular or square based nanowires. We tried several methods to induce an asymmetry in these latter systems. The first trial consisted in giving an asymmetry to a TW in the ansatz used as input for micromagnetic simulation. Induced asymmetry should not be to large in order not to give to much energy to the system and get a disordered behavior. After some iterations, TW has returned to its symmetric shape. The second attempt started from a symmetric TW at equilibrium obtained with a micromagnetic simulation with FeeLLGood. A magnetic field of a few tens of millitesla is applied along the wire axis so as to break the symmetry of the TW. While the field is switched on, the TW is asymmetric, but then returns symmetric without magnetic field. These methods has been tested until diameter of 150 nm in circular nanowires. Thus there is not ATW on diagonal. We will come back to this in the following section. Nevertheless, it is possible to extend the previously existing TW/ATW line

as in Figure 2.6 and in the upper triangle, this line exists, as the transition from VW to Néel wall then Bloch wall (see schemes on Figure 2.4b). This line, in the lower triangle, is essentially flat for strip width 100 nm or higher, and we determined it at $t = 57.5 \pm 2.5$ nm. However, when reaching diagonal, the rise of curling is more favorable than the breaking of symmetry (see sec.2.4.2 for explanations).

Increase in curling in transverse walls

Type of second-order phase transition we describe below has already been reported in the context of near-single-domain particles [56], but not in the context of domain walls. The case of VW, with a curling of magnetization around the transverse component, which makes the vortex core, is well known and found in flat strips. This curling develops to decrease dipolar energy but with a cost in exchange. However this curling cannot develop in small size system because the very large gradient of magnetization direction would induce a prohibitive cost in exchange. Following the same arguments, DWs in nanowires of small diameter are essentially one-dimensional as illustrated in Figure 2.3a-left. Circulation is computed using the curl of the magnetization. Since the curl is a vector, it is possible to project it onto a basis made of the transverse component, its orthogonal direction, and the wire axis. For small diameter, it has only one non-zero component reflecting the rotation of the magnetization from one domain to the other. Implemented method is detailed in chap.6.

Increasing diameter, the previously symmetric distribution of magnetization continuously develops an orthoradial curling, either clockwise or anti-clockwise, so as to decrease dipolar energy. This breaking of symmetry is again the signature of a second-order transition, with circulation as an order parameter, for example any component of the quantity **curl m**. For a TW, magnetization curl is non zero. Thus the integration of this quantity and its projection along relevant axis (DW core direction, its orthogonal direction and the wire axis), enables to identify a curling around DW core. This order parameter can be integrated either on the whole wire or on a disk cross-section so as to study the evolution of the circulation with increasing diameter (Figure 2.7b) or along the wire length (Figure 2.7a).

The three components of the z-resolved curl for a TVW in a disk-based nanowire are plotted versus its length in Figure 2.7a, where the transverse component y is chosen to be the TW core azimuth. Transverse curling adds a vortex character to the DW as seen from $(\mathbf{curl\ m}).\mathbf{u}_y$. This DW has developed both transverse and vortex features, whose visibility depends on the cross-section examined Figure 2.3b and c. The reason of difference in the diedron shape at the core of the TW will be dealt later.

When integrated on a disk cross-section and normalized with the diameter d, the z-component (along the wire axis), $(\mathbf{curl}.\mathbf{m}).\mathbf{u}_z$, should equal π for a perfectly orthoradial vector field, *i.e.* close to the situation found at a BPW center. Let us go back to the one-dimensional model and take the example of a x-TW, (Figure 1.10) and look at the y component of the magnetization curl. We see that each side of the TW is like the quarter of a vortex but with opposite directions. Without using of absolute value, the y component of the curl would vanish (odd function as seen in Figure 2.7a).

Thus, when integrated along the length of the wire, we take the absolute value to avoid cancelation and normalize with d^2. The curling is then of about π for a DW of length d. The expected value for the curl along the wire depends both on the length of the wall and the amount of curling in the wire. Thus, a change in the behavior of the magnetization curl, this latter taken as an order parameter, indicates a transition. To follow this transition, the curl of the magnetization is plotted versus wire diameter (Figure 2.7b). The integrated quantity grows rapidly beyond 36 nm ($\approx 7\Delta_\mathrm{d}$) for both y and z components, exhibiting a breaking of symmetry. This behavior is the one expected for a second-order phase transition. The x-component remains almost constant since it stands for the change of orientation from one domain to the other. This quantity ranges from $\pi/2$ at small diameters to π for large diameters. It is not zero at small

diameter because each side of the wall has the shape of a quarter vortex whose center is at the side of the wire. Let us look at the x-component of the curl of the magnetization to understand the limit $\pi/2$:

$$\begin{aligned}
(\mathbf{curl\ m}).\mathbf{u}_x = \partial_y m_z - \partial_z m_y &\sim 1/L, \quad \text{L being the DW width} \\
\int \frac{\partial_z m_y \, \mathrm{d}S\mathrm{d}z}{d^2} &= \frac{\pi R^2}{d^2}\left[m_y(0) - m_z(-\infty) + m_y(0) - m_z(+\infty)\right] \\
&= \frac{\pi}{4} \times 2 \\
&= \frac{\pi}{2}
\end{aligned}$$

At large diameter, it gets harder to find an estimation since the distribution of magnetization is more complex and the 1D model does not apply. Despite this non-zero background, the superimposed increase of the curl of magnetization is clearly visible as a second-order-like feature.

After the transition, the longitudinal curling keeps rising since there is nothing to prevent the magnetization to rotate more than one loop. The reason is that these loops enlarge the wall width and thus enable a decrease of the magnetostatic energy of the wall (see Figure 2.7b). Since volume charges are given by $\mathrm{div}\,\mathbf{M} \approx -\frac{\partial m_z}{\partial z}$, if charges are spread through an orthoradial curling, gradient of magnetization decreases, inducing a reduction of dipolar energy. Moreover, at large diameter, DW width increases (Figure 2.10b) forcing the magnetization not to be longitudinal. This increase of diameter is thus linked with a curling of the magnetization to prevent the magnetization to be transverse to the wire axis and to decrease the dipolar energy. The explanation for the longitudinal curling is less obvious. It is a characteristic more related to the BPW but it has been reported and called *helicoidal domain wall* [68]. Although the two DWs are different the physics explaining the phenomenon is the same. The longitudinal curling allows a progressive variation of the longitudinal magnetization m_z from one domain to the another thus a decrease of its gradient along this direction. Since the magnetic charges are proportional to $-\partial m_z/\partial z$, the longitudinal curling dilutes them and leads to a decrease of the magnetostatic energy. Since the decrease in dipolar energy exceeds the increase in exchange energy caused by the rotation of the magnetization, both longitudinal and transverse are preferred to decrease the energy for these systems.

Before we go further, let us briefly describe the difference between a x-TW and a x-VW. For the latter DW there is the rise of a curling around the x-direction. Contrary to the longitudinal component, the two transverse components do not keep increasing and reach π. This is consistent with the picture of a vortex wall (only one loop around the vortex core). If we go back to strips, the transition between a y-TW (resp. x-TW) and a y-VW with curling (resp. x-VW) occurs at approximately $7\Delta_\mathrm{d}$ for the x dimension (resp. y).

The last paragraph is mainly descriptive and does not give any physical meaning for the rising of the curling in such micromagnetic systems. As all systems, TVW in wire of increasing diameter tries to decrease its energy and therefore the increasing magnetostatic energy. Indeed the dipolar energy has an increasing contribution in head-to-head domain walls while the diameter gets larger.

We can now turn to explanations for the origins of the curling in these two directions. It can be noticed that the transverse curling of a TVW can be viewed, in first approximation, as two ATW of opposite transverse asymmetries (see Figure 2.8b). Thus, in wires there is a breaking of symmetry as well but it is expressed through a curling and not through a shift between enter and exit of the magnetic flux. This curling spreads surface and volume charges leading to a decrease of magnetostatic energy larger than what an ATW would allow. This explains the tendency of the system to develop transverse curling instead of asymmetry in the entry/outlet of the magnetic flux.

As magnetic charges are further apart one from one another, domain wall width L increases, as found in simulations, see calculations in sec.2.5 and Figure 2.10b. For this curve, DW width

has been computed with : $L = \int_{-\infty}^{+\infty} \sin^2\theta \, \mathrm{d}z$, definition given by Jakubovics, apart from a factor 2 [69]. At small diameters the limit is expected to be $2\sqrt{2A/K_\mathrm{d}} \approx 14.1\,\mathrm{nm}$. It is worth noticing that in circular wires of large diameter, DW lengths for both BPW and TVW are similar, as well as the z-resolved curling Figure 2.7a, meaning the driving force is the same for the curling no matter the DW internal structure (see sec.2.5).

Curling: finer features

In this last part, after a presentation of the main aspects about curling and asymmetries we are now dealing with finer points. First, let us focus on the competition between two components of the magnetization curl, longitudinal and transverse curling in TVWs (see Figure 2.7c to follow the discussion). This competition leads to a frustration between both curling directions. Indeed, the direction of the z-component of magnetization is opposite on either side of the DW. On the other hand, the magnetization keeps the same direction around the vortex core all along the transverse direction. These two opposite requests for both curlings are not compatible, and in practice one of them is predominant over the other depending on geometry. In the case of a square-based nanowire (see Figure 2.7d,e) transverse curling dominates (seen by the triangular shape of the transverse part) whereas the two lobes on either sides of the wall originate from longitudinal curling. It is the reverse for circular nanowires (see Figure 2.7f) for which the transverse part does not assume a triangular shape extending over the whole cross-section as was the case for the square nanowire. Indeed, both halves of the wire display each two distincts lobes of opposite signs for the x-component; upon crossing the wall, ne leaves a lobe of positive (resp. negative) sign to enter a lobe of similar shape but of negative (resp. positive) sign. In the square case, only one lobe of definite sign was available right beside the wall core. Here, the persistence of the two opposite lobes up to the very core of the DW highlights a domination of the longitudinal curling over the transverse curling. This competition between longitudinal and transverse curling gives rise to a distorted aspect of TVW with the rise of curling but without asymmetry as stated above.

Linked to these previous remarks, another feature should be noticed. We will look at the longitudinal component of magnetization on the surface of the nanowire ans at the surface charges $\mathbf{m}.\mathbf{n}$, $\mathbf{n}$ being the local normal to the wire surface and pointing outwards. In square cross-sections the longitudinal curling induces an extra cost in energy because of edges, creating surface magnetic charges. Indeed, in Figure 2.8b there are surface charges at edges, and the change of sign is due to the change in the outward normal to the surface orientation, close to DW center. To the contrary, in Figure 2.8a, magnetization remains almost parallel to the surface. This indicates that longitudinal curling of magnetization is not favorable in square-based nanowires. Thus the efficiency of curling to decrease magnetostatic energy is decreased and leads to a reduction of the length of DW. This extra cost is found for both TVW and BPW upon increasing diameter. This extra cost in energy caused by sharp edges may explain the smaller DW lengths for square-based nanowires compared to disk-based ones, as seen in Figure 2.10b. This may also explain the occurrence of an asymmetric BPW (ABPW), which does not exist in disk-based nanowires (Figure 2.8c versus Figure 2.8d). For the same reason, ATW may occur in nanowires with a square cross-section while they may not in wires with disk cross-section. Another fine point related to magnetostatics is a outward radial tilt of the longitudinal component of the magnetization for a BPW in wires with a disk cross-section, at large diameter (Figure 2.8c bottom). The rise of this radial tilt with diameter is presented on Figure 2.9. Inset explains the physical reason, which is the consequence of the positive charge centered on the wall of a head-to-head magnetic distribution. Principle is similar to concertina features in soft planar magnetic elements (*e.g.* [70]). These head-to-head charges are also responsible for the outward radial component of magnetization in longitudinal curling for both BPWs and TVWs (see Figure 2.8b,d presenting an imbalance between positive and negative contrast: curling is not perfectly orthoradial, but slightly tilted). This tilt increases with diameter since magnetic

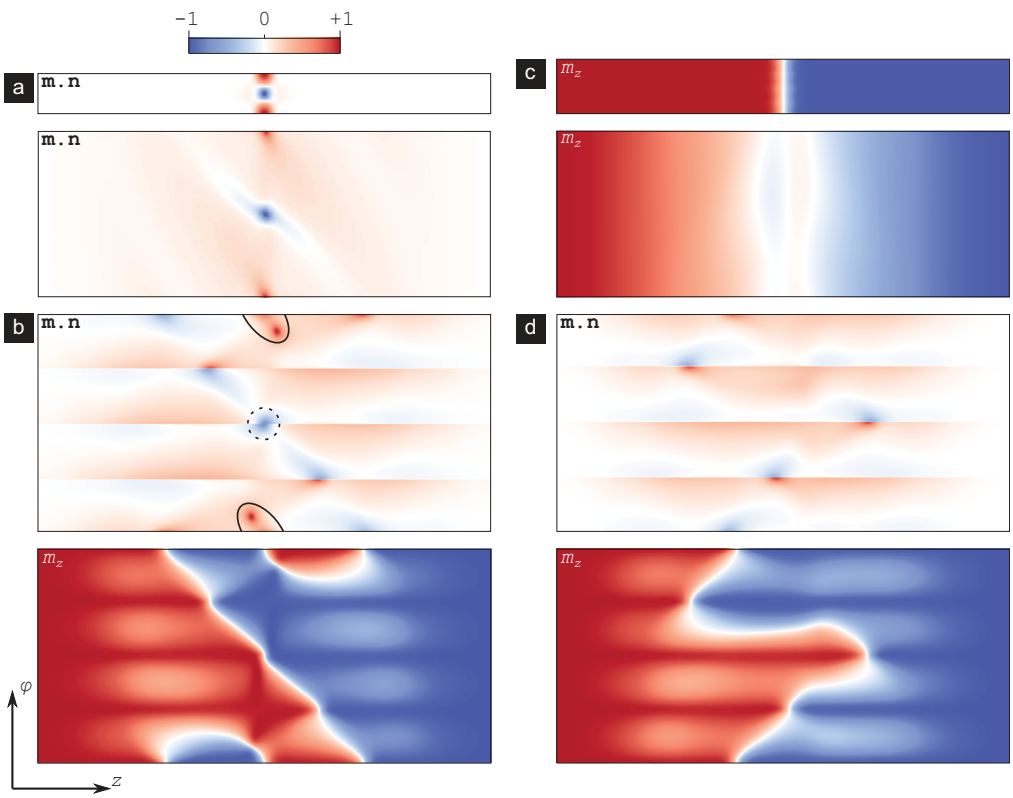

FIGURE 2.8: **Unrolled surface maps** In all cases the length of the view is 1000 nm, and the ratio of lengths along z and φ is exact. (a) $\mathbf{m}.\mathbf{n}$ maps of TVWs for disk cross-sections with diameters 30 nm and 120 nm (b) $\mathbf{m}.\mathbf{n}$ and m_z maps of a TVW for square cross-section for side 120 nm. The circled (dotted-circled) areas indicate the locus of the outgoing (ingoing) flux of magnetization from the core of the TVW. We show here a sub-variety where the flux enters and exits through the edges. (c) m_z maps of a BPW for disk cross-section of diameter 30 nm and 120 nm. (d) $\mathbf{m}.\mathbf{n}$ and m_z maps of a BPW in a square cross-section wire of side 120 nm

charge of the wall increases. So does the dipolar field, tilting the z-component of magnetization at wire surface. It is interesting to note also that the dispersion of magnetization value within one section vanishes with decreasing the mesh size (Figure 2.9). In [71], Pylyposkyi *et al.* used the Landau-Lifshitz-Gilbert equation in term of spins so as to be freed from mesh-dependent effects on Bloch point wall simulations. Moreover they established that the dipolar field of BPW induces a radial component of magnetization in Bloch point structure.

Fine micromagnetic features

The large number of features of DWs close to diagonal forces us not to prolongate some lines into its vicinity. Note for instance that for square-cross section, VW can be of three types. The tube of magnetization can go from one surface to the other, or from one edge to the opposite surface and as a third case, from one edge to the opposite edge. The latter case in found in larger squares for which a flux perpendicular to surface has a prohibitive cost in magnetostatic energy leading to a tilted flux direction.

2.5 Scaling law for domain wall energy and width

So far in this chapter, beyond the general description of the phase diagram, figures come from simulations. They are expected to be numerically accurate but do not always help to build an idea of the physical behavior. It is the purpose of this section to provide physical insights in

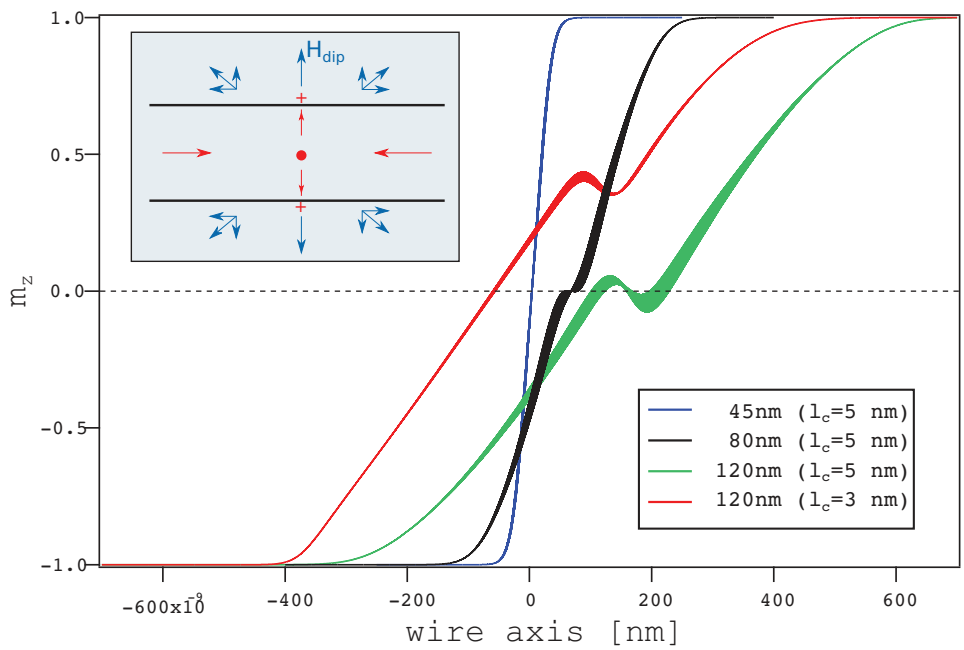

FIGURE 2.9: **Radial tilt of the longitudinal component of magnetization due to the magnetic charge**. Graph of the component of magnetization along the wire axis for three diameter values. For each wire axis position all the values of the z-component of the magnetization are presented, explaining the distribution of values and thus the thickness of the curves. l_c is the mesh size. The shift in the z position only means the DWs are not all centered along the wire axis. The inset is a scheme to explain the physical feature.

selected issues.

To deal with DW energy and length, nanowires are considered. Only quantities at rest are considered. Following the idea of giving trends and not accurate nor exact quantities, it is not of great importance to use the exact definition of the DW width (Lilley[22], Jakubovics[69], Thiele[23], or other). Two models provided an approximation of the DW width for small diameters. The first model is from Nakatani *et al.* [3]. The 1D model for the Bloch wall ($m_x = \tanh(x/\Delta)$, $m_y = 1/\cosh(x/\Delta)$) is a good approximation for DW internal configuration and thus yields a good estimate Δ of the DW width and is valid for $\pi\Delta > 2R$ and thus $R \ll \sqrt{A/K_\mathrm{d}}$. The model of Hertel [72] discards the monopolar charge of the DW under the assumption that it is only an offset on energy and '*does not change significantly with the domain wall width*'. He used a variational approach and found the same width as Lilley.

The purpose of the following is to provide a scaling law for large diameters without neglecting DW charge, which in fact happens to be the leading parameter determining DW width. In a head-to-head wall, the total charge Q is $2\times(M_\mathrm{s}\times$ surface cross-section) that is $Q = 2\pi R^2 M_\mathrm{s}$ for a disk based wire. In order to get a feeling about the importance of the charge, let us assume that it is reminiscent of the triangular shape of the TW in strip, distributed in a sphere of radius R and volume $4/3\pi R^3$. The total magnetostatic energy $\mathcal{E}$ related to these charges scales with $\mu_0 Q^2/R$, so that $\mathcal{E}_\mathrm{d} \sim K_\mathrm{d} R^3$. On the other hand the density of exchange energy scales like $1/R^2$ [as $e_\mathrm{ex} = A\ (\nabla\mathbf{m})^2 \propto 1/R^2$] thus the volume integrated exchange one scales like AR so that magnetostatic energy becomes rapidly the dominating energy with increasing diameter. As seen for curling, to decrease dipolar energy, system spreads magnetic charges and thus enlarges domain wall. This feature is associated with longitudinal curling. An optimum will be found between exchange and the dipolar energy.

We consider the following model. Consider a charge Q, spread over a length L in a disk-based wire of radius R. The volume density of charges is $\rho = 2M_\mathrm{s}/L = Q/\pi R^2 L$. For this situation, we discard numerical factors and compute numerics on an infinite cylindrical wire. We consider

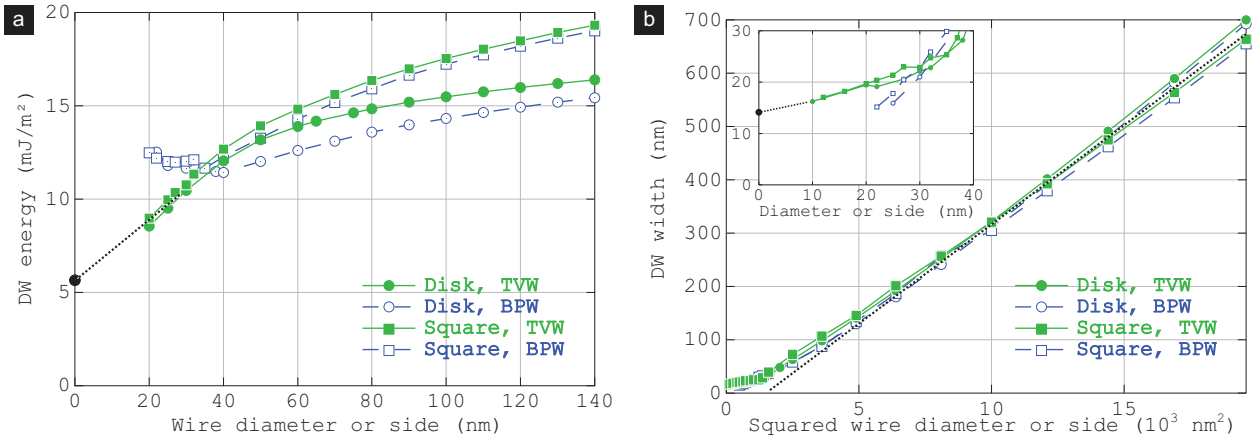

FIGURE 2.10: **DW energy and width square- and disk-based wires** (a) DW energy versus energy normalized to cross-section. The dot on the y axis stands for the limit $4\sqrt{AK_{\mathrm{d}}/2} \approx 5.7\,\mathrm{mJ/m^2}$[2]. (b) DW width versus squared (main graph) lateral dimension. The dot on the y axis of inset stand for the limit $2\sqrt{2A/K_{\mathrm{d}}} \approx 14.1\,\mathrm{nm}$ [2]. Narrow-dotted lines are guides to the eye. Notice that for a given value d the area of the cross-section is larger by the amount $4/\pi$ in squares compared to wires.

separately the inside and outside of the wire. First let us deal with the inside. Since we work with an infinite wire, there is a translational symmetry leading to a logarithmic divergence after integration. In practice, we integrate until a distance L equal to the wire radius, leading to $\log(r/L)$. Thus for the inside, the energy density E_{d} scales like $E_r \sim \rho^2 r^2$ (Gauss theorem). The total energy is then:

$$\mathcal{E}_{\mathrm{d}} = \int_0^R 2\pi E_{\mathrm{d}}\, r\mathrm{d}rL \sim \rho^2 \int_0^R r^3 \mathrm{d}rL \sim \rho^2 R^4 L \tag{2.1}$$

Outside of the wire, dipolar field scales like ρ/r thus energy scales like $(\rho/r)^2$. The integration gives rise to the same scaling than Eq. 2.1, indeed, over a length L the long range dipolar interaction becomes negligible. This means that the dipolar energy scales like $K_{\mathrm{d}}R^4/\mu_0 L$.

We have seen that a curling develops in system of increasing dimensions to reduces surface charges by progressively decreasing the component of magnetization normal to the surface and thus reducing magnetostatic energy leading to an extra cost in exchange energy. The total cost in exchange energy scales like $LR^2 \times (A/R^2)$ thus $\mathcal{E}_{\mathrm{ex}} \sim AL$. The minimization of the total energy $\mathcal{E} = \mathcal{E}_{\mathrm{ex}} + \mathcal{E}_{\mathrm{d}}$ with respect to L leads :

$$L \sim R^2/\Delta_{\mathrm{d}} \tag{2.2}$$

$$\mathcal{E} \sim AR^2/\Delta_{\mathrm{d}} \tag{2.3}$$

The wall width is thus expected to increase rapidly with the wire radius [38]. This law quantitatively fits our simulations (Figure 2.10b), showing that there is a change of regime from low to large diameters that can be found as the point of intersection between the large-diameter regime asymptote and the x-axis. Transition is found at $\sim 8\Delta_{\mathrm{d}}$, close to the apparition of curling. This highlights the tight link between increase of DW length and curling.

Conclusion

In this chapter, DWs in close to one-dimensional systems with geometry ranging from strip to wire have been considered. All DWs found using micromagnetic simulations are of two

types, based on their *topologies*, TVWs and BPWs. For the first ones, found in nanostrips and nanowires, a tube of magnetization goes through the magnetic object. The latter are found in nanowires. The two families are separated by an energy barrier. Contrary to what was reported so far, BPW can be found not only in perfectly square or disk-based wires but also in thick strip and, by extension, probably in non perfectly disk based wires. Using simulations, a phase diagram was built based on arguments pertaining to phase transitions. We confirm the magnitude of $\approx 7\Delta_{\mathrm{d}}$ for the TW/BPW transition in square nanowires. We continued the known transition between TW and VW until the diagonal and found that it is $7.7\Delta_{\mathrm{d}}$. Second order transitions concern a symmetry breaking in a previously symmetric magnetic textures. This symmetry breaking is governed by the goal to decrease magnetostatic energy, either by spreading head-to-head magnetic charges or better closing the transverse component flux. These features may arise only for samples of whose lateral dimensions at least one is larger than the dipolar exchange length $\sqrt{2A/(\mu_0 M_{\mathrm{s}}^2)}$. Asymmetry can be of two types, either an asymmetry such as the one found in asymmetric transverse wall in strips, or curling (with longitudinal or transverse components). The former type of asymmetry may appear for systems with one of the two transverse directions smaller than $7\Delta_{\mathrm{d}}$. As soon as the two dimensions are larger than $7\Delta_{\mathrm{d}}$, transverse curling is preferred as it enables a larger decrease in energy. This transverse curling can also be viewed as two opposite asymmetries on two faces of the strip. This is why there exists no ATW in strips.

Curling seems to be more efficient to decrease the energy (and thus enlarge DW width) in circular wires than in (close to) square nanowires, due to magnetostatic energy associated with edges.

Chapter 3

Shadow XMCD-PEEM: evidencing domain wall types in magnetic cylindrical wires

This chapter is dedicated to the imaging of DWs. We used the X-ray Magnetic Circular Dichroism-Photo Emission Electron Microscopy (XMCD-PEEM) in transmission. This technique presents good compromise for spatial resolution with respect to the surface / bulk ratio for nanowires. Moreover, this technique is compatible with time resolved experiments. The use of transmission give access to the shadow of the wire. This use of XMCD is an original and new approach of this imaging technique.
Moreover, I decided to develop my own model capable to reproduce XMCD contrast from a micromagnetic configuration obtained with FeeLLGood.

In the latter chapter, we derived an extended phase diagram for DWs in strips and nanowires. We can thus assume the type of DW for a given geometry. I am going to apply simulations to experiments, particularly, imaging of DWs.

To chose an imaging technique some criteria need to be defined. Indeed the choice is based on desired information, compatibility with environmental parameters (temperature, applied field, *etc.*), spatial and time resolution, measured quantity (magnetization, induction, stray field, *etc.*). We are looking for a microscopy technique with spatial resolution smaller than the domain wall width so as to be able to identify the domain wall internal structure. Regarding spatial resolution, among microscopies allowing a spatial resolution below 50 nm are XMCD-PEEM [73], STXM [74], electron holography or Lorentz microscopy [75–77], Scanning Electron Microscopy with Polarization Analysis (SEMPA) [78], Spin-Polarized Low-Energy Electron Microscopy (SPLEEM) [79, 80]. Within these techniques some microscopies probe only topmost atomic layer(s) (SPLEEM and SEMPA), others are transmission techniques and gather information about volume magnetic texture over its depth [holography, (S)TXM] with a penetration depth of the order of 100 nm. However, for the latter, information is averaged along the beam so that there is a loss of information in case of a magnetic texture varying along the path. XMCD-PEEM is an intermediate technique with a few nanometers of penetration depth, related to the mean free path of secondary electrons (used for imaging). This technique has been recently applied to three-dimensional objects lying on a supporting surface [4–8], where X-rays are tilted with respect to the normal to the surface. This gives rise to a shadow containing information about magnetization in the bulk. This technique was named shadow XMCD-PEEM [4]. However, due to the three-dimensional shape of objects the considered objects and the depth- and helicity-dependent absorption of X-rays through the structure, the magnetic contrast cannot be interpreted in a straightforward way. Streubel *et al.*. [9, 10] simulated the contrast in the shadow of a rolled tube, however based on an analytical form of the distribution of magnetization in a thin sheet and not on a realistic configuration. Also, contrast at the surface of the structure was not computed. To the contrary, our method is based on micromagnetic structures obtained with the relaxation of the magnetization.

This chapter, after a presentation of $3d$ ferromagnetic materials and XMCD-PEEM technique, deals with the numerical method developed during my thesis to model and analyze the shadow-XMCD contrast. The goal of this method is to provide a quantitative analysis of the contrast using the developed numerical tool. First we present the microscopy technique. The second part is dedicated to the presentation of the experimental set-up. In the third part, we present the absorption model used, how it has been implemented, and test cases used to validate the code. This method is compared to experiment. In a last part, some instrumental aspects are discussed as well as experimental parameters.

3.1 Principle of the microscopy technique

3.1.1 Dichroism in $3d$ ferromagnetic elements

In the present work we deal with $3d$ ferromagnetic material. For these materials, the valence band is composed of full core subshells and a partly-filled valence/conduction band with orbitals $4s$ and $3d$. For free atoms, the $4s$ shell is completely filled whereas the $3d$ one is partially filled.

In ferromagnetic $3d$ metals, spin up and spin down bands are not equally filled. Indeed, there is a shift in energy occurring to reduce the electrostatic interaction by decreasing the band overlap. The shift also increases kinetic energy since energy landscape scales as $\hbar^2k^2/2m$ (this would not be the case if it scaled as $\hbar k/2m$). According to the Stoner criterion, there is a spontaneous band shift. As a consequence, the $3d$ spin up band is more filled than the spin down one leading to the ferromagnetic order (Figure 3.1). Thus the $3d$ band is responsible for the magnetism, and in a first approximation, for the spontaneous magnetization of ferromagnetic material.

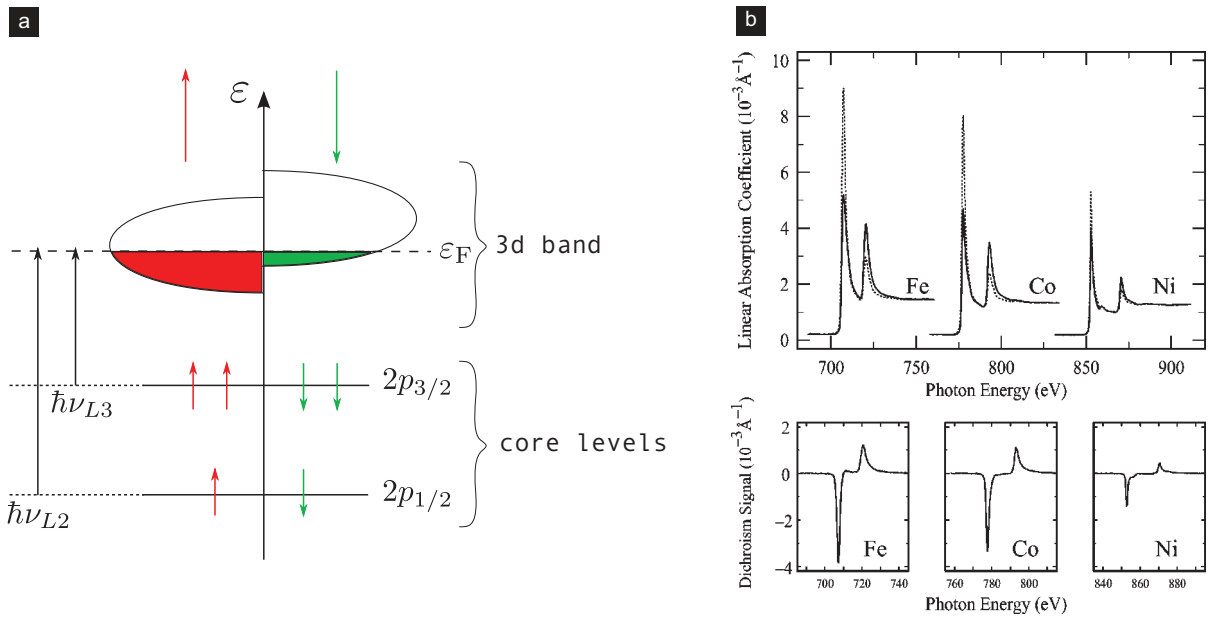

FIGURE 3.1: (a) Schematic view of the band structure of a ferromagnetic material. The $3d$ spin-up band is more filled than the spin-down one. $2p_{3/2}$ state is filled twice as much as $2p_{1/2}$ state. The two black arrows on the left side correspond to the energy to transfer one electron from the core to the $3d$ band. (b) XAS (top) signal for both positive (full line)and negative (dotted line) helicities with the $L3$ and $L2$ edges. Dichroic signal corresponding to the difference between the tow helicities. Graphs from [81].

We are now going to explain the meaning of the $L2$ and $L3$ edges, which we will use in microscopy. Orbital moment $\mathbf{L}$ of an electron in shells couples to the spin, giving rise to the spin-orbit coupling. The latter splits energy levels, previously degenerate, into a number of levels equal to the number of values of the quantum number for $\mathbf{J} = \mathbf{L} + \mathbf{S}$. This splitting is of the order of a few to hundreds of electronvolts depending on the system. In case of ferromagnetic $3d$, the fine structure related to the subshell $2p$ ($L = 1$) is now $2p_{3/2}$ with $\mathbf{L}$ and $\mathbf{S}$ parallel and $2p_{1/2}$ with $\mathbf{L}$ and $\mathbf{S}$ antiparallel (see Figure 3.1a). When excited with photons, electrons can reach a higher level and thus photon can be absorbed only if the photon energy corresponds to an interval between two levels, as energy must be conserved during a transition. For photons of higher energy, electron is only excited towards a free higher energy state or expelled from the atom. During excitation of levels $2p_{3/2}$ and $2p_{1/2}$ towards $\mathcal{E}_{\mathrm{F}}$, edge associated to $2p_{3/2}$ is called $L3$ and the one associated to $2p_{1/2}$ is called $L2$ leading to two different absorption peaks.

Besides energy conservation, the Fermi's golden rule states, using symmetries, that a transition is feasible only if $\Delta\ell = \pm 1$, and $\Delta s = 0$, ℓ being the orbital quantum number and s the spin quantum number. The transition operator must be even not to be null. Thus transition must be done between two odd orbitals or between an even orbital and an odd orbital. s and d orbitals are even. p and f orbitals are odd. According to this rule, electrons excited from $2p$ can only hop towards $3d$ or $4s$. During absorption of photon, the angular momentum of the latter is transferred to the sample. This transfer is -1 ($+1$) for right (left) circularly polarized light leading to another condition on the transition which is :

$$\begin{array}{rcl} \text{left} & : & \Delta m_\ell = +1 \\ \text{right} & : & \Delta m_\ell = -1 \end{array}$$

where m_ℓ is the magnetic quantum number. This restriction is visible only if initial and final states are differentiable. See [82, 83] for further details.

We can now speak about the polarization giving rise to dichroism. This is a requirement electrons are sensitive to polarization of light otherwise there is not any dichroism. Due to

selection rules and the number of state for $2p_{3/2}$ and $2p_{1/2}$ levels, $L3$ peak is twice higher than $L2$ peak. However, at this stage the difference in $3d_{\uparrow}$ and $3d_{\downarrow}$ populations does not matter since $2p$ states are not polarized.

However, if we can excite them with photons of controlled helicity, then angular moment of photons removes the degeneracy of the probability of transition between a helicity parallel or anti-parallel to magnetization. Probabilities of excitation are given by the Clebsch-Gordan coefficients. With a $+1$ helicity, probability for a photon to excite a $2p_{3/2}$ with a spin-up is 62.5 % and 37.5 % with a spin-down. In case of $2p_{1/2}$ these probabilities are 75 % for a spin down electron and 25 % for a spin up one. Same proportions are obtained for a -1 helicity.

In practice, we measure two spectra with opposite helicities. To be rigorous, one should measure the whole energy spectra prior to deduce information about spin and orbital moments. However, in PEEM, most of time we work at a given energy and proceed to the intensity difference for both opposite helicities at this energy (Figure 3.1b)

3.1.2 From atomic absorption to measuring absorption on a material

Let now explain briefly the mechanism of absorption of photon through matter. This will be of use when we model absorption in sec.3.3.1. When a photon travels through matter it has a probability μ per unit length to be absorbed along its path. If μ is uniform, this results in an exponential decrease of the initial intensity $I_{X,0}(\delta)$ along the path: $I_X = I_{X,0}e^{-\mu\delta}$ where δ is the length of the path through matter. If energy $\hbar\omega$ of incident photon is high enough, its absorption by an electron leads to ionization of the atom. The emitted electron is called photo-electron. Its kinetic energy depends on incident photon energy, binding energy and the work function. If photon energy is lower than the sum of the biding energy and of the work function, the absorbed photon excites an electron towards unoccupied states of higher energy. This is the principle of the XAS (Figure 3.1b) which reflects unoccupied states of valence band. For both ionization and excitation, photo-electron needs to decrease its energy to go back to its fundamental state through emission of a photon. This phenomena is called fluorescence. If the photon emitted by fluorescence is absorbed by an electron, the latter is ejected and called Auger electron. Auger electrons lead to multiple inelastic collisions giving rise to secondary electrons. There are more secondary electrons than Auger electrons. Due to the small escape depth of these secondary electrons, only those close to surface escape material.

For each chemical element, there is a specific energy at which core electrons can be expelled. Thus, by scanning photon energy, X-rays reach energies corresponding to transitions between two levels from core to valence band specific to an element.

Absorption peaks of X-ray Absorption Spectroscopy (XAS) spectra provide information about chemical elements found in the sample. Since the beam is monochromatic and photons are absorbed at a precise energy depending on material, this technique gives rise to absorption spectra.

3.1.3 The Photo-Emission-Electron-Microscope

To probe matter, PhotoEmission Electron Microscopy (PEEM) uses an X-ray beam for excitation and collects photoelectrons. Electrons are accelerated when they escape sample and slown down when they reach the imaging plate. Before to reach the channel plate, electrons pass though objective lens which determines resolution. After this lens, there are other lens (two or more) to create an image of the sample behind a backfocal plane aperture. This image is then magnified by projector lenses. At the end of imaging column, there are other combined lenses whose goal is to decelerate electrons prior to the cooled charge-coupled device (CCD).

Collection of these electrons on the detector gives rise to the contrast image according to the amount of photo-electrons emitted from the sample surface. As it is possible to chose energy of incident photons, this technique is selective in element. In practice, a sample extra bias is also available. A positive bias prevents extraction from electrons while a negative one selects

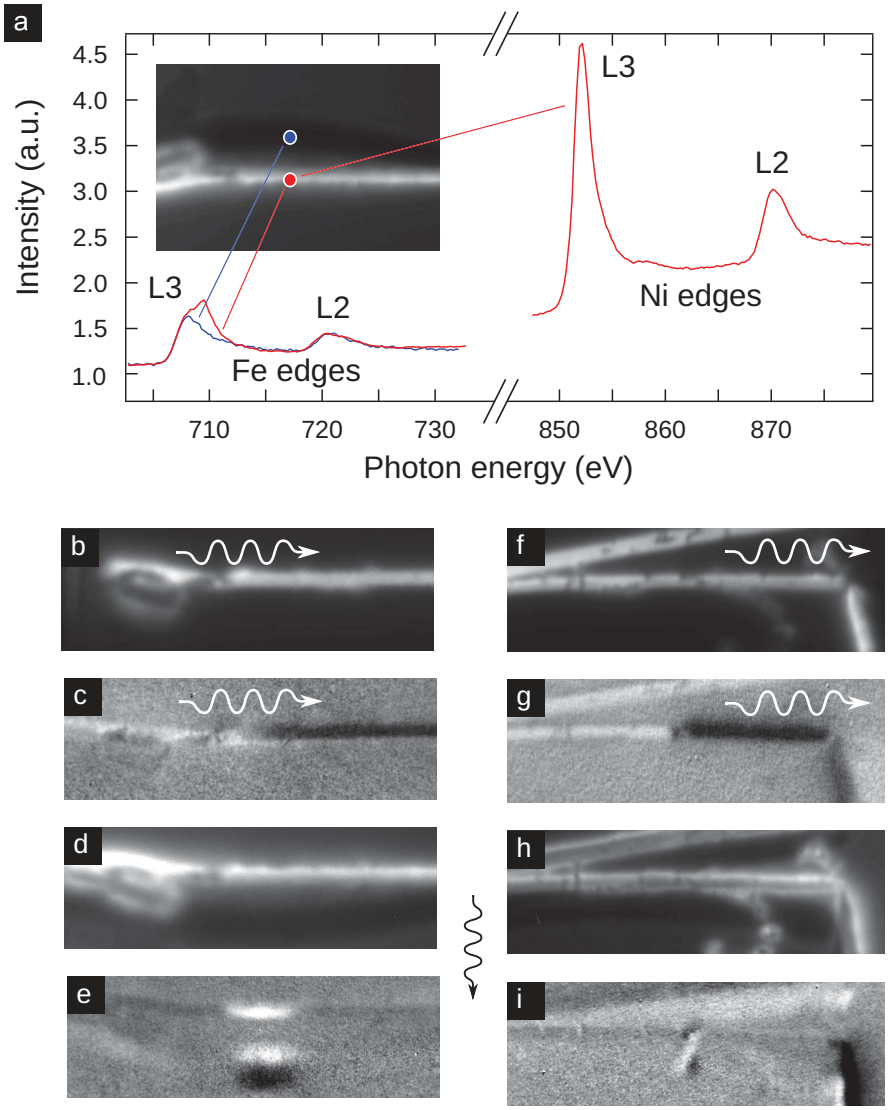

FIGURE 3.2: **XAS and XMCD of cylindrical wires.** (a) Red: absorption spectra across the Fe and Ni L edges normalized to the background signal (absorption on the supporting Si surface). Blue: inverted and normalized spectra measured in the shadow. In each column below are a few views of the same wire, at the same location with a field of view $3 \times 1\,\mu$m. In the top two rows the X-ray beam is parallel to the wires, whereas it is perpendicular to it in the bottom two rows. (b,d,f,h) show the absorption contrast summed for both helicities. A shadow is visible only when the beam is perpendicular to the wire in (d,h). (c,e,g,i) show the XMCD contrast. (b,c,f,g) are obtained at the Ni $L3$ edge and (d,e,h,i) at the Fe $L3$ edge.

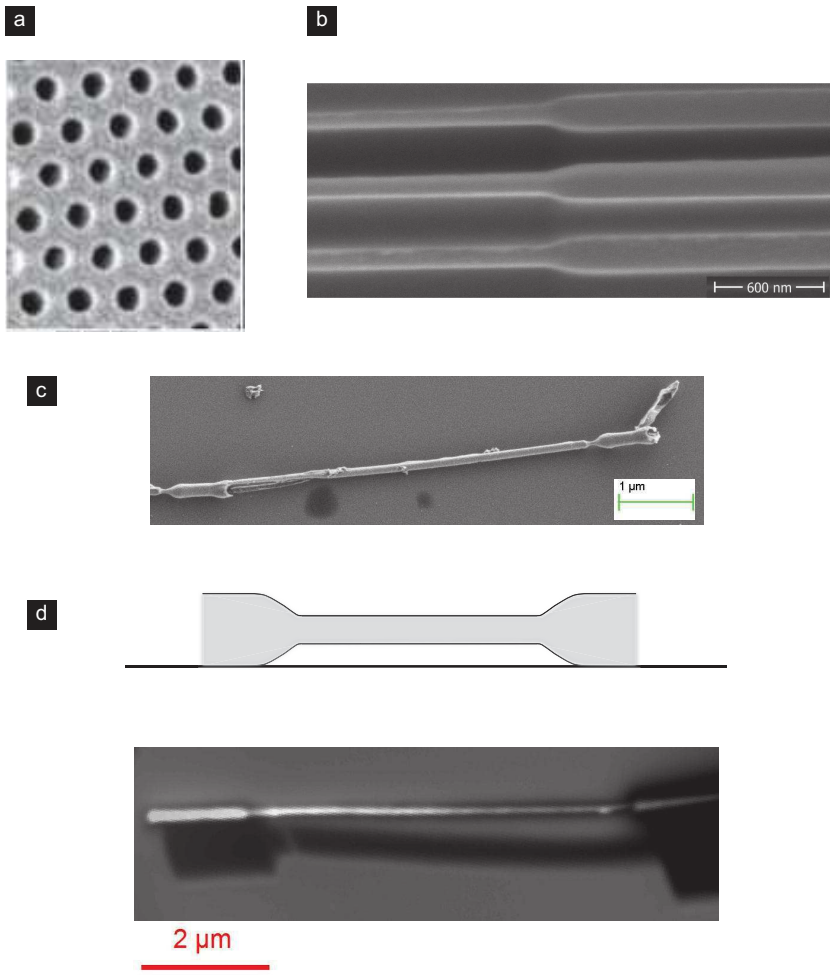

FIGURE 3.3: **Samples** (a) Top view of an alumina membrane. (b) Membrane produced by the chemistry department of the university of Erlangen FAU, used to deposit wires. (c) Wire with diameter modulations at its end, produced by Sandrine DA COL. (d) Scheme of a wire suspended above substrate and XAS image for such wire.

electrons with a finite energy. The peak of secondary electrons is at a few electron volts only, whereas Auger electrons have energies from a few to hundreds of electron volts.

X-rays go through matter over a length of several tens to hundreds of nanometers, excite electrons, but due to the small escape depth of photoelectrons, only those emitted a few nanometers below the surface can escape the sample. PEEM is thus a technique surface.

3.2 Experimental imaging

3.2.1 Samples

The basic principle of synthesis is standard: anodization of alumina templates to get self-organized array of pores arranged on a triangular lattice (Figure 3.3a), followed by filling of the pores by electroplating a magnetic material. This leads to magnetic cylindrical wires. Whereas this general scheme is quite standard, we made use of more advanced techniques to have wires with a diameter modulated along their length. These are obtained in pores initially modulated in diameter. Some had been synthesized by Sandrine DA COL in a pulsed process (Figure 3.3c), while others were fabricated by our colleagues from the chemistry department of Erlangen Nurnberg University, making use of a three-step anodization / dissolution process (Figure 3.3b). Some arrays of pores have been coated with a thin HfO_2 layer, to act as a

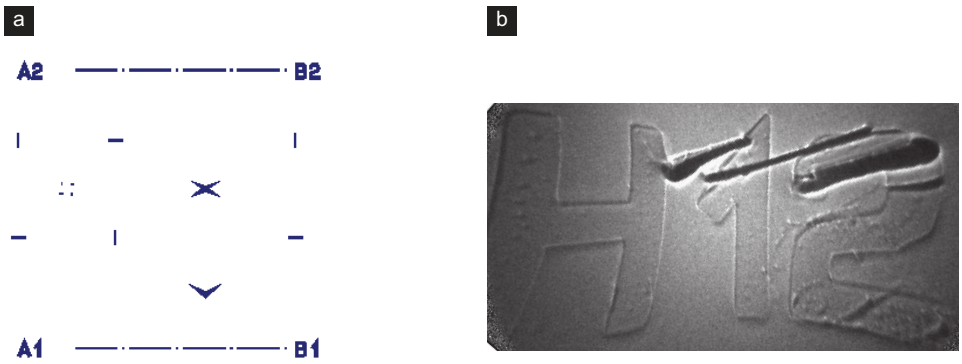

FIGURE 3.4: **Marks on the substrate.** (a) Template used for the marks imprinted on the Si substrate. (b) Wires close to a mark.)

protection against oxidation for forthcoming wires. Wires considered are $Fe_{20}Ni_{80}$ cylindrical nanowires. Alumina matrix is then dissolved with a sodium hydroxide solution. Thereafter wires are dispersed on a Si substrate with alignment marks to make the mapping of interesting wires easier (Figure 3.4). Wires are aligned along a preferential direction using an in-plane magnetic field during the dispersion. The initial idea of the modulations was to restrict DW motion and prevent them from annihilation at a wire's end, so as to be able to study them. Moreover, thanks to these modulations, the thin part of the wire can be suspended above the substrate (see Figure 3.3d) which is a very important feature as will be seen in the following. The length of these wires is a few micrometers.

Prior to perform XMCD-PEEM measurements, samples are characterized. First crystallinity is characterized using X-ray diffraction and Transmission Electron Microscopy. Results show both mono and polycrystalline structures. In a second step, magnetism is investigated using Kerr magnetometry. In a third step, Magnetic Force Microscopy is performed in order to check whether there are DWs.

3.2.2 Set-up

Element-selective X-ray absorption spectroscopy (XAS) and XMCD-PEEM were carried out at the spectroscopic photoemission and low-energy electron microscope [84] operated at the undulator beamline Nanospectroscopy of Elettra, Sincrotrone Trieste. Photons impinge on surface with a grazing angle of 16 °. In our experiments, photons are essentially circularly polarized within an energy range from 50 to 1000 eV. The microscope used at the Nanospectroscopy beamline is an Elmitec Speleem III. Note that the microscope works with Ultra High Vacuum (UHV). Experiments were carried out by Olivier Fruchart, Sandrine Da Col, Nicolas Rougemaille, Raja Afid, Alexis Wartelle, Christophe Thirion, Michal Staňo and myself from the Neel Institute and Andrea Locatelli, Tevfik Onur Mentes, Benito Santos Burgos and Alessandro Sala from Elettra. We went to Elettra for three beam times.

3.2.3 Measurements

Spectroscopy was performed across L edges of either Ni or Fe, using circularly polarized radiation as a probe. Dichroic images were obtained by a pixel-by-pixel operation on the images, taking the difference between intensities obtained for opposite helicities σ_+ and σ_-: $I_{\mathrm{XMCD}} = (I_{e,\sigma_-} - I_{e,\sigma_+})/(I_{e,\sigma_-} + I_{e,\sigma_+})$. Series of several tens of images with an exposure time of few seconds are recorded, drift-corrected and finally co-added [85]. This allows to benefit from a high signal-over-noise ratio while limiting drift effects, providing images with a spatial resolution on the order of 30 nm.

To image a domain wall we proceed in two steps (except on lucky days when you find a domain wall right away). First wires are aligned with the beam. This first step informs about magnetization along the wire axis, that is along the beam direction, and thus can reveal a reversal in the magnetization direction along the wire. Thus a change in the contrast from black to white (or the reverse) locates a domain wall (Figure 3.2b,c,f,g). Then the sample is rotated by 90 ° such that the wires are perpendicular to the beam. At Elettra this is a tedious procedure as the sample holder cannot be rotated. Instead, the sample cartridge must be unmounted from the microscope stage, and brought back to air. The sample needs to be unmounted, rotated and remounted manually at crossed-angle. The cartridge is then inserted again under UHV, remounted on the microscope stage, before proceeding to the re-alignment with the microscope. This entire procedure takes several hours. Notice that more recent instruments may have a rotatable sample holder, such as the one in Alba (Barcelona) or Soleil (Paris). In this second step the magnetization in the domains is perpendicular to the beam and does not give rise to dichroic signal any more (both polarization are equally absorbed). The contrast comes from areas where the magnetization is not aligned with the wire axis, such as the DWs. It can also come from diameter modulations and wire ends where orthoradial curling texture can develop to decrease the dipolar energy (Figure 3.2d,e,h,i) (see sec.3.3.3).

It can be seen in Figure 3.2(e,i) that DWs may give rise to two types of contrast, with a rather complex structure. We have thus access to information from the wire surface but also from its shadow thanks to the grazing angle of 16 °. To attribute a type of DW to these contrast and to understand them, simulated contrast appears to be an important tool, as will described in the following. Notice that with experimental contrasts, we have information from the surface of the wire and from its shadow. The latter is another motivation for a simulation tool to understand it.

3.3 Developing simulations for the quantitative analysis of shadow XMCD-PEEM

3.3.1 Absorption model

Here we start from 3D micromagnetic textures as an input to simulate the resulting XAS and XMCD contrasts to be expected at the surface of the nanostructure and in its shadow. We used two kinds of magnetic textures. The first type is analytical configurations that are used to highlight simple aspects of the technique, or to compare numerical and analytical results for the XMCD contrast. The second type of configurations are realistic ones, resulting from micromagnetic simulations. For that we use the home-made finite element code FeeLLGood [86]. Material parameters are chosen so that they are suitable for Permalloy ($Fe_{20}Ni_{80}$) : $A = 10\,\mathrm{pJ/m}$, $\mu_0 M_s = 1\,\mathrm{T}$. In order to quicken the relaxation towards equilibrium, the damping parameter α was set to 1. This has no impact on the result since we considered only states at rest. No magnetocristalline anisotropy was considered. In this section we explain the method that starts from a magnetic structure and leads to a XMCD contrast. For XMCD-PEEM contrast modeling, we need to consider mainly three aspects. First is the absorption of photons through matter. Second, photo emission of electrons close to surface. Third, collection of these electrons in the microscope.

Let us first consider X-ray absorption. At each position during the travel through matter, a probability of absorption per unit length, μ, is associated to the X-ray to be absorbed. This probability results in a mean free path $\lambda = 1/\mu$, and depends on the material and the photon energy. μ also depends on the direction of magnetization compared to the direction of the beam and its helicity (this is dichroism), which makes μ position-dependent. We consider the absorption at the L2 and L3 edges of Fe and Ni and use the coefficients determined experimentally in the case of pure materials and for both helicities (Nakajima *et al.* [87]). For Permalloy we assume the absorption coefficient to be $\mu = 0.2\mu_{\mathrm{Fe}} + 0.8\mu_{\mathrm{Ni}}$. All the coefficients are summarized

TABLE 3.1: Absorption coefficients μ at the different absorption edges. Figures for pure elements are derived from [87]

Edge	Helicity	μ_{Fe} (nm^{-1})	μ_{Ni} (nm^{-1})	$Fe_{20}Ni_{80}$			
				μ (nm^{-1})	$\Delta\mu$ (nm^{-1})	$\frac{\mu_+-\mu_-}{\mu_++\mu_-}$	λ (eV)
Fe L3	μ_-	0.09	≈ 0	0.018	-0.008	-0.29	706.8
	μ_+	0.05	≈ 0	0.010			
Fe L2	μ_-	0.03	≈ 0	0.006	0.002	0.14	719.9
	μ_+	0.04	≈ 0	0.008			
Ni L3	μ_-	0.017	0.053	0.046	-0.011	-0.14	852.7
	μ_+	0.017	0.040	0.035			
Ni L2	μ_-	0.017	0.017	0.017	0.003	0.08	870.0
	μ_+	0.017	0.021	0.020			

in Table 3.1 where μ_+ and μ_- stand for for the absorption coefficient for the left and right polarized X-rays, respectively. At the Fe L edges the absorption due to Fe is very large and the pre-edge absorption due to Ni is very weak. Thus the absorption due to Fe is the dominating one. At the Ni L edges the post edge absorption due to Fe is no more negligible because the absorption on Ni, with its nearly filled $3d$ band, yields less intensity. However, due to the larger content in Ni, the latter remains the dominant contribution to absorption.

Progressive absorption of the beam in matter is obtained by integrating its position-dependent rate of absorption through each thickness $\mathrm{d}\ell$ of material:

$$\frac{\mathrm{d}I_{X,\sigma_\pm}}{\mathrm{d}\ell} = -\left[\frac{1}{2}\mu_+(1 \pm \hat{\mathbf{k}} \cdot \mathbf{m}) + \frac{1}{2}\mu_-(1 \mp \hat{\mathbf{k}} \cdot \mathbf{m})\right] I_{X,\sigma_\pm} \tag{3.1}$$

This formula takes into account energy and helicity dependence, in relation with the direction of magnetization when in the sample, with $\hat{\mathbf{k}}$ the unit vector along the propagation direction.

Second, we consider the escape of electrons from matter, to yield intensity $I_{e,\sigma}(\mathbf{r}_\mathrm{s})$ at any point $\mathbf{r}_\mathrm{s}$ at surface. Since the escape length of photo-electrons is only a few nanometers, smaller than the diameter of wires and than any characteristic magnetic length, we make the assumption that $I_{e,\sigma}(\mathbf{r}_\mathrm{s})$ reflects intensity of photons at the very surface $I_{X,\sigma}(\mathbf{r}_\mathrm{s})$. Thus, we need to estimate the intensity of emission of photo-electrons $I_{e,\sigma}(\mathbf{r}_\mathrm{s})$ at surface, related to the intensity of photons $I_{X,\sigma}(\mathbf{r})$ previously calculated. For magnetic materials, local absorption depends on local magnetic configuration and helicity of the polarized beam. Thus photon intensity is multiplied by a dichroic factor to give rise to photo-electron intensity. To the contrary, in case of non magnetic surface, for example on the supporting surface, there is no dichroism and $I_{e,\sigma}(\mathbf{r}_\mathrm{s})$ is proportional to $I_{X,\sigma}(\mathbf{r}_\mathrm{s})$.

Let us then discuss the escape of electrons from matter. Theoretically, photo-emitted electrons are emitted isotropically and not perpendicular to the local nor mean surface of sample. Thus, we expect that the local rate of electrons escaping matter results from the convolution of the electron intensity described in the previous paragraph, and a function describing this scattering processes, including production of secondary electrons. In practice however, as the electron escape depth is only a few nanometers, expected broadening should not exceed these few nanometers, which is much smaller than the instrumental resolution (circa 30 nm). Thus, these effects may be safely neglected. At this stage we have an estimation of $I_{e,\sigma}(\mathbf{r}_\mathrm{s})$ at each point of the surface of the nanostructure and on the supporting surface.

As a third step we need to convert this intensity $I_{e,\sigma}(\mathbf{r}_\mathrm{s})$ into the intensity per unit surface of the detector $I_{\mathrm{s},\sigma}(x, y)$. One parameter linking $I_\mathrm{s}(x, y)$ with $I_{e,\sigma}(\mathbf{r}_\mathrm{s})$ is the angular acceptance of the microscope. Indeed electrons are emitted on the average along the normal to the local surface, thus with an angle θ with the microscope axis (Figure 3.6a). Instrumental angular collection is not exactly known and may depend on the extraction and electron energy, on the

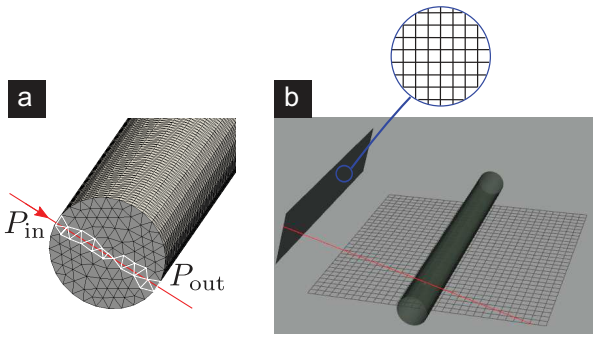

FIGURE 3.5: **Numerical implementation.** (a) presents the method to model the X-ray beam. The red line stands for the X-ray beam that crosses the elements (in white, from the finite element discretization) (b) shows the wire on the gridded supporting surface and photon source. The insert shows the grid of the source, as an example for all grids

contrast aperture, surface roughness, *etc.* Thus the aim is not to consider an exact transfer function but to get an estimation. As collection is maximum for $\theta = 0$ and zero for $\theta = \pi/2$, we used as a crude model the collection efficiency $\cos\theta$. Thus, as the area of nanostructure surface per area of the detector scales like $1/\cos\theta$, this choice simply results in the projection of $\mathbf{r}_{\text{s}}$ onto the plane of the supporting surface to get its (x, y) coordinates.

In the end, the XMCD contrast is computed as defined previously ($I_{\text{XMCD}} = \frac{I_{\text{s},\sigma^-} - I_{\text{s},\sigma^+}}{I_{\text{s},\sigma^-} + I_{\text{s},\sigma^+}}$). Thanks to the grazing angle of angle of 16 °, in the shadow the resolution is increased by a factor 3.6 in the direction perpendicular to the beam. Moreover, as some wires are suspended above the substrate surface due to the modulation of diameter we have access to the whole wire shadow, projected on substrate. To be as close as possible to experiment, wires can also be suspended in simulations.

Note that the above procedure is not a bijection but a surjection. Indeed, different magnetic configurations could result in the same image contrast, as in regular XMCD-PEEM method. This, along with other issues contributing to image formation such as photon scattering, field distortion due to wire topography and background electron intensity, will be discussed further later on (sec.3.5).

3.3.2 Numerical implementation

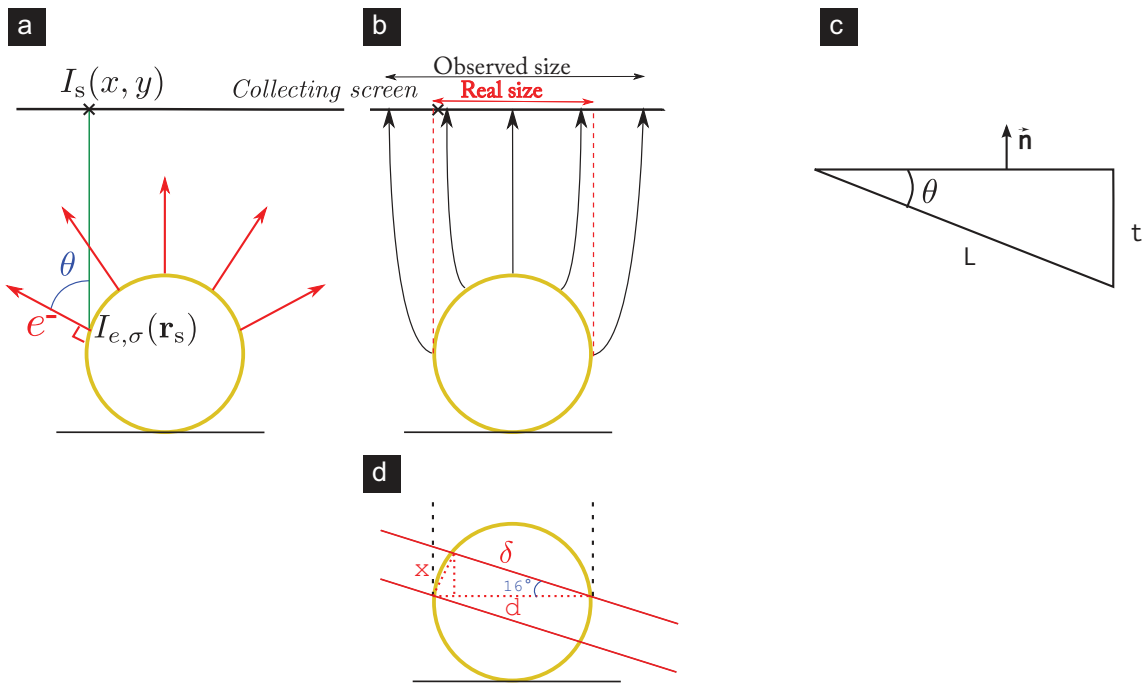

FIGURE 3.6: (a) illustration of the collection of the photo-electrons. $\mathbf{e}^-$ is the secondary electron emission direction. θ is the angle between the imaging axis and the latter direction. (b) illustrates the distortion of the photo-electron trajectory (see sec.3.5.5). (c) Scheme to explain the $1/\hat{\mathbf{k}}.\mathbf{n}$ factor. $\mathbf{n}$ is the outward normal to the system.

In the present study we consider cylindrical nanowires. The numerical method principle consists in launching parallel rays to mimic the photon source. We consider a regular planar grid perpendicular to the direction of photons, that stands for a parallel and uniform source of photons (Figure 3.5b). From each node a ray is launched and intercepts the surface of the cylinder at two points P_{in} and P_{out} respectively, called entering and exit points.

The first step is to compute absorption of photons through matter following equation Eq. 3.1. For this aim we need to calculate absorption along the ray. The latter is discretized into segments of a chosen length between P_{in} and P_{out}. The integration carried out at the points separating these segments.

The second step is the production of photo-electrons related to the relative orientation between the local magnetization and the wave vector, called dichroism. This latter is taken into account at the wire surface:

$$I_{e,\sigma_\pm} \propto \frac{1}{\mathbf{n}\cdot\hat{\mathbf{k}}}\,\frac{2}{\mu_+ + \mu_-}\left(\frac{1}{2}\mu_+(1 \pm \hat{\mathbf{k}}\cdot\mathbf{m}) + \frac{1}{2}\mu_-(1 \mp \hat{\mathbf{k}}\cdot\mathbf{m})\right) I_{X,\sigma_\pm} \tag{3.2}$$

with $\mathbf{n}$ the local outward normal to the surface. The pre-factor $1/(\mathbf{n}\cdot\hat{\mathbf{k}})$ reflects the fact that X-ray entering matter at an angle travels along a length scaling like $1/(\mathbf{n}\cdot\hat{\mathbf{k}})$ while remaining at a depth smaller than the escape length of electrons, thus contributing more to photo-emission. As the mean free path of photons is much larger than that of electrons, the photon flux remains nearly unchanged within this escape scheme, so that the number of electrons emitted is simply proportional to the length of the photon path. A rapid calculation reads (Figure 3.6c):

$$\sin\theta = \frac{t}{L} \Rightarrow L = \frac{t}{\sin\theta} = \frac{t}{\cos(\pi/2-\theta)} = \frac{t}{\hat{\mathbf{k}}.\mathbf{n}} \tag{3.3}$$

Note that the right hand side is the derivative of X-ray intensity along the propagation path (as in equation 3.1). The physical sense is clear, as the derivative of $I_{X,\sigma}$ is the amount of photons absorbed within that incremental distance, and photoemission is directly proportional to absorption. For point P_{sub} on substrate, found with the intersection between the ray and the substrate, photo-electron intensity corresponds to integrated intensity at P_{out} but with no dichroism pre-factor. Since secondary electrons are ejected normal to surface there is also no correction related to the angular acceptance.

The third step in the procedure allocates a photo-electron intensity to all the detector grid points. P_{in} with coordinates (x, y, z), is associated with $I_{\text{s}}(x, y)$ on screen. In practice, we want to deliver an image at the screen, so sampling points x and y should be evenly spaced. However, the lateral density of P_{in} and P_{out} is not uniform due to the curvature of wire. To solve this problem we determine the corresponding detector cell whose coordinates are the closest of coordinates (x, y) and its near neighbors so as to smooth the photo-electron intensity. It is equivalent, in signal processing, to apply a laplacian filter which tends to cut off high spacial frequencies. Finally the XMCD-PEEM contrast is calculated on detector grid.

To be as close as possible to the experimental results, wires are suspended above substrate. This suspension is to be adapted for the distance between the wire and its shadow to fit the one of experimental result.

3.3.3 Test cases

In this section we apply simulation method to test cases: transverse magnetization and orthoradial curling. These distributions do not exist as such however it enables to validate the code. It also highlights physical aspects and features that can arise in XMCD-PEEM contrast and can be useful later identify DWs. In both tests, numerical result was compared to the analytic one.

For the following explanations, let us say that magnetization antiparallel to the direction of X-rays absorbs more σ^+ polarized rays than the other polarization. On the reverse magnetization parallel to the direction of the X-rays absorbs more σ^- polarization.

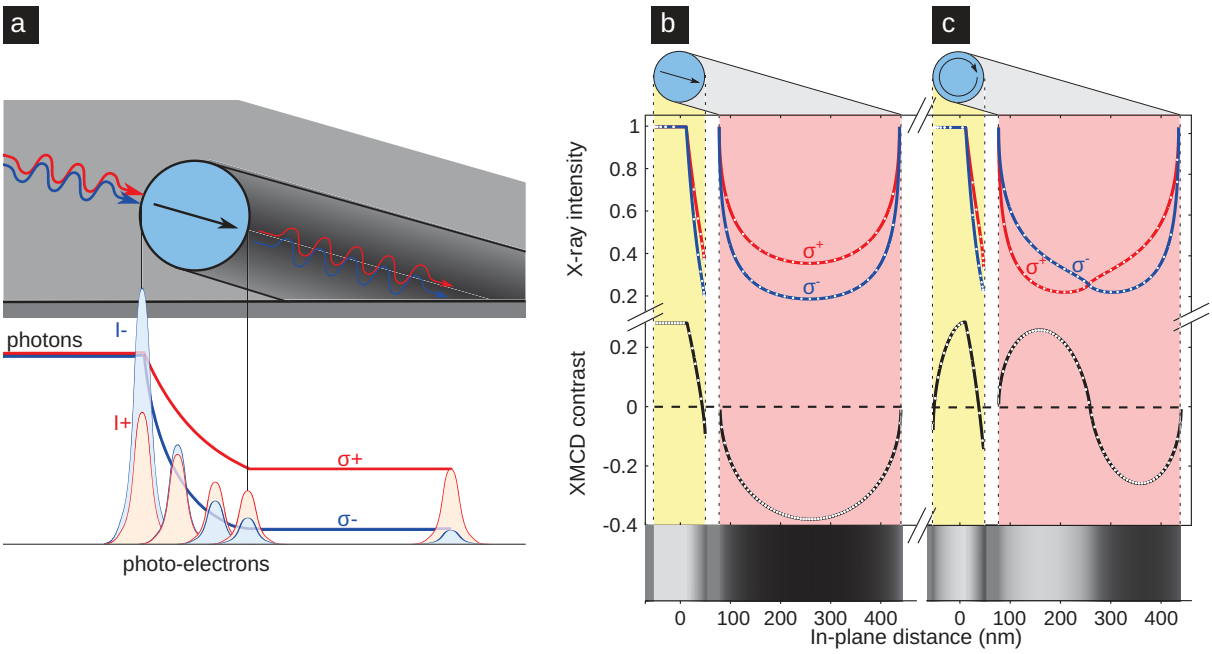

FIGURE 3.7: **Illustration of XMCD-PEEM.** (a) Illustration of the principle of the dual surface and volume contrast on the basis of the test case of magnetization parallel to the X-ray beam. The curves below present the polarization-dependent X-ray intensity at the absorption peak as the X-rays propagate through the wire section. The first test case is (b) uniform magnetization across the wire and parallel to the X-ray beam. The second test case (c) is orthoradial curling. Photon density and XMCD at the surface of the wire (yellow background) and in the shadow (pink background). The dots stand for the numerical simulation whereas the full lines are for the analytical solution. The bottom part presents the XMCD contrast for each configuration. A gap has been set between the wire and the surface so that the entire shadow is visible. Note that the lateral scale is expanded by a factor $\sin(16\,^{\circ}) \approx 3.6$ in the shadow, thanks to the grazing incidence.

Uniform transverse magnetization

The first test case is a wire uniformly magnetized along with the X-ray direction. Figure 3.7b shows $I_{X,\sigma}(\mathbf{r})$ and the resulting surface absorption $I_{X,\sigma}(\mathbf{r}_\mathrm{s})$ for photons going through the wire. The two curves illustrate that photons with one of the polarization are more absorbed than those with the other polarization. Since magnetization does not change orientation along the path of the photon, the most absorbed polarization is always the same and intensity of these photons decreases at a faster rate. At the exit of the wire, photons with the most absorbed polarization are fewer than the others, leading to a dichroic signal which is of opposite sign in the shadow. The curve in Figure 3.7a illustrates the local absorption that is proportional to $I_{X,\sigma}(\mathbf{r})$ multiplied by the dichroic ratio. The maximum of the absorption corresponds to the center of the shadow for which the length of magnetic material is the largest. The curves in the shadow of both the X-ray intensity and XMCD contrast exhibit a mirror symmetry, with the two maxima at the edges where the absorption is the smallest.

If the absorption is large enough, for example if the diameter is large enough, the imbalance of the remaining photons at the back side of the wire increases and outweighs the dichroic ratio. This leads to a contrast with opposite sign at the back side of the wire although $\hat{\mathbf{k}} \cdot \mathbf{m}$ is identical to that of the front side. There is a critical diameter above which the contrast reverses: $d_\mathrm{c} = \ln(\mu_+/\mu_-)/[(\mu_+ - \mu_-)\cos(16\,^\circ)]$. The $\cos 16\,^\circ$ comes from the photon direction. Indeed, the last photon which escapes wire at the back side travels a distance $d_\mathrm{c}\cos 16\,^\circ$ (see Figure 3.6d).

$$\begin{aligned} \delta^2 + x^2 &= d_\mathrm{c} \\ \sin 16\,^\circ = x/d \Rightarrow x &= d_\mathrm{c}\sin 16\,^\circ \\ \delta &= d_\mathrm{c}\cos 16\,^\circ \end{aligned} \tag{3.4}$$

The absorption coefficients μ and thus the photon energy are crucial to determine this effect. In the case of wires made of Permalloy, $\mathrm{d_c}$ is respectively 70, 140, 20 and 50 nm at the Fe-$L3$, Fe-$L2$, Ni-$L3$ and Ni-$L2$-edge. This clearly illustrates why quantitative simulation of the contrast is crucial for the analysis of experiments: the contrast may not be indicative of the local magnetization, neither in magnitude nor even in sign.

Orthoradial curling

The second test case is orthoradial curling. This configuration is interesting since it is close to real magnetic distributions such as the BPW and curling at the end of a wire. Figure 3.7c shows $I_{X,\sigma}(\mathbf{r})$ and XMCD contrast for this distribution. Let us concentrate on the shadow. The right part corresponds to the top part of the wire, for which magnetization is mostly parallel to the direction of the beam and absorbs more σ^--polarized X-rays. For the left part of the shadow, it is the reverse. It corresponds to photons having gone through the bottom part of the wire, that is the part that absorbs more σ^+ than σ^- because magnetization is mostly antiparallel to the direction of the beam, hence the low intensity of I_{X,σ^+}. Center of the shadow has no XMCD contrast, as at all point through wire diameter, X-ray direction is perpendicular to magnetization. This globally bipolar contrast is thus a clear signature of the orthoradial curling. The curve of XMCD contrast (Figure 3.7c) shows a central symmetry with symmetry point at the center of the wire reflecting symmetry of the configuration. To the contrary, concerning, direct XMCD contrast at wire surface, it is maximum at the middle of the wire zone, corresponding to the top of the wire where the beam is tangent to the latter. The contrast is largely monopolar as in the case of uniform transverse magnetization, which could for instance naively be expected from a transverse wall with transverse component aligned with the beam direction. Thus, ascribing surface contrast to a TW or a BPW may remain ambiguous. Addition of shadow contrast to wire surface contrast is crucial to distinguish between the two possibilities. This again highlights the requirement for quantitative analysis.

In both the cases of transverse uniform magnetization and orthoradial curling, there is an excellent agreement between numerical procedure and analytical results (see dots and line on Figure 3.7b-c). More details about analytical XMCD-PEEM technique can be found in chap.6. Thus it is possible to go further and to compare experimental results and simulated ones. These comparisons will enable the understanding of shadow that, as seen previously, is complex and also to hint at the magnetic textures in wire.

3.4 Comparing simulations and experiments

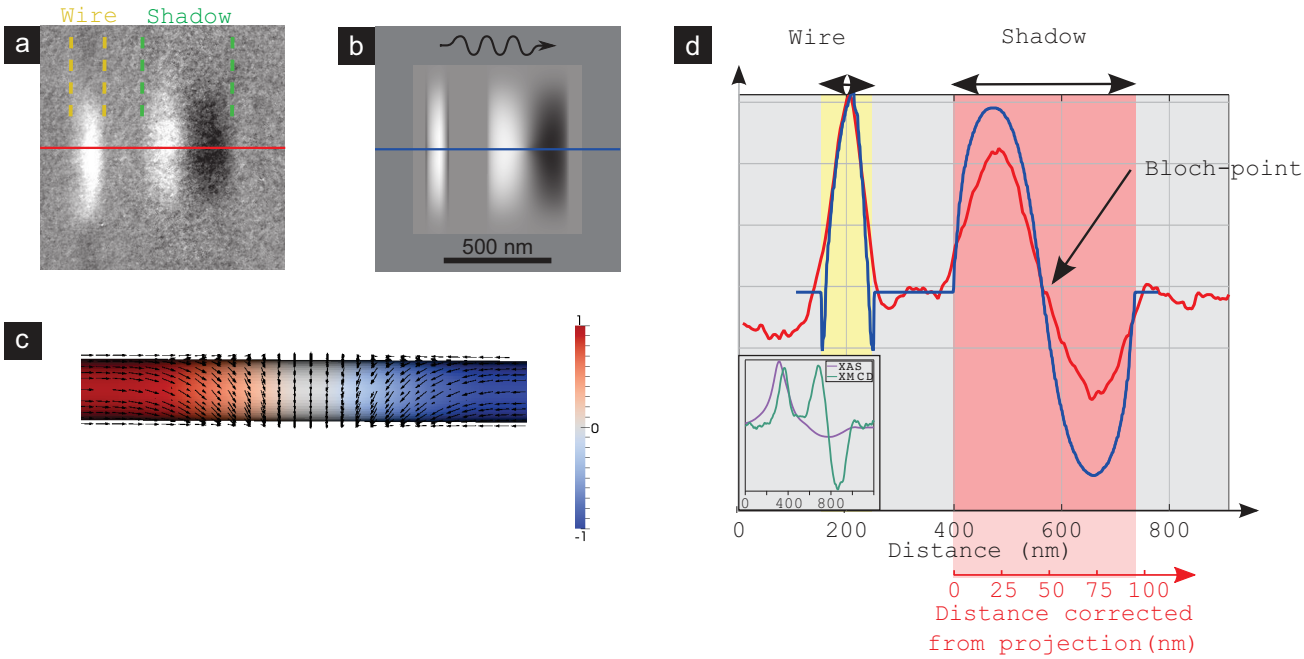

FIGURE 3.8: **Comparison of experiment and simulation for the Bloch point wall** (a) Experimental and (b) simulated contrasts at the surface and in the shadow at the Fe $L3$ edge. The wire has a diameter 90 nm. This diameter has been determined from the XAS of the wire shadow. (c) Micromagnetic simulation of a Bloch point wall, used as an input for simulating the contrast. (d) Cross-sections for (a) and (b). The inset shows the XAS and XMCD for the experimental cross section.

In this section, we will focus on the understanding of experimental contrasts (Figure 3.2e-i) and we will assign them to a type of DW. As seen previously (sec.1.2.4), two types of DWs are expected in nanowires, transverse wall for diameters below $7\Delta_d$ and BPW for larger diameters. Let us now focus on Figure 3.8, where Figure 3.8a is a zoom of Figure 3.2e. Figure 3.8b presents simulated XMCD contrast without adjustable parameters. The wire diameter and the gap between the wire and the substrate have been deduced from XAS (Figure 3.2d). BPW could be ascribed to experimental contrast Figure 3.8a. Indeed the most important signature of BPW is the bright and dark contrast in the shadow revealing an orthoradial curling. Moreover symmetry with respect to plane perpendicular to wire axis reveals a pure orthoradial curling. This feature is compatible only with BPW. A quantitative comparison can be done by using *e.g.* a cross-section (Figure 3.8d). Contrast has been normalized so that simulation and experimental maxima coincide at wire surface. There is almost perfect agreement at wire surface with a sharp peak shifted aside right from the center of the wire. This lateral shift of XAS and XMCD contrasts is illustrated on the inset of Figure 3.8d. Experimental XAS results from a convolution between the theoretical one (as on Figure 3.7c, top part) and the instrumental resolution function. As a result the maximum of XAS is left shifted compared with the maximum of XMCD contrast. In

the shadow, the contrast is antisymmetric as expected and cancels at the location that should coincide with the place of the Bloch point. Nevertheless some features do not fit so well. First, experimental contrast is wider than simulated one by about 25 nm, second, it is lower. These aspects mostly comes from experimental aspects that will be discussed later on in sec.3.5.

Let us now turn to the contrast on Figure 3.2i reproduced in Figure 3.9. It can be ascribed to transverse wall, as suggested by simulation. A signature of this is the lack of symmetry with respect to a plane perpendicular to the wire axis TW. White and black contrasts at surface, becoming a black and white contrast in shadow, arise from the curling of magnetization around the core of the transverse wall. Curling around the core of the transverse wall was expected above $7\Delta_d$ as presented in Figure 2.7b. This feature favors a magnetization as parallel as possible to the surface of the wire, preventing occurrence of surface charges. Moreover, contrast along the direction of the beam is black and white on one side and white and black on the other side of DW, revealing orthoradial curling of opposite sign on either side of DW as presented with simulations in Figure 2.7a. Finally, contrast at the center of the shadow reveals the direction of the transverse part of the DW (the vortex). As seen in Figure 3.9d, XMCD contrast is not invariant under rotation of the wire around its axis, confirming the role of the transverse component. The latter being responsible for the large contrast at the center of the shadow, azimuth of the transverse component is thus a parameter to consider to fit experimental contrast.

As suggested at the end of the section about uniform magnetization (sec.3.3.3), in case of large enough diameter, contrast should reverse at the backside of wire. This is illustrated on Figure 3.10. Profiles (Figure 3.10d-f) clearly evidence this contrast inversion which is more developed for large diameter (Figure 3.10a,d).

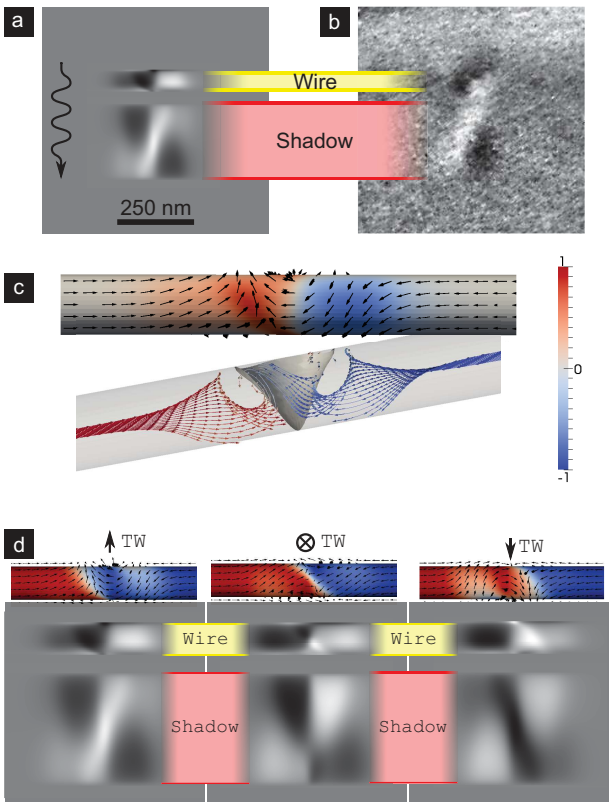

FIGURE 3.9: **Comparison of experiment and simulation for the transverse-vortex wall** (a) Simulated and (b) experimental contrasts at the surface and in the shadow at the Fe $L3$ edge. The wire has a diameter 70 nm and is lifted 25 nm above the surface. (c) Surface and open view of the micromagnetic state used for the simulation of the contrast. (d) Dependance of the simulated contrast on the azimuthal rotation the domain wall. The location and direction of the transverse core of the wall are indicated above each case.

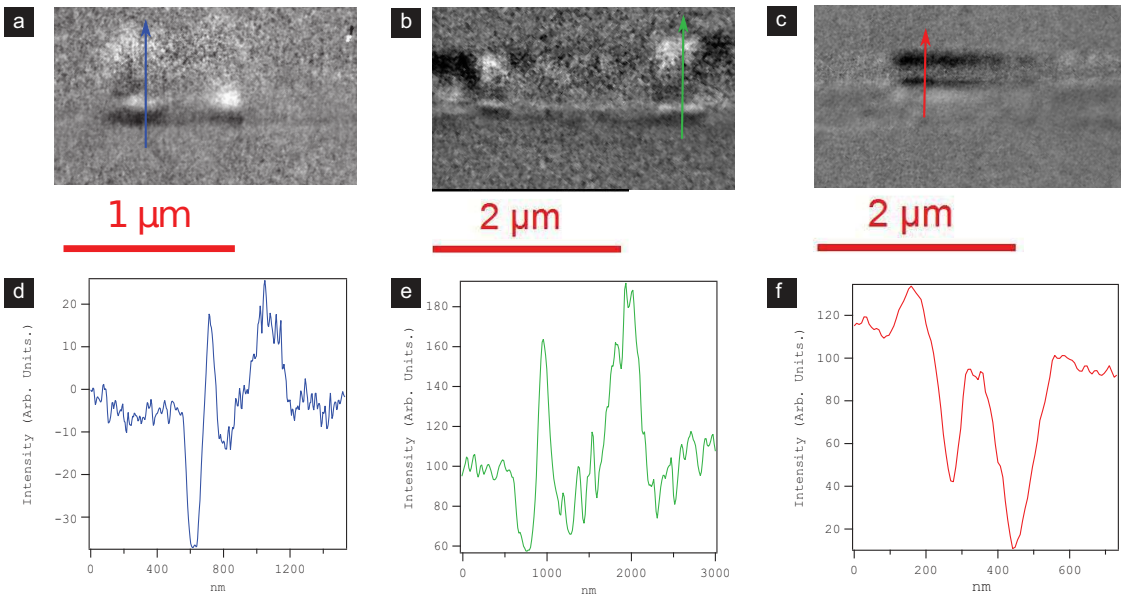

FIGURE 3.10: **Illustration of contrast inversion at the back side of wire with a BPW.** Material for the first column is $Fe_{20}Ni_{80}$. Image gathered at Ni $L3$ edge. Material for the second and third column is $Co_{40}Ni_{60}$. Images were gathered at Co $L3$ edge. Top row is XMCD contrast images. For the three images, beam comes from the bottom. The bottom row is composed of profiles of XMCD contrasts. The wire diameters, measured from XAS images are (a) 170 nm, (b) and (c) 70 nm. Shadow cannot be used since we do not have access to the whole shadow.

TABLE 3.2: Absorption coefficient values used in simulation in Figure 3.11. For image (k) they are the absorption coefficients of Fe L3 edge. For image (m), they are Fe L3 edge coefficients multiplied by 2 to keep the ratio but not the difference between μ_- and μ_+

	Image (k)	Image (m)
μ_- (nm^{-1})	0.018	0.036
μ_+ (nm^{-1})	0.01	0.02

Type of a DW in a wire is mostly determined by the need to decrease magnetostatic energy. This may lead to an orthoradial curling at wire ends, an orthoradial curling as seen in sec.1.1.3 and also "C" shape end domain. This curling had not been evidenced so far experimentally. Here we identified it as shown in Figure 3.11. Wire has been determined to be 120 nm in diameter. Extension of orthoradial curling along wire fits rather well the experimental one.

3.5 Discussion about the experimental contrast and resolution

So far, experimental settings have been stated as a possible limitation for perfect agreement between simulation and experiment. Thus, in this section more experimental details and instrumental aspects not directly included in simulation are discussed, ah they have an impact on magnetic contrast and spatial resolution.

3.5.1 Microscope settings (start voltage, plane of focus)

When dealing with flat objects, perfect focus is reached simultaneously on shadow and on surface of the object. In the present case, things are different. In principle the depth of focus of the instrument is large enough so that top of wire and supporting surface should be both in focus. In practice, however, this could not be achieved. This is ascribed to the curvature of wire,

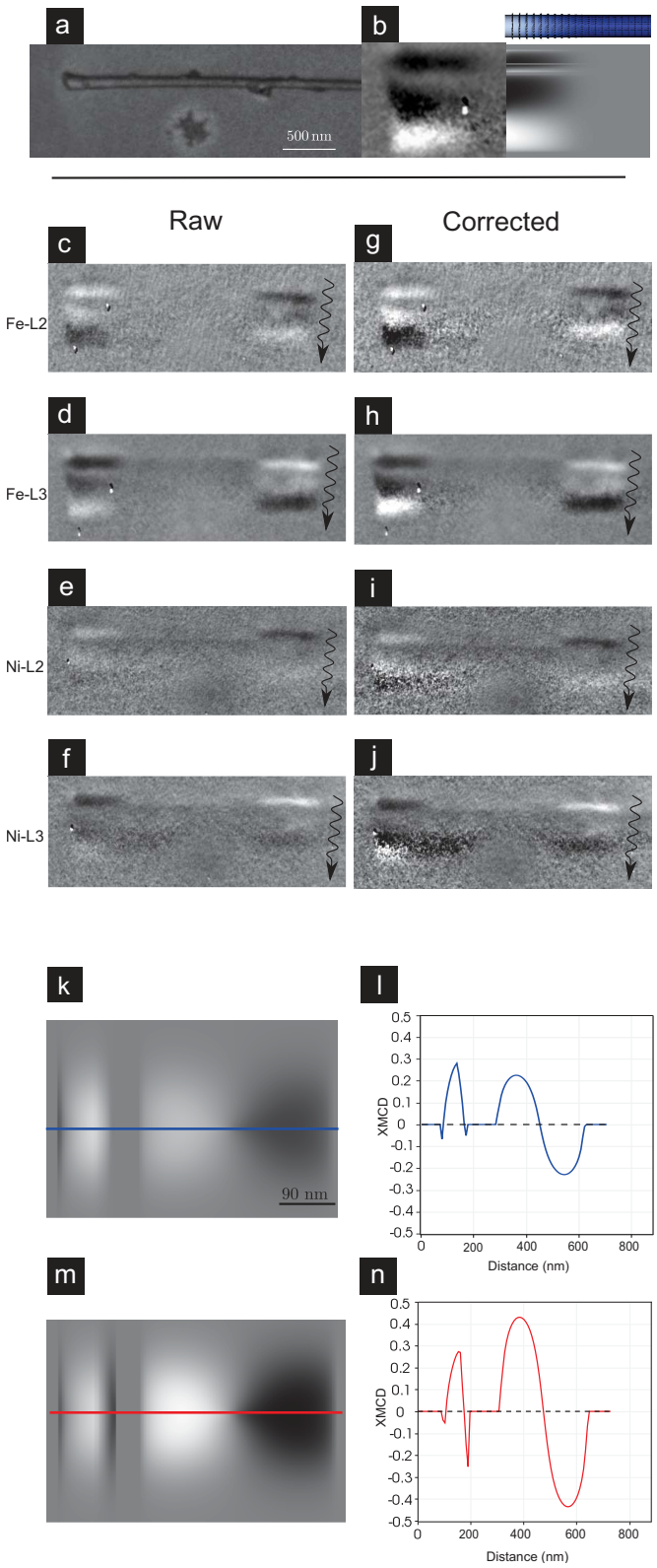

FIGURE 3.11: **Role of the absorption coefficient on contrast.** (a) LEEM image of a wire and (c)-(f) experimental XMCD contrasts of this wire. (g)-(j) are the same experimental contrasts from which background level has been removed. (b) left is the left end of (h) and to the right is a simulation of the XMCD contrast at the Fe L3 edge for a wire of 120 nm diameter with a curling at the end and corresponding micromagnetic configuration. The contrast is 6 % for (c,d,g and h), 5 % for (e and i) and 9 % for (f and j). Since for the grey scale, the intensity of the XMCD contrast $\in [-1, 1]$, if the contrast is chosen $\in [-0.06, 0.06]$, black and white correspond to 6 %. (k) and (m) Simulated XPEEM images for a 90 nm-diameter wire with a Bloch point wall (see absorption coefficients Table 3.2) and their profiles (l) and (n).

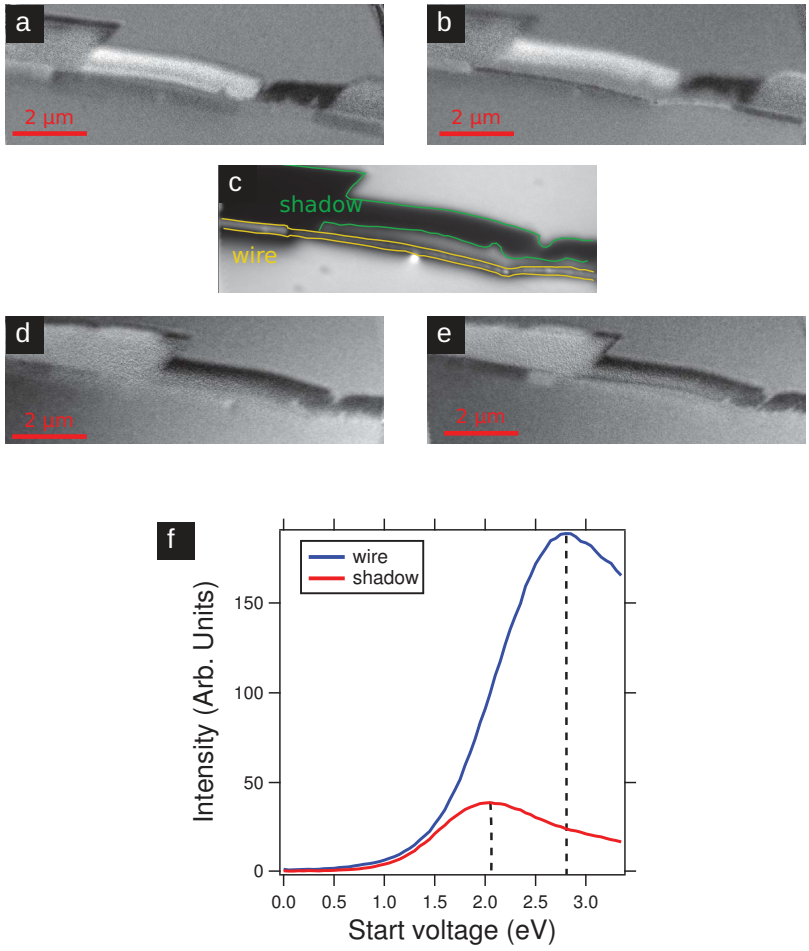

FIGURE 3.12: **Role of the plane of focus and the start voltage.** XMCD contrast is taken at Fe L3 edge, with start voltage $2.1\,\mathrm{eV}$ with a focus (a) on supporting surface and (b) on wire surface. (d) $2.0\,\mathrm{eV}$ and (e) $2.8\,\mathrm{eV}$ with a focus on surface. (c) is the sum of both helicity intensities where wire and shadow areas are highlighted to guide the eyes. (f) XAS on wire and shadow versus start voltage.

distorting trajectories of electrons leaving sample (Figure 3.6), thereby acting in itself as a lens. This lens effect can be compensated, or not, by the microscope focus, so as to set plane of focus anywhere between supporting surface and the top of wire. For instance, setting plane of focus on supporting surface has an effect on XAS and XMCD contrasts with a loss of sharpness as shown in Figure 3.12a. On the reverse it is possible to focus on wire (Figure 3.12b) loosing sharpness on shadow. The difference is more striking on wire because it has a large aspect ratio compared to surface. As we now know, in the case of highly-topographically-distorted samples as wires, both the start voltage and the focus may be tuned to get the best contrast either the wire or the shadow. These two settings are linked. Let us explain what is start voltage. Inside microscope, a high voltage is used to extract electrons. Here high voltage means 18 keV-STV (18 keV in the case of ELETTRA). Start voltage (STV) is the voltage bias on sample. In PEEM, a negative start voltage prevent from extraction of electrons while a positive one selects electrons with a given kinetic energy. The higher the STV the lower the difference in focus. As an example, with a STV of 3 eV the difference in focus is of 1 mA whereas it is 4.2 mA for a STV of 1.5 eV (see Figure 3.13). Unit for the focus is the mA because almost all lenses of the microscope are electromagnetic lenses, thus they work with coils. Coils are disposed so as to create a magnetic field with a rotational symmetry which does electron to converge. These lenses work by controlling current through coils. As a comparison, for an optical lens, to adjust focus, one adjusts sample-lens distance. For an electromagnetic lens, to adjust the focus, the parameter is the current through the coil. These images also illustrate that a higher start voltage leads to a sharpen contrast because photo-electrons are less sensitive to local variations of the surface work function, such as induced by absorbates and impurities.

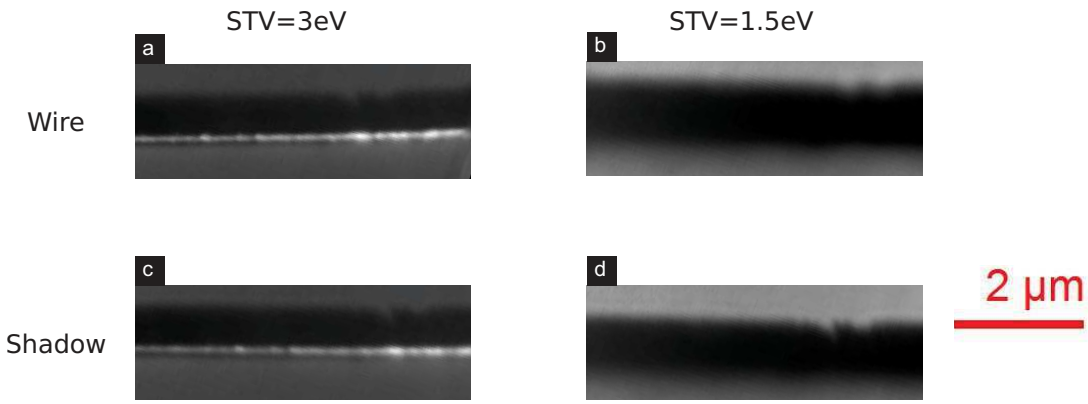

FIGURE 3.13: **Illustration of the difference of focus with the start voltage.** For all four cases, wire is a the bottom and shadow at the top. For the first column, STV = 3 eV, for the second column, STV = 1.5 eV. For the first row, focus is set on the wire whereas it is set on the shadow for the bottom row. The difference is 1 mA at 3 eV and 4.2 mA at 1.5 eV. In (b) and (d) the wire is not visible. Let us have a look at Figure 3.12f to compare the intensity at each STV for the wire and the substrate.

This may explain why the image quality both in the wire and in the shadow is better in Figure 3.12e than Figure 3.12d.

A fine tuning of STV may also be used to examine more precisely either the wire or the shadow. Indeed each material has a different work function. Whether we are interested in the Si supporting surface or the Py wire surface, STV may be tuned. In the present case, a lower STV ($\approx$ 2.0 eV) maximizes the number of electrons from shadow whereas a higher STV ($\approx$ 2.8 eV) gives rise to a higher intensity from wire. In principle, this difference of STV should be visible only on XAS image that results directly from measured electrons. To the contrary, an XMCD image results from the difference normalized to the sum of intensities should thus not depend on the number of electrons and not be influenced by the choice of the start voltage. However experiment differs from theory and in practice a lower number of electrons reduces the XMCD

signal as will be discussed in sec.3.5.3.

3.5.2 Photon energy

Let us first discuss the procedure to set the photon energy to maximize XCMD. We have seen previously that for $3d$ ferromagnetic materials, $L3$ edges give rise to a higher magnetic contrast than $L2$ edges. Thus we worked mostly at $L3$ edges. Note that surface oxidation, no matter how small it is, gives rise to a secondary peak close to the $L3$ principal peak and slightly shifts its maximum compared to the metallic spectra (Figure 3.2a). As the XMCD signal is maximum at the metal peak energy, it is important to determine the latter precisely. To do this experimentally we deemed more relevant to measure the absorption spectra from the shadow to set the working energy. Indeed, in this case photons probe the bulk of the wire, with mostly no oxidation. In principle spectra gathered at the wire surface and in the shadow should be mirror images of one another, with peaks at the L edges for the former, and dips for the latter. In practice, we notice that these two spectra at the Fe $L3$ edge differ significantly, in shape and position. We understand this as resulting from surface oxidation for the peak at the wire surface, while the spectrum in the shadow mostly reflects Fe in the core of the wire, with no oxidation. To the contrary, both spectra are very similar for Ni. This gives the picture of wire with a nm-thin oxide crust at its surface, largely enriched in Fe, around a metallic $Fe_{20}Ni_{80}$ core. Notice that Fe enrichment at surfaces upon oxidation is a usual process for FeNi alloys [88]. In the end, it remains that the photon energy must be determined from the spectra in the shadow, to maximize XMCD contrast.

Second, we consider the relative contrasts at the Fe and Ni edges. Let us consider XMCD contrast on wire. Theoretically we expect the contrast to be slightly better at the Ni $L3$ edge than at the Fe $L3$ one as dichroism is larger at Ni $L3$ edge than at Fe $L3$ edge as presented by $\Delta\mu$ in Table 3.1. However, in practice we worked at the Fe $L3$ edge which gives rise to a larger dichroic signal than the Ni $L3$ edge for both wire surface and shadow since the resulting contrast is larger (see the last column of Table 3.1). This will be explained later in sec.3.5.3, and related to the existence of a background level.

Third, let us highlight the impact of the choice of an absorption spectrum on distribution features of XMCD contrast. According to what has been explained previously, a positive contrast at wire surface is associated with a negative one on shadow. Indeed, a large absorption and thus a loss of photons of a given helicity is associated with an enhanced number of secondary electrons.

The number of photons going through wire is related to the dimensionless quantity $d\mu_{\pm}$ with d the wire diameter. In case of large absorption, we can expect, for example, a contrast inversion at back side of the wire. This contrast inversion is visible depending on the simulated edges Figure 3.11(k,m). However, experimentally, due to spatial resolution, it is difficult to see this contrast inversion. Certainly, it is visible at high resolution and for wires with large diameter as presented in Figure 3.13. Finally, we expect the contrast in the shadow to be reinforced and even to diverge for $\mu d \to \infty$, at the Ni edge. Yet, it is not the case. This will be explained in the following section.

3.5.3 Background level in PEEM imaging

Theory shows that for high value of μd, and also of the difference $\mu_+ - \mu_-$, it is possible to reach increasing values of XMCD contrast in the shadow. However this theoretical expectation comes at the expense of a much reduced intensity of the number of photons. This is the principle of some polarizers, for example for the helicity of X-rays [89] or spin of electrons [90]. In practice, an experimental effect limits the contrast. If we examine Figure 3.14 we see that for a broad wire, for which $\mu d \gg 1$, intensity in the shadow reaches a plateau and remains of the order of 15 % of the intensity over the free supporting surface. Since the background level of the camera is already subtracted from images, this intensity results from electrons really impinging on the detector. This background was found to be weakly affected by settings of the LEEM,

in particular the aperture of the field of view. The contrast aperture, affecting the angular collection of microscope, does not have a sizeable effect either. This is an a priori mostly helicity-independent background $I_{e,\mathrm{b}}$, that thus reduces the computed XMCD contrast. Indeed, in the XMCD computed so far, I_b does not appear in the difference of intensities at the numerator but is summed in the denominator. If $I_{e,\mathrm{b}}$ is determined it is possible to get a more accurate value of the true XMCD by computing: $I_{\mathrm{XMCD},0} = (I_{e,\sigma_-} - I_{e,\sigma_+})/(I_{e,\sigma_-} + I_{e,\sigma_+} - 2I_{e,\mathrm{b}})$. Figure 3.11 presents raw data in the first column, and values corrected from the background level in the second column. In these, it is striking that contrast in the shadow is higher in the corrected images than in the raw ones, as expected from theory. This increase of the contrast in shadow by removing the background level can be a reason to explain the difference of contrast in the shadow between experiment and simulation (Figure 3.8d). These contrasts also explain why working at the Fe edges yields a higher contrast than at the Ni edges, whereas a similar contrast would be expected for Permalloy as computed from the tabulated absorption coefficients (Table 3.1). This results from the large number of photons absorbed at the Fe edges, and thus the background level is smaller in relative value. Nevertheless, the signal over noise ratio is poorer in the case of Ni, an issue discussed below.

As discussed before, the shadow is more reliable to gather information because, for instance, it is relatively distortion-free. Moreover, the spatial resolution in this area is increased by a factor $1/\sin(16\,^\circ) \approx 3.6$ along the beam direction thanks to the projection with a grazing angle, bringing the resolution to 10 nm. However the limited number of photons collected in shadow is a practical limitation to this gain. The number of collected photons in shadow is sharply reduced due to absorption. Thus, if a better resolution is needed, one has to increase the acquisition time. However it is to be noted that the acquisition time is an optimum. A too short time offers the advantage of a small drift but also a small number of electrons collected. Thus the noise is high and drift correction is difficult to compute. To the contrary a long acquisition time gives rise to a large number of electrons but the drift is so huge that the correction cannot remove it.

3.5.4 Scattering effects

So far we have considered propagation in geometrical optics, neglecting scattering. In general interaction of X-rays with matter can be described via complex atomic scattering factors. Real and imaginary parts give rise to the Faraday rotation of photon polarization vector and to magnetic dichroism, respectively, as the photon beam propagates through magnetic material. The two are related by the Kramers-Kronig relation, and they are comparable in magnitude at the Fe L3 edge [91]. Until now, we have considered only the X-ray absorption coefficient, which is proportional to the imaginary part of the forward scattering amplitude via the optical theorem [92]. Instead, as we noted above, a proper treatment should include the full scattering process. Indeed, intensity oscillations near the edge of the shadow are visible in Figure 3.14 due to Fresnel diffraction from the wire. Furthermore, the Fresnel fringes also show a dichroic signal.

3.5.5 Electric field distortion

LEEM images of non flat surface are distorted [73] because secondary electrons escape perpendicularly to the local surface. Their trajectory is curved through the extraction voltage such that the size of a convex objects, like the ones we use, is larger than the real size. This creates a significant distortion to the outgoing low-energy electron wave. In the end there are two aspects that combine in the final image: the spherical aberrations of the objective lens (due to the angular spread of electrons), and the distorted potential profile of the topographically nonuniform sample surface. In the case of shadow XMCD-PEEM this experimental feature can be directly evidenced. Indeed we have access to the shadow of the object from which electrons escape along the electric field lines. To measure the wire diameter, the width of the shadow is divided by 3.6. The apparent width of the wire deduced from XAS was about 50 % larger than the width obtained from the shadow. Indeed, let us have a look at Figure 3.12c and compare the widths

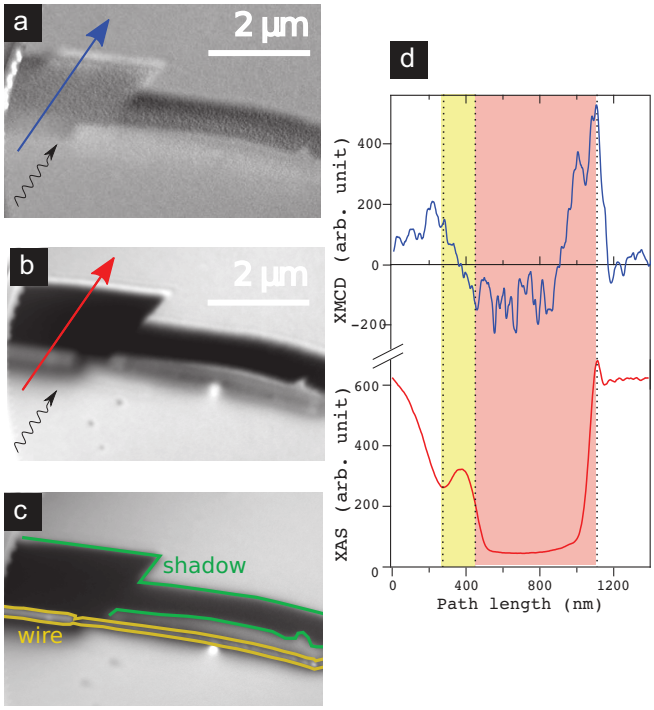

FIGURE 3.14: **Scattering effects.** Wire image of the intensity for (a) the XMCD and (b) the absorption contrast summed for both helicities. (c) shows the wire and shadow zones on the contrast images. The plot (d) presents the intensity at the cross-sections shown in (a) and (b). Dotted lines are guides to the eye and limit the wire (left, yellow) and shadow areas (right, pink)

of the wire measured with the shadow and directly on the wire. The former gives a diameter of 57 nm while the latter is 70 nm. But we can also compare these widths and the impact of the STV on the width measured directly on the wire. The wire diameters we get through this procedure are those we keep as relevant and use as input for the simulations. Notice this method to gather the size of the nanostructure is possible only for objects that are slightly above the supporting surface in order to split the contrast arising from the wire and from the shadow and then measure the whole shadow.

3.6 Conclusion

The shadow XMCD-PEEM provides a surface and volume information about magnetization, which is of great importance to solve complex magnetic configurations. Moreover, the increase of spatial resolution thanks to the use of shadow makes this method unique. To help identification of DW, a simulation tool has been developed. Starting from micromagnetic configurations, we get a XMCD contrast. Simple test cases helped the understanding of the experimental contrast. Then simulated contrasts from simulated micromagnetic configuration help to distinguish between a TVW and a BPW. A comparison between experiments and simulations leads to a good qualitative agreement. Quantitative differences come from, for example, as presented in Figure 3.8, a background level that is difficult to quantify. The last part with a study of the impact of plane of focus, extraction voltage, background level and electric field distortion enables to extract the true structure as well as the contrast. Due to curved surface, plane of focus can be set between substrate and wire surface. The background level can be measured directly on images and subtracted to get the contrast free from background. More details about the simulated contrast can be found in chap.6

Chapter 4

Conclusion

The study of domain walls in nanowires has known a rising interest after the proposition of IBM for a three dimension race track memory. In this application, bits are made of DWs. Further than application to device, many physical features related to these DWs are of interest.

There remains many physical and numerical features to study about DWs in nanowires. Nevertheless, we pursue the phase diagram of magnetic DWs for a geometry ranging from nanostrips to nanowires. The first and second order phase transition lines have been traced up to diagonal of the diagram. However, the second-order transition line between TVW and ATW does not continue until diagonal. Indeed, the latter is not a steady state for wires over the range of tested geometries, that is until a diameter of 150 nm. The Bloch point wall, predicted for nanowires of square or disk-based cross section, extends its existence and stability domain around the diagonal. Moreover, above $7\Delta_{\mathrm{d}}$ for TVW, both transverse and longitudinal curling rise, the former around the transverse component, the latter along the wire axis. These two directions of curling appear as a method to decrease the dipolar energy for large diameter nanowires. This aspect is an explanation for the stability of the BPW around the diagonal, the system preferring to close its magnetic flux as soon as its dimensions are suitable. The curling appears as a more efficient method to decrease the magnetostatic energy than the asymmetry. Moreover, a scaling law for the DW width has been derived.

The study of DWs continues with their imaging. To get a sufficient spatial resolution, chosen technique is XMCD-PEEM. XMCD-PEEM imaging of these nanowires of disk-based cross section has been done three times during my thesis. Experimental conditions, with a 16 ° grazing angle enables to access the shadow of the wire. This imaging technique is made possible for suspended wires, by the fact that they are bent or they have ends with larger diameter. This shadow contains information about volume magnetization, averaged along path of X-ray. This technique thus combines a surface imaging and a volume averaged imaging.

To help the understanding of this complicated contrast, a simulation tool has been developed. This tool enables to discriminate between a TVW and a BPW, which is currently not possible using the MFM technique. We can thus assert the Bloch point wall has been observed for the first time. Comparison between simulated contrasts and experimental ones yields a good qualitative agreement. Quantitative differences may come from, for example, background signal in the shadow. This signal is to be evaluated for each set of images.

Experimental settings such as the extracting voltage, plane of focus, background level, have been studied to help to get physical relevant magnetic contrast.

The study of DWs propagation under magnetic field is part of the thesis of Alexis Wartelle. Connection between BPW circulation and direction of applied field has been confirmed. Numerical study of this propagation will be part of the thesis of Beatrix Trapp.

Chapter 5

Perspectives

In the framework of a device-oriented work we are interested in structured wires that enable to control DW motion. Production of wires with diameter modulations along wire are ongoing work (joined work between Néel Institute, University of Erlangen and Smart Membrane). We are interested in BPW since this DW is the fastest under an applied magnetic field. These wires need to be correctly dimensioned to ensure nucleation of a BPW and not TVW. In that way, the phase diagram tells us to use wires with diameters larger than 35 nm. But due to the metastability, we chose a diameter of 70 nm.

A wire included in such a device has a modulated diameter along wire axis, either protrusions or constrictions. The former acts as potential barrier. The latter is a potential well for DWs. Applied magnetic field will be used either to make DW go through protrusion or to depin DW from potential well. Thanks to the application of the magnetic field, the DW is moved to the next diameter modulation. Several field values are to be considered. There is the steady state regime field accompanied with a high speed, the minimum field to propagate a DW and the minimum field to depin a DW. Gaussian distributions are to be considered for both latter fields. The propagation fields have to be sufficiently lower than the depinning fields so that a DW is only propagated along wire and does not go through diameter modulations.

For this work, there are currently three main steps. First, to plot $v = f(H_{\text{applied}})$. Second, we will study influence of diameter modulation shape on depinning field. Third, each field values will be chosen so that a DW goes through one modulation at a time.

Plot of speed versus applied field has already been done by Thiaville *et al.* [2]. However the considered system is a square-based nanowire with a side of 40 nm, and field to apply to reach steady state regime differs according to geometry. To study dynamics, simulations were performed using the DW moving frame formulation. Indeed, this is an alternative solution to very long wires, the latter requiring computing power and memory. To prevent nucleation of DW from the ends of wire, $\alpha = 1$-zones have been added in order to dissipate energy. Fields were applied with a step-wise function from 1 to 10 mT.

However, problems occur at this step. After a given number of iterations, DW speed does not evolve linearly with time. Number of iterations leading to the change of behavior increases with field. After this change of behavior, DW moves slower, with some bumps. Close looks at micromagnetic configurations at long time show these configurations are much more complicated than a BPW. Systems develop spin waves without cylindrical symmetry (cork-screw shape). Moreover, wire averaged components m_x and m_y show temporal oscillations. Frequencies of these oscillations change between the beginning and the end of the simulation meaning there is a frequency for the first regime and for the second, complex, regime. However it is not clear whether the change of frequency is directly linked with DW or whether it is related to spin waves.

A second set of simulations included some modifications. All modifications were done separately in order to get the impact for each of them. First, instead of using a step-wise function

for the applied field, we use a linear function with a rising time of 3.5 ns. With this method, closer to experimental conditions, energy is not added too fast to the system. Second, influence of mesh size has to be properly studied. Third, a simulation was done using the laboratory frame.

Use of linear function for the applied only delayed the change of behavior and time oscillations of m_x and m_y are still there. A finer mesh gives rise to better results. However, even at the beginning, behaviors differ. The finest mesh gives rise to a higher speed. Finally, when using laboratory frame, DW exits wire before any clear change in motion is visible.

After this set of simulations we can bring some conclusions. The use of a three segment wire with abrupt α-changes is not a relevant solution. This sharp variation acts as a mirror reflecting spin waves instead of dissipating energy. We already knew BPW may raise some problems since magnetization norm is not kept. BPW thus tries to remain at the center of the cell, as close as possible to the wire axis so as to limit dipolar field. However, it is not feasible due to mesh structure (no cell centered on wire at each mesh layer). As a result, the Bloch point jumps from one cell to another around the wire axis which might be an explanation of m_x and m_y oscillations. These jumps can be exacerbated by the reflected spin waves which disturb the system. Moreover, to check influence of spin waves on oscillation frequencies, a method is to time average magnetization over the DW only.

We face two possible problems. First, there are numerical problems, mainly due to interaction between mesh and Bloch point. Second, we need to learn more about dynamical and physical aspects of an orthoradial curling configuration in cylindrical geometry. To solve these problems, we can study them separately. First, we can work with tubes which do not present Bloch points. Then, we can compare oscillation periods of m_x and m_y for a tube and a wire with similar configurations. Third, we can study the gyrotropic precession of DW within a tube applying a transverse field then let the system to relax. This precession does not depend on the Bloch point. Finally, to study the behavior of an orthoradial curling with an applied magnetic field, we can apply a longitudinal field.

Gyrotropic precession is studied in tube. A transverse to wire field (along x) of 50 mT is applied with a rising time of 3.5 nsec. Once the system reaches its steady state with a no more increasing x-component, the field is switched off and system relaxes. Relaxation starts with oscillations of the transverse components of the magnetization, m_x and m_y. DW moves then is reflected with a high increase of energy. Spin waves and problems at boundaries are certainly responsible for this reflection.

This new set of simulations reflects it remains problems with spin waves. They are not absorbed at the end of tubes and wires because they bring too much energy. A solution to solve this remaining problem is to develop α-matching in the same way as impedance matching.

Another crucial point needs to be investigated to better understand the simulation results. A close look at micromagnetic simulations at various times show variations from the classic configuration of a BPW. It is not even clear whether BPW still lies within wire. This means BPW may have been transformed into another type of DW. To solve this question, a code is being developed by C. Thirion and myself. The goal is to track a BPW at each simulation iteration. The physical quantity used for this tracking is the winding number. To each type of DW is associated a winding number so that, by implementing the temporal computing of winding number, we will be able to assert if the DW is a BPW or of another type. This tool is crucial to understand results of BPW simulations.

Chapter 6

Appendix

This appendix presents in details numerical developments done during my thesis. They concern the homemade finite element code FeeLLGood but also numerical tools used for the phase diagram and the simulated XMCD contrast.
The first part concerns FeeLLGood. The calculation of the demagnetizing field has been optimized thanks to the use of a new library. The other point is related to a new formulation implemented in FeeLLGood in order to work in the DW moving frame. Both developments have been developed by Jean-Christophe Toussaint then tested and used by me.
The second part is dedicated to numerical tools. First we present the ray tracing method used to simulate the XMCD contrast as well as surface magnetization maps, domain wall widths or estimations of the curl of the magnetization for the phase diagram. The ray tracing has been developed by Jean-Christophe Toussaint and some improvements were brought by me. I developed the numerical tools associated to the ray tracing.
The third part about the simulation of the MFM contrast has been developed before my thesis by Jean-Christophe Toussaint. I added the possibility to rotate the wire and designed the surface simulating the tip path over the wire.

A Some FeeLLGood modifications

A - 1 Speed optimization of the demagnetizing field calculation

We explained (sec.1.1.1) that demagnetizing energy, due to the long range of dipolar interactions, is computing-time consuming. A possibility to improve its computing time is to find a faster method to implement the fast multipole method (sec.1.3.2). Idea is to parallelize expansion calculation (computing of moments) for each level of the dyadic partition in FMM. In the next step, we collect all information corresponding to one level. Then we proceed to the expansion at a higher level. ScalFMM library is used for this improvement, developed by INRIA (French National Institute for Research in Computing and Automatism) [93]. As a result, computing time of demagnetizing field is ten times smaller than with the previous library (Kifmm 3D package [94]). Currently the most time consuming step is assembling of elementary matrices in finite element part.

A - 2 Modification of the formulation used in FeeLLGood: framework with the domain wall

When using numerical methods, some compromises have to be made, for instance between simulations with a mesh a fine as possible or a very fast simulation. Another problem arises when one is interested in domain wall propagation.

In that case, to limit the boundary effects, one can use very long wires (several micrometers) to enable the DW to propagate. However this method requires large computing resources in

power and memory. The most convenient solution is to find an alternative method. In that sense, we chose to bring some modifications to the formulation used in FeeLLGood (sec.1.3.3). Idea is to introduce a moving frame to keep DW centered during dynamics so that there is no need to use very long wires. This method is similar as adding a field that moves the DW backward. A motion of the mesh itself can be implemented however this method raises some problems. First, mesh is redefined at each step which requires a lot of computing time. Second, there are artifacts due to the interaction between the mesh and the micromagnetic configuration. An alternative method, without moving the mesh, is presented here:

Let us start from the Alouges formulation (see p.44):

$$\alpha \mathbf{v} + \mathbf{m} \times \mathbf{v} = \mathbf{H} - \lambda \mathbf{m} \tag{6.1}$$

where λ is the Lagrange multiplier and $\mathbf{H}$ is the effective field.

First, we project Eq. 6.7 onto a test function $\mathbf{w}$ in the tangent plane of $\mathbf{m}^n$. We are looking for $\mathbf{v}$ in the tangent plane such that:

$$\int \alpha \mathbf{w} \cdot \mathbf{v} + \int \mathbf{w} \cdot (\mathbf{m}^{n,\theta} \times \mathbf{v}) = \int \mathbf{w} \cdot \mathbf{H}^{n,\theta} - \int (\mathbf{m}^{n,\theta} \cdot \mathbf{H}^{n,\theta}) \mathbf{w} \cdot \mathbf{m}^{n,\theta} \tag{6.2}$$

where $\mathbf{m}^{n,\theta} = \mathbf{m}^n + \theta \Delta t \mathbf{v}$. We linearize $\mathbf{H}^{n,\theta} = \mathbf{H}^n + \theta \Delta t v \; \partial_m \mathbf{H}^n$.

We define $\phi(\mathbf{m}^n) = \alpha + \theta \Delta t (\mathbf{m}^n \cdot \mathbf{H}^n)$ and then get the formulation for the θ-scheme integration, neglecting terms in Δt^2:

$$\int \mathbf{w} \cdot \phi(\mathbf{m}^n) \mathbf{v} + \int \mathbf{w} \cdot (\mathbf{m}^n \times \mathbf{v}) - \theta \Delta t \int \mathbf{w} \cdot \left(\frac{\partial \mathbf{H}^n}{\partial \mathbf{m}} \mathbf{v} \right) = \int \mathbf{w} \cdot H^n \tag{6.3}$$

We can now turn to the DW moving frame. We define V_z, the instantaneous DW speed along wire axis as $V_z = \frac{L}{2} < v_z >$ with $< v_z >= \mathbf{e}_z \cdot \; < \partial_t \mathbf{m} >$, $< \partial_t \mathbf{m} >$ being the volume average of time derivative of magnetization. Modification of formulation with addition of this term leads to a transport term added to the time derivative of magnetization. We assume this term to be small and it is considered as a small perturbation because convergence of the weak formulation has not been proved with this term. Let us now write the differential of $\mathbf{m}(z,t)$:

$$\begin{aligned} \mathrm{d}\mathbf{m} &= \frac{\partial \mathbf{m}}{\partial z} \mathrm{d}z + \frac{\partial \mathbf{m}}{\partial t} \mathrm{d}t && (6.4) \\ \frac{\mathrm{d}\mathbf{m}}{\mathrm{d}t} &= \frac{\partial \mathbf{m}}{\partial z} \frac{\mathrm{d}z}{\mathrm{d}t} + \frac{\partial \mathbf{m}}{\partial t} && (6.5) \\ \frac{\mathrm{d}\mathbf{m}}{\mathrm{d}t} &= \frac{\partial \mathbf{m}}{\partial t} + \underbrace{V_z \frac{\partial \mathbf{m}}{\partial z}}_{\text{transport term}} && (6.6) \end{aligned}$$

Taking into account this term, LLG-equation reads:

$$\alpha \mathbf{v} + \mathbf{m} \times \mathbf{v} = \mathbf{H} - (\mathbf{m} \cdot \mathbf{H}) \mathbf{m} + \alpha V_z \frac{\partial \mathbf{m}}{\partial z} + V_z \mathbf{m} \times \frac{\partial \mathbf{m}}{\partial z} \tag{6.7}$$

Changing the frame of reference leads to add two new terms to the Alouges formulation. These new terms do not make use of the Lagrange multiplier since the local conservation of $\mathbf{m}$ forces $\mathbf{m} \cdot \partial_z \mathbf{m} = 0$.

We can now write the new weak formulation obtained from equation Eq. 6.3:

$$\begin{aligned}\int \mathbf{w}\cdot\phi(\mathbf{m}^n)\mathbf{v} \quad + \quad \int \mathbf{w}\cdot(\mathbf{m}^n\times\mathbf{v}) - \theta\Delta t\int \mathbf{w}.\left(\frac{\partial \mathbf{H}^n}{\partial \mathbf{m}}\mathbf{v}\right) &= \int \mathbf{w}\cdot H^n \\ +V_z^n\int \mathbf{w}\cdot(\mathbf{m}^n\times\frac{\partial \mathbf{m}^n}{\partial z}) + \alpha V_z^n\int \mathbf{w}\cdot\frac{\partial \mathbf{m}^n}{\partial z} \\ +\theta\Delta t V_z^n\int \mathbf{w}\cdot\left(\mathbf{v}\times\frac{\partial \mathbf{m}^n}{\partial z} + \mathbf{m}^n\frac{\partial \mathbf{v}}{\partial z}\right) \\ +\alpha\theta\Delta t V_z\int \mathbf{w}\cdot\frac{\partial \mathbf{v}}{\partial z} \end{aligned} \tag{6.8}$$

where three terms are added, acting as a field pushing back domain wall.

B Numerical tool development

B - 1 Ray tracing

Ray tracing tool has first been developed to mimic X-ray traveling through matter and simulate XMCD-PEEM contrast (see p.76). Jean-Christophe Toussaint developed the basis, found libraries, wrote code for grid definition. I worked on tests and improvements then post processing codes based on ray tracing.

XMCD-PEEM gives information about surface magnetization. However, as said before (chap.3), we have access to shadow reflecting volume magnetization averaged along the path of an X-ray. Thus, to simulate XMCD-PEEM technique, magnetization is computed at any location inside sample, which has been achieved with this code. Since it appeared this method is very powerful, it has also been used in other post-processing codes. For example, it proved useful to compute domain wall width or to get surface magnetization maps, in the chapter dedicated to the phase diagram (see Chap 2).

Let us explain the method implemented for XMCD contrast. Other methods will be detailed below but they are based on a similar principle. Consider a ray launched from a source that is a regular planar grid. Numerical description of a grid (Figure 3.5), using Boost library [95], is:

```
struct Grid{
 Point G;
 int Nu, Nv;
 double Lu, Lv;
 double Scell;
 double focal;
 Vector ng;
 Vector tu;
 Vector tv;
 Cell_array cells;
};


Grid source;

source.focal=120*SCALE; // SCALE is the unit
source.Nu=1024;
source.Nv=1024;

source.cells.resize(boost::extents[source.Nu][source.Nv]);
```

```
cout << source.cells.shape()[0] << " " << source.cells.shape()[1]
    <<endl;

double theta=16.*M_PI/180.;
source.ng=Vector(+cos(theta), -sin(theta), 0.);
source.tu=Vector(+sin(theta), +cos(theta), 0.);
source.tv=CGAL::cross_product(source.ng, source.tu);
source.G=Point(fem.cx-source.focal*source.ng.cartesian(0)-fem.lx
    /3.,
        fem.cy-source.focal*source.ng.cartesian(1),
        fem.cz-source.focal*source.ng.cartesian(2));

source.Lu=280.*SCALE;
source.Lv=700.*SCALE;
```

LISTING 6.1: **Example of the definition of a grid**

Same template is used to define the other grids (substrate grid and detector grid). Numerical description of ray is done using geometry toolbox library CGAL [96]. A kernel K is used to model Euclidean geometry. With this kernel, we can use object of type `Ray_3` which is a directed straight ray in the three-dimensional Euclidean space E^3. This ray starts from a point source and goes to infinity. The first step is to find intersection points between ray and external surface of nanostructure, called P_{in} and P_{out} (see Figure 6.1a). To compute this intersection point, a function `search_intersections` has been developed, using CGAL objects. Next step is to determine surface element (triangular) to which theses points belong. Let us take the example of P_{in} point. To find the correct triangle, principle is to find a given number of P_{in} nearest neighbors and surface element to which they belong. Then we compute surface of surface element delimited by nodes of these faces and P_{in}, the latter be it in (Figure 6.1d) or out (Figure 6.1c) of the face. Here is an algorithm of principle:

```
Find the 10 nearest nodes TMP(ie) to P_in
Put them into an array
Associate its face Fac(ie) to each nearest neighbor TMP(ie)
To create a three-component vector V(i), between P_in and the 3
    nodes NOD(i) of Fac(ie)
Loop over the faces
   Create a vector C
   Loop over the three nodes NOD of the a face:
      C(i) = cross product between V(i) and V(i+1)
   End loop
   S = 1/2 * (norm of each C vectors)
   If (S /surface of the face < 1)
     then this is the right face
   Endif
End loop
```

LISTING 6.2: **Algorithm of principle to find the face to which the intersection point belongs**

Using the ANN library [97], this algorithm is implemented in C++ as follows:

```
void intercept_facet(Fem& fem, Point_List& point_list, Facet2Pt &
    facet2pt, ANNkd_tree* &triangles_kdTree){

for (std::list<Point>::const_iterator it=point_list.begin(); it !=
     point_list.end(); ++it){
  Point P0=*it;
  ANNpoint queryPt = annAllocPt(3);    // allocate query point
  queryPt[0]=P0.cartesian(0);
  queryPt[1]=P0.cartesian(1);
  queryPt[2]=P0.cartesian(2);

    int NPS=10;

  ANNidx id[NPS];    // allocate near neighbor indices
  ANNdist distsq[NPS];    // allocate near neighbor dists

  triangles_kdTree->annkSearch(queryPt, NPS, id, distsq, 0.);    //
      ANN function to find nearest nodes of mesh

    bool found=false;
    for (int nps=0; nps<NPS; nps++){
      Fac &fac = fem.fac[id[nps]];

      Vector V[Fac::N]; // vector with a number of components equal to number of
          face nodes
      for (int ie=0; ie<Fac::N; ie++){
        int i=fac.ind[ie]; //change of numbering
           Node &node = fem.node[i];
        Point tmp(node.x, node.y, node.z);
           V[ie]=Vector(P0, tmp);
        }
      double Sp[Fac::N], St=0.;
      for (int ie=0; ie<Fac::N; ie++){
        Vector C = cross_product(V[(ie+1)%3], V[(ie+2)%3]);
        Sp[ie] = 0.5*sqrt(C.squared_length()); // surface of one sub-
            triangle
        St += Sp[ie]; // total sum of all normalized sub-surfaces
        }
      double r=St/fac.surf;
      const double eps=1e-6;
      if (r<1.+eps)// comparison between surface of face [ind(nps)] and the one
          delimited with P0
         facet2pt[id[nps]]=P0;
         found=true;
         }
      if (found) break;
      }//endfor nps
  }
if ((facet2pt.size()>0) && (facet2pt.size()!=2)) {
    cout << "WARNING nb intersections : " << facet2pt.size() <<
        endl;
    }
}
```

Listing 6.3: **Example of C++ code to find the face to which a point belongs using ANN library**

At these intersection points, magnetization is interpolated from nodal values of triangle (face) to which they belong using a method based on the areal coordinates method [98]. For that, triangle with three nodes (I, II, III) is divided into sub-triangles with a common vertex P_{in} (see Figure 6.1d). Then, the polynomials used for the interpolation of the magnetization are calculated such that the one associated to node I is the ratio between surface of the sub-triangle (P_{in}, II, III) and the total surface of triangle (I, II, III) (Figure 6.1d). Same method is applied for the other two nodes. Algorithm of principle for this method is:

```
N = 3 is the number of nodes of the cell
d = 3 is the dimension of the space
Loop over N nodes of a face:
   Create a vector between P and the node n
   Create a vector C(n) of d components
   C(n) = cross product between Pin and TMP(n)
   S(n) = 1/2 * square root( C(n))
   Stot += S(n)
end loop

Create a N component vector A (interpolation polynomials)
Loop over each components of A:
   A(n)=S(n)/Stot
   Loop over the N nodes of the face
      up(d)+=A(n)*(component d of magnetization at node n) //
          Creation of d component magnetization vector up at P
   end loop
end loop
```

Listing 6.4: **Algorithm of principle for the areal coordinates method for interpolation of magnetization**

The implementation of this algorithm in C++ reads:

```
/*-MAGNETIZATION INTERPOLATION FOR TRIANGLE -*/
void interpol(Fem &fem, Fac &fac, Point P, triple &up){

Vector V[Fac::N];

//gather coordinates of triangle vertices
for (int ie=0; ie<Fac::N; ie++){
   int i = fac.ind[ie]; //from global to local numbering
   Node &node = fem.node[i];
   Point tmp(node.x, node.y, node.z);
   V[ie]=Vector(P, tmp);
   }

double Sp[Fac::N], St=0.;
for (int ie=0; ie<Fac::N; ie++){ // loop over all face nodes
   Vector C = cross_product(V[(ie+1)%3], V[(ie+2)%3]);
   Sp[ie] = 0.5*sqrt(C.squared_length()); // surface of sub-triangle
```

```
18     St += Sp[ie]; // total surface
19     }
20
21  double alpha[Fac::N];
22  for (int ie=0; ie<Fac::N; ie++){
23     alpha[ie]= Sp[ie]/St; // new lagrangian polynomial
24     }
25
26  up[0]=up[1]=up[2]=0.;
27  for (int ie=0; ie<Fac::N; ie++){
28     int i = fac.ind[ie]; //global numbering of the ith node
29     Node &node = fem.node[i];
30
31     for (int d=0; d<3; d++){ //magnetization at each node
32        up[d] += alpha[ie]*node.u[d];
33       }
34     }
35  }
```

Listing 6.5: **C++ implementation of the areal coordinates method for a triangle**

In order to calculate absorption along ray, the latter is discretized into segments of a chosen length between P_{in} and P_{out}. For each discretization point, first, we determine element (tetrahedron in volume of wire, see Figure 6.1b) to which point belongs. Second, magnetization is interpolated with the method previously described but with four nodes and making use of sub-tetrahedrons instead of sub-triangles. Sub-triangles are only used for elements at surface of wire, thus for entering and exit points.

Implementation has been done by using the geometry toolbox library CGAL [96] for rays, and the nearest neighbourg searching library ANN [97].

B - 2 Surface magnetization maps

We work with configurations in three dimensions where space of coordinates and magnetization vector have three coordinates. These configurations are difficult to present. Thus several displays must be used. Some of them are provided by softwares such as Paraview [99] or Visit [100], AVS [101]. These displays can become crucial when facing very complex structures, especially at surface. For instance when searching for asymmetric transverse wall, there is a need to know whether locations where magnetic flux enters and exits are located on a same plane perpendicular to the wire axis. The goal is thus to get a 2D image of magnetization at wire surface.

There exists alternative methods to get surface magnetization. One can think, for example, of searching only for surface elements of wire and compute scalar product between normal to surface and magnetization. Then it will be necessary to check if everything is saved in the proper way so that when output file is read, values of scalar product are not misplaced. This technique is much more complicated.

To compute these surface magnetization maps, wire is divided in a given number of constrictions perpendicular to the wire axis. For each one, rayss with direction $\hat{\mathbf{k}}$, are radially launched from wire axis. In that case, we are not interested in tetrahedrons the ray crosses through wire, but only in its intersection with a surface triangle (see Figure 6.2b). This triangle and magnetization at intersection are found as explained in sec.B - 1 by interpolation of the magnetization with areal coordinates. Once magnetization $\mathbf{m}$ at surface is obtained, we can be interested either in radial component of magnetization or in z component of magnetization. For the former, surface map is in plane (θ, z) where θ goes from 0 to 2π and z covers the wire length, computing the scalar product between the direction of the ray $\hat{\mathbf{k}}$ and $\mathbf{m}$, so that only the

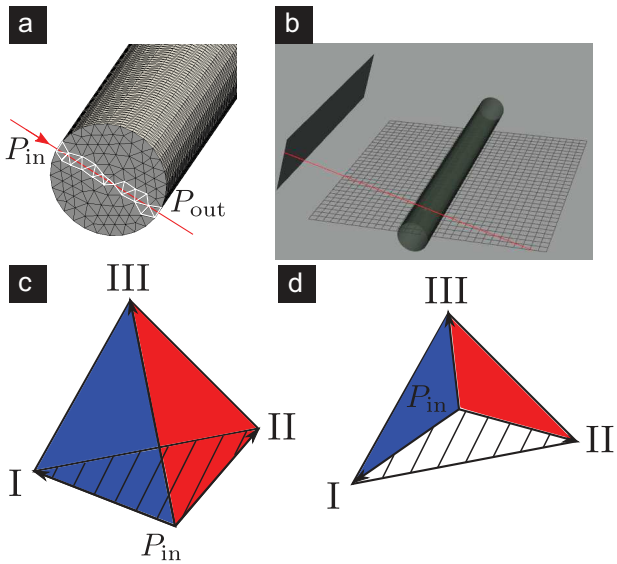

FIGURE 6.1: **Description of numerical method.** (a) presents method to model X-ray beam. Red line presents X-ray beam crossing elements (in white, from finite element discretization). Surface elements of discretized physical system are in grey. (b) shows wire on gridded substrate and photon source. (c) and (d) illustrate areal coordinate method. Blue, red and striped areas are the three triangles defined with (P_{in}, I, II, III). (c) scheme of the sub-triangles with P_{in} outside the triangle (I, II, III). (d) sub-triangle with P_{in} inside the triangle (I, II, III)

radial magnetization is kept (Figure 6.3b). It is summarized in Figure 6.2. Radial component is equivalent to local normal to surface. Principle of algorithm is the following:

```
Loop over the z position
 Loop over the angle theta from 0 to 2pi
    Definition of ray direction n_x= cos(theta) and n_y= cos(
       theta)
    Find entering and exit points of ray
    Find element to which these points belong
    Interpolation of magnetization at these points
    Scalar product between interpolated surface magnetization and
        ray
 end loop
end loop
```

LISTING 6.6: **Algorithm of principle for map of magnetization**

We can also do the scalar product with z direction to get maps of longitudinal component at surface.

When dealing with square wires, rays launched from wire axis are not normal to surface. Method is then slightly different (see Figure 6.3a). Rays are still radially launched from wire axis and intersection with the surface of nanostructure determined. This step enables to find equispaced magnetization vectors at surface. However, $\hat{\mathbf{k}}$ vector is not equivalent to the outward normal to surface. Thus instead of computing the scalar product ($\hat{\mathbf{k}} \cdot \mathbf{m}$) we compute ($\mathbf{n}_{\text{s}} \cdot \mathbf{m}$) where $\mathbf{n}_{\text{s}}$ is the outward normal of surface, which is defined for each surface element. With this configuration, there is a sharp change of normal to surface direction at edges of the square

thus a sharp change of color on maps (Figure 6.3a). This change highlights circulation of magnetization, which is an orthoradial curling since the color changes from red to blue (or vice-versa) at locations where the local magnetization is tangent to the surface. This curling is accompanied with magnetic charges at wire edges. The first method does not highlight edge charges. However the latter has the advantage to keep a continuous normal to surface convention and thus to highlight curling around transverse part (Figure 6.3b).

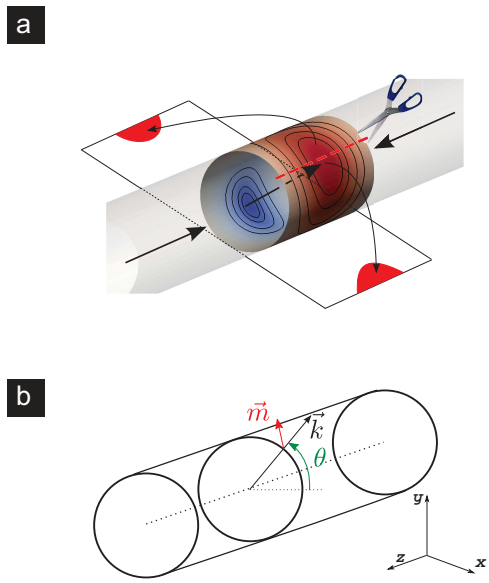

FIGURE 6.2: **Surface map technique.** (a) Black arrows are for magnetization. (b) Principle of the technique.

B - 3 Computation of a discrete vector field curl

Curl of magnetization has been chosen as an order parameter to follow the breaking of symmetry occurring in TW. We were first interested in curl integrated over the wire and its plot as a function of diameter. Following evolution of each curl component, it will be possible to decide wether the rise of curling we observe on micromagnetic configurations is a second-order phase transition. It is also possible to gather information from the layer-resolved curl of magnetization, along wire length, for example, to compare the curl of magnetization of a TVW along wire axis to the one of a BPW.

Both methods need a normalization. For the layer-resolved method, normalization has be chosen so that curl equals π for a perfect orthoradial curling, like the one of a BPW. To achieve this, the value integrated over a disk cross section was divided by d, the diameter. In the curl integrated over the volume, normalization has been chosen so that the curl equals π for a DW of length d. Final result is divided by d^2. Thus both curling strength and volume enter the result. A value larger than π can be obtained, for example, in case of a BPW with width much larger than d (Figure 2.7)b.

Calculation of the curl is another example of use of ray method, making this method mesh independent. However this independence is limited since, as shown previously (sec.1.3.3) the derivative of magnetization is constant within a cell.

Obviously there are other methods to implement the curl of magnetization in case of finite element structured systems. It would be possible to compute the curl of magnetization for each element of mesh and add them. However this method depends more on mesh and does not allow to easily get a z-resolved curve of the curl. Indeed, without making use of the ray, method would have use a loop over all cells to find all those being at a given position. But this method may lead to a lot of mistakes such as double counts.

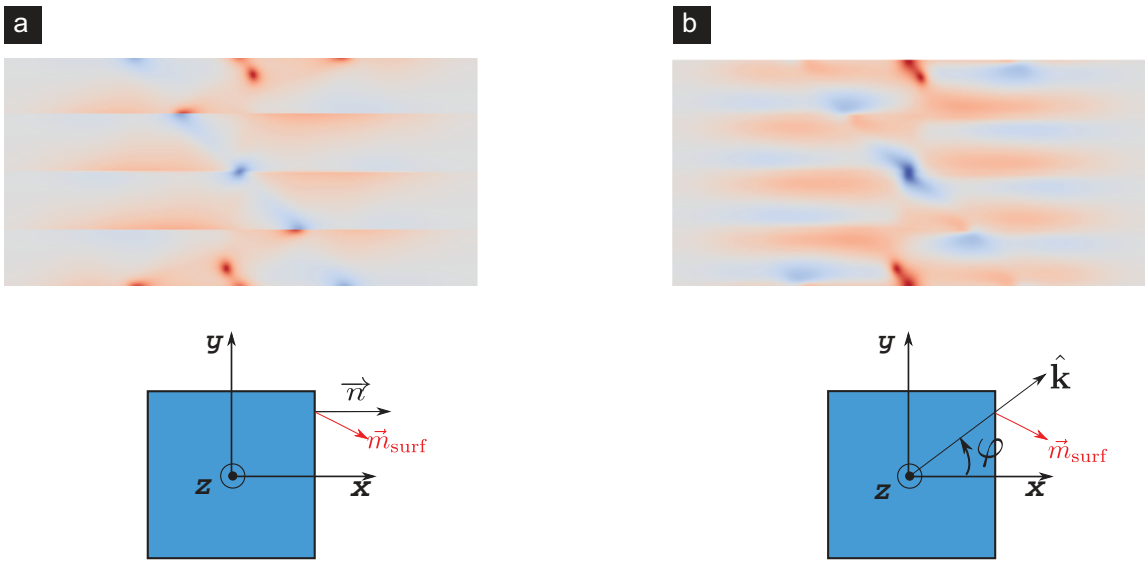

FIGURE 6.3: **Two methods for surface magnetization**. Top row: Maps of surface magnetization for a TW in a 120 nm-side square-based nanowire. Bottom row: Schemes of methods. (a) Surface magnetization computed using scalar product between normal to surface $\mathbf{n}$ and magnetization $\mathbf{m}$. (b) Surface magnetization using the scalar product between ray launched from wire axis $\hat{\mathbf{k}}$ and magnetization $\mathbf{m}$.

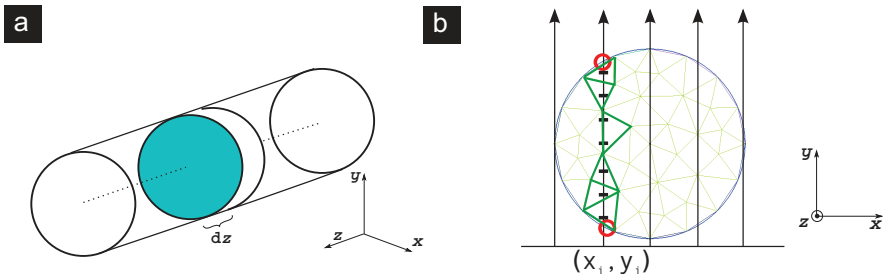

FIGURE 6.4: **Computed curl technique.** (a) Wire with an infinitesimal cylinder. (b) Disk on which the curl is computed. Large black arrows stand for rays, green triangles schematize tetrahedrons crossed by ray and black marks are discretization place.

Let us start to detail the layer-resolved method. Let assume wire axis is along the z direction. The curl is thus computed for layers in the (x, y) plane. Wire length is discretized into small segments i of length dz. For each z_i position, a ray is launched in the y direction, from a point under the wire, with coordinates (x_j, y, z_i). The x_j-coordinate of the ray spans the diameter size (see Figure 6.4b). For each ray, the entering and exit points and the intercepted tetrahedrons are determined as in the section B - 1. Magnetization is then interpolated at one point inside a tetrahedron. Only one point is necessary due to P1-type polynomials that have a constant gradient within a cell. The derivatives of the magnetization are obtained using the derivatives of the Lagrange polynomials and magnetization at nodes. Because we are using P1-type polynomials, we can directly compute spatial derivatives of magnetization by derivating the Lagrange polynomials. Finally, curl is computed and integrated along the ray path (see Figure 6.4a). At the end we get magnetization curl for a layer of a given thickness. This method is repeated along the wire axis so as to get a z-resolved curl of the three components of magnetization as presented in Figure 2.7a. An algorithm of principle of this code is presented hereafter:

```
Find direction of transverse component A using the mean value of
    the transverse component
Build a base with (A, B, z)
  Loop over the z direction with dz step
      Increase z by dz
      Loop over the x position
         Definition of origin of the ray (x, y, z) and direction
             (1, 0, 0)
         Find the entering and exit points of the ray,
             discretization
            Interpolation of the magnetization at the interior
                points
            Computing of magnetization curl at one Gauss point (
                derivatives are constant within a cell) then
                multiplication by dx and addition to the previous
                term
         Multiplication of this term by dy and addition
      end loop
  end loop
Projection of the three components of the curl on (A, B, z) base
Saving of components, divided by the diameter
```

Listing 6.7: **Algorithm for the z-resolved curl of the magnetization**

For the second method, the first steps are the same as previously. Curl is computed on a disk as before but then it is integrated over wire volume, adding all layer values. Algorithm of principle is:

```
Build a base with (A, B, z)
  Loop over z direction with dz step
      Loop over x direction
        Definition of origin of ray (x, y, z) and direction (1, 0,
            0)
        Find entering and exit points of ray, discretization
        Computing of the curl of magnetization at one interior point
             (derivatives are constant within a cell), multiplication
             by dy + addition
      end loop
      Multiplication of this curl by dz + addition
      Projection of the three components of the curl to the (A, B,
          z) base
      Saving of components, divided by the squared diameter
  end loop
```

Listing 6.8: **Algorithm of principle for the wire integrated curl of the magnetization**

B - 4 Estimation of the domain wall width

There are various definitions for domain wall width (Lilley [22], Thiele [23], Jakubovics [69] and others, see sec.2.5). The point is to get a scaling law and not numerical coefficients in most cases. Exact definition of domain wall width is not important. Thus we decide to use $\delta_{\mathrm{DW}} = \int_{-\infty}^{+\infty} \sin\theta(x)\mathrm{d}x$ which is a variation of the definition of Jakubovics: $\delta_{\mathrm{J}} = \int_{-\infty}^{+\infty} \sin^2\theta(x)\mathrm{d}x$.

To compute this integral a procedure based on the one used to compute the curl for a layer was used. Three components of magnetization are averaged over a layer of wire, so that a direction of magnetization is associated with a thin cylinder of thickness dz. With these data it is possible to get the angle between wire axis and the magnetization. Then the sine of this angle is integrated along wire. Sine is zero within domains and non-zero inside wall contributing to wall width. Algorithm for the method is:

```
Initialize integral=0.0
Loop over z
  x = xmin
  Loop over y (ny step)
    y=ymin + dy*ny
    Ray launched in the x-direction from P_ori (x, y, z)
    Find intersection
    Interpolation of magnetization
    Add magnetization vectors component by component
  end loop
end loop
Loop over all z-layers
  Get angle theta between z direction and averaged magnetization
  Integral += abs(sin(theta))
end loop
```

Listing 6.9: **Algorithm of principle for domain wall width**

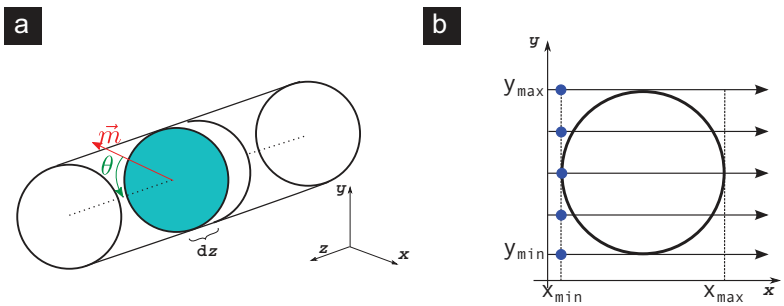

Figure 6.5: **Computed domain wall width** (a) An averaged magnetization direction is associated with a cylinder of infinitesimal thickness. (b) Ray launching within a layer. Blue dots are places from where rays are launched.

B - 5 Analytical test cases for XMCD

Simulation code used to simulate shadow XMCD-PEEM (chap.3) has been validated using an analytical model. For this validation, we used the software Matlab [102]. Two magnetic configurations were tested. First, the magnetization is aligned with beam (Figure 3.7b), second, it is a pure orthoradial curling (Figure 3.7c). Uniform magnetization is the simplest configuration to test, with absorption along path of X-ray. A wire uniformly magnetized along its axis can be also used but it is not relevant. Indeed, magnetization is everywhere perpendicular to beam and thus there is no absorption. Pure orthoradial curling is of interest since it is close to the BPW configuration. To compare analytical and numerical results, we first compute photon intensity for each polarization, then XMCD-PEEM contrast.

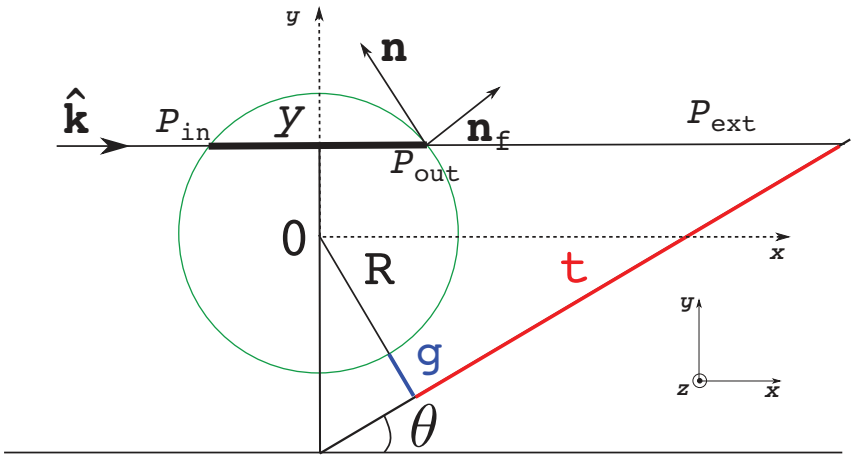

FIGURE 6.6: **Scheme for analytical models used for shadow XMCD-PEEM.** $\hat{\mathbf{k}}$ is the beam direction, P_{in} and P_{out} are entering and exit points of ray into wire, P_{ext} is the intersection between beam and substrate. g is the gap between wire and substrate, $\mathbf{n}_{\text{f}}$ is the local outward normal to wire surface and $\mathbf{n}$ is the normal to substrate. θ is the angle between beam direction and substrate.

Let us have a look at Figure 6.6 to follow discussion. Intensity of remaining photons is computed in the interval $y \in [-R\,;R]$.

Intensity

Magnetization parallel to the beam

One assumes that magnetization is perpendicular to wire and aligned with the beam. Due to absorption, X-ray intensity decreases exponentially along path (Figure 3.7b). More precisely, one has:

$$\text{arg}_0 = \frac{\mu_{\sigma^+} + \mu_{\sigma^-}}{2} \times x_{\text{f}} \tag{6.9a}$$

$$\text{arg}_{1,\text{para}} = \frac{\mu_{\sigma^+} - \mu_{\sigma^-}}{2} \times x_{\text{f}} \tag{6.9b}$$

$$I_{X,\sigma^+}(x_{\text{f}}) = \exp(-\text{arg}_0 - \text{arg}_{1,\text{uni}}) \tag{6.9c}$$

$$I_{X,\sigma^-}(x_{\text{f}}) = \exp(-\text{arg}_0 + \text{arg}_{1,\text{uni}}) \tag{6.9d}$$

arg_0 is the non-magnetic part on absorption, whereas $\text{arg}_{1,\text{uni}}$ is magnetic absorption depending on configuration.

Abscissa t where photon intercepts substrate is $t = y/\sin(\theta) + (R + gap)/\tan(\theta)$ (Figure 6.6). Then we define a test variable h such that:

$$\begin{aligned} h &= 0 \quad \text{if} \quad t < R \\ h &= 1 \quad \text{if} \quad t > R \end{aligned} \tag{6.10}$$

The variable h is used as a test for all photons intercepting substrate. If intersection abscissa is smaller than wire radius then intensity of considered photon is not taken into account. This test removes intensity arising from the bottom part of the wire. Thus this part gives electron contrast in shadow.

```
for n=1:Ny // y−loop from −R to +R
   arg0=(kp+km)*xf(n);
   arg1=(kp-km)*xf(n);
   Ip(n)=exp(-arg0+arg1);
   Im(n)=exp(-arg0-arg1);
end;

ti=16*pi/180.; //angle between beam and substrate
t=y/sin(ti)+(R+gap)/tan(ti); //definition of the distance from wire bottom and
    intersection of ray with substrate
h=1-(t<R); //test
```

Listing 6.10: **Matlab code for photon intensity on shadow for a magnetization parallel to beam**

Next part computes intensity at wire surface. At entering point x_{i}, intensity is set to one because no absorption has taken place yet. At exit point of wire, intensity is given by equation (6.9a):

```
for n=1:Ny
   arg0=(kp+km)*xf(n);
   arg1=(kp-km)*xf(n);
   Iph_p=exp(-arg0-arg1);
   Iph_m=exp(-arg0+arg1);

   p=p+1;
   x=-xf(n); // entering point
   nf=[-xf(n), y(n)]/R;
   nfng=dot(nf, ng);
   nfk=nf(1); // x− direction, parallel to photon direction
   if (nfng>0)
      Ip(p)=1; Im(p)=1;
   end;

   p=p+1; x=+xf(n); // exit point
   nf=[+xf(n), y(n)]/R;
   nfng=dot(nf, ng); nfk=nf(1);
   if (nfng>0)
      Ip(p)=Iph_p; Im(p)=Iph_m;
   end;
end;
```

Listing 6.11: **Matlab code for the photon intensity at wire surface for a magnetization parallel to beam**

Orthoradial curling

For the orthoradial curling, the method is exactly the same as for the uniform magnetization. Only the argument arg_1 related to the magnetic absorption of the exponential differs. They become:

$$\arg_0 = \frac{\mu_{\sigma^+} + \mu_{\sigma^-}}{2} \times x_\mathrm{f} \tag{6.11a}$$
$$\arg_{1,\mathrm{curl}} = \frac{\mu_{\sigma^+} - \mu_{\sigma^-}}{2} \times |y| \times \mathrm{asinh}(x_\mathrm{f}/y) \tag{6.11b}$$
$$I_{X,\sigma^+}(x_\mathrm{f}) = \exp(-\arg_0 - \arg_{1,\mathrm{curl}}) \tag{6.11c}$$
$$I_{X,\sigma^-}(x_\mathrm{f}) = \exp(-\arg_0 + \arg_{1,\mathrm{curl}}) \tag{6.11d}$$

XMCD-PEEM contrast

We can now turn to XMCD-PEEM contrast. The algorithm is quite the same. First we compute contrast at each point on shadow by removing points at the bottom surface of wire using test variable h (see eq.6.10). We add then contrast arising from points at wire surface.

Magnetization parallel to beam

Dichroic contrast on substrate, is given by:

$$C(p) = \frac{I_{e,\sigma^-}(p) - I_{e,\sigma^+}(p)}{I_{e,\sigma^-}(p) + I_{e,\sigma^+}(p)} \tag{6.12a}$$

Matlab code for shadow contrast on substrate is:

```
for n=1:Ny // y-loop from -R to +R
   arg0=(kp+km)*xf(n);
   arg1=(kp-km)*xf(n);
   Ip(n)=exp(-arg0+arg1);
   Im(n)=exp(-arg0-arg1);
   C(n)=(Im(n)-Ip(n))/(Im(n)+Ip(n)); //Contrast
end;

ti=16*pi/180.; //angle between the beam and the substrate
t=y/sin(ti)+(R+gap)/tan(ti); //definition of the distance from the wire bottom
    and intersection of ray with substrate
h=1-(t<R); //test
```

Listing 6.12: **Matlab code for XMCD contrast on shadow for magnetization parallel to beam**

Contrast at surface of wire is split into two parts. We compute separately entering points, where no absorption has yet taken place through matter, and exit points, with absorption through matter. First, let us define some variables used in the following:

$$\mathrm{f}_{\mathrm{para},\sigma^+} = \frac{2}{\mu_{\sigma^+} + \mu_{\sigma^-}}[(\mu_{\sigma^+} + \mu_{\sigma^-})/2 + (\mu_{\sigma^+} - \mu_{\sigma^-})/2] \tag{6.13a}$$
$$= 1 + \frac{\mu_{\sigma^+} + \mu_{\sigma^-}}{\mu_{\sigma^+} - \mu_{\sigma^-}} \tag{6.13b}$$
$$\mathrm{f}_{\mathrm{para},\sigma^-} = \frac{2}{\mu_{\sigma^+} + \mu_{\sigma^-}}[(\mu_{\sigma^+} + \mu_{\sigma^-})/2 - (\mu_{\sigma^+} - \mu_{\sigma^-})/2] \tag{6.13c}$$
$$= 1 - \frac{\mu_{\sigma^+} + \mu_{\sigma^-}}{\mu_{\sigma^+} - \mu_{\sigma^-}} \tag{6.13d}$$
$$n_f = [-xf(n), y(n)]/R \tag{6.13e}$$
$$asc = |n_f \cdot k| \tag{6.13f}$$

asc is related to the angle cosine between the outward normal to surface and direction of extracted electrons. This quantity is linked to the number of events (absorption) occurring in the wire volume. $n_f \cdot k$ is the local normal component in the direction of beam. It is possible to add 10^{-16} to asc for cases the two vectors are orthogonal.

The dichroic contrast for entering points only includes the dichroism at the surface of the material. It is given by:

$$I_{e,\sigma^+}(p) = \mathrm{f}_{\mathrm{para},\sigma^+}/asc \tag{6.14a}$$
$$I_{e,\sigma^-}(p) = \mathrm{f}_{\mathrm{para},\sigma^-}/asc \tag{6.14b}$$
$$\tag{6.14c}$$

Contrast for exit points takes into account absorption through matter, combined with dichroism:

$$I_{e,\sigma^+}(p) = \mathrm{f}_{\mathrm{para},\sigma^+} \times I_{X,\sigma^+}/asc \tag{6.15a}$$
$$I_{e,\sigma^-}(p) = \mathrm{f}_{\mathrm{para},\sigma^-} \times I_{X,\sigma^-}/asc \tag{6.15b}$$
$$\tag{6.15c}$$

In both magnetic cases, contrast is given by:

$$C(p) = \frac{I_{e,\sigma^-}(p) - I_{e,\sigma^+}(p)}{I_{e,\sigma^+}(p) + I_{e,\sigma^+}(p)} \tag{6.16}$$

Code for both two cases, entering and exit points, is:

```
p=0;
tg=[+cos(ti) sin(ti)]; // beam direction
ng=[-sin(ti) cos(ti)]; // orthogonal direction to beam
for n=1:Ny // loop over y values from −R to +R
   arg0=(kp+km)*xf(n);
   arg1=(kp-km)*xf(n);
   Iph_p=exp(-arg0-arg1); //photon intensity for positive polarization
   Iph_m=exp(-arg0+arg1); // photon intensity for negative polarization

   pf_sigmap=(kp+km)/2+(kp-km)/2; //definition of pre−factor for positive
       polarization
   pf_sigmam=(kp+km)/2-(kp-km)/2; // pre−factor for negative polarization

   p=p+1;
   x=-xf(n); //set x to entering point
   nf=[-xf(n), y(n)]/R; // normal to surface at entering point
   nfng=dot(nf, ng);
   nfk=nf(1);
   if (nfng>0) // test to keep photo−electrons escaping towards detector
  asc=abs(nfk);
       Ip(p)=pf_sigmap/asc; // photo−electron intensity for positive polarization
       Im(p)=pf_sigmam/asc; // photo−electron intensity for negative polarization
       C(p)=(Im(p)-Ip(p))/(Im(p)+Ip(p)); //contrast
   end;

   p=p+1;
   x=+xf(n); //set x to exit point
   nf=[+xf(n), y(n)]/R; //normal to surface at exit point
```

```
    nfng=dot(nf, ng);
    nfk=nf(1); // x−component of nf along beam direction = dot(nf, tg)
    if (nfng>0) // test to keep photo−electrons escaping towards detector
        asc=abs(nfk);
        Ip(p)=pf_sigmap*Iph_p/asc; //photo−electron intensity for positive polarization
        Im(p)=pf_sigmam*Iph_m/asc; // photo−electron intensity for negative polarization
        C(p)=(Im(p)-Ip(p))/(Im(p)+Ip(p)); //contrast
    end;
end;
```

Listing 6.13: **Matlab code for XMCD contrast on wire surface for a magnetization parallel to beam**

If ray is perpendicular to the normal then the scalar product asc tends to zero. If we note t the photon path of wave vector $\hat{\mathbf{k}}$ through matter, t_e the escape depth of photo-electrons and $\mathbf{n}$ the local outward normal to wire surface then:

$$I = \int_0^t e^{-\mu x}\mathrm{d}x = \frac{1-e^{-\mu t}}{\mu} \tag{6.17}$$

$$\sim t = \frac{t_\mathrm{e}}{\hat{\mathbf{k}}.\mathbf{n}} \text{ if } t \ll \frac{1}{\mu} \tag{6.18}$$

$$\sim \frac{1}{\mu} \text{ if } t \gg \frac{1}{\mu} \tag{6.19}$$

Thus intensity does not diverge for rays almost tangent to wire surface.

Orthoradial curling

For orthoradial curling, principle is similar as for magnetization parallel to beam. Only pre-factors differ.

$$u = -y/R \tag{6.20a}$$

$$\mathrm{f}_{\mathrm{curl},\sigma^+} = \frac{2}{\mu_{\sigma^+}+\mu_{\sigma^-}}[(\mu_{\sigma^+}+\mu_{\sigma^-})/2+(\mu_{\sigma^+}-\mu_{\sigma^-})/2]\times u \tag{6.20b}$$

$$= 1+\frac{\mu_{\sigma^+}+\mu_{\sigma^-}}{\mu_{\sigma^+}-\mu_{\sigma^-}}\times u \tag{6.20c}$$

$$\mathrm{f}_{\mathrm{curl},\sigma^-} = \frac{2}{\mu_{\sigma^+}+\mu_{\sigma^-}}[(\mu_{\sigma^+}+\mu_{\sigma^-})/2-(\mu_{\sigma^+}-\mu_{\sigma^-})/2]\times u \tag{6.20d}$$

$$= 1-\frac{\mu_{\sigma^+}+\mu_{\sigma^-}}{\mu_{\sigma^+}-\mu_{\sigma^-}}\times u \tag{6.20e}$$

$$\tag{6.20f}$$

Other terms are identical. Thus the code used for implementation differs only by adding the term $u = y/R$ with $y = y(n)$ varying in loop.

C Simulation of the MFM contrast

Magnetic force microscopy (MFM) is the most accessible imaging technique at laboratory. Thus it is the first to be used to try to locate then identify the type of DW. This technique can also be used to study propagating fields by imaging before and after a field is applied. Question arises, whether it may be used to identify the type of DW in cylindrical wires, either TVW or BPW.

C - 1 Phase contrast in MFM imaging

Cantilever oscillates as an harmonic oscillator in z-direction around its equilibrium position z_0. We work under the assumption of small amplitude oscillations. Taking this force into account, the dynamics of the cantilever along the z-direction is given by:

$$m\ddot{z}(t) + \Gamma\dot{z} + c[z(t) - z_0] = F_z^{\text{ext}}(t) \tag{6.21}$$

where m is magnetic tip mass, Γ is surrounding media viscosity and c the cantilever stiffness. Since we made the assumption of small oscillations, it is possible to write the Taylor expansion of the force around the tip equilibrium position z_0:

$$F_z \cong F_z(z_0) = (z - z_0) \left.\frac{\partial F_z}{\partial z}\right|_{z_0} + \vartheta(z - z_0)^2 \tag{6.22}$$

The second derivative of the position along the z direction is then given by:

$$m\ddot{z} \cong -c\left(1 - \frac{1}{c}\left.\frac{\partial F_z}{\partial z}\right|_{z_0}\right)(z - z_0) + F_z^{\text{ext}} + F_z(z_0) \tag{6.23}$$

Without any external force, the pulsation the of cantilever is $\sqrt{m/c}$ and the frequency is $f_0 = \frac{1}{2\pi}\sqrt{c/m}$. With the perturbation from the external force, the oscillation frequency is:

$$f = \frac{1}{2\pi}\sqrt{\frac{c}{m}\left(1 - \frac{1}{c}\left.\frac{\partial F_z}{\partial z}\right|_{z_0}\right)} = f_0\sqrt{1 - \frac{1}{c}\left.\frac{\partial F_z}{\partial z}\right|_{z_0}} \tag{6.24}$$

C - 2 MFM models

Force between sample and tip comes from Zeeman force resulting of magnetization tip stray field, or equivalently of sample stray field on tip magnetization. Since tip magnetic moment is supposed to be known and fixed whereas we are looking for sample stray field, we chose the latter Zeeman force.

It is possible to use either monopolar or dipolar approach. With the monopolar one, magnetic force is integrated from tip equilibrium position to infinity whereas for the dipolar one, force is integrated over the tip. Let us present the monopolar approach:

$$E_{\text{int}} = \mu_0 \int_z^{+\infty} \mathrm{d}^3\mathbf{r}'\ \mathbf{M}_{\text{tip}}(\mathbf{r}') \cdot \mathbf{H}(\mathbf{r}') \tag{6.25}$$

where $\mathbf{H}$ is the stray field from sample.

The force resulting from energy is given by $F_z = -\partial_z E_{\text{int}}$. Thus, for the monopolar approach, force along z-direction is given by:

$$F_z = -\mu_0 S M_{\text{tip}}^z H_z(z_0) \tag{6.26}$$

where S is the interaction surface. And relative variation of the oscillating frequency of the tip is:

$$\frac{\Delta f}{f_0} \cong \frac{1}{2c}\left.\frac{\partial F_z}{\partial z}\right|_{z_0} = -\mu_0 M_{\text{tip}}^z S \frac{1}{2c}\left.\frac{\partial H_z}{\partial z}\right|_{z_0} \tag{6.27}$$

In the framework of the dipolar approach, interaction energy is given by:

$$E_{\text{int}} = \mu_0 \int_z^{z+L} \mathrm{d}^3\mathbf{r}'\ \mathbf{M}_{\text{tip}}(\mathbf{r}') \cdot \mathbf{H}(\mathbf{r}') \tag{6.28}$$

Force is then:

$$F_z = \mu_0 S M^z_{\text{tip}}[H_z(z) - H_z(z-L)] = \mu_0 S M^z_{\text{tip}} L \frac{\partial H_z}{\partial z} \tag{6.29}$$

Finally, the relative variation of the oscillation frequency of the tip is:

$$\frac{\Delta f}{f_0} \cong -\mu_0 M^z_{\text{tip}} S L \frac{1}{2c} \left. \frac{\partial^2 H_z}{\partial z^2} \right|_{z_0} \tag{6.30}$$

Field acts decreasing or increasing frequency for attractive or repulsive interaction.

C - 3 Simulations and results

The developed MFM code is a post-processing of the finite element code FeeLLGood. This means micromagnetic configurations we use for simulations of MFM contrast are obtained with relaxation of magnetization (see sec.1.3.3). Material parameters are those of permalloy. MFM contrast is computed along a path standing for tip trajectory over sample to reflect the so-called lift mode MFM. This surface will be discretized into finite elements. It is of importance to think about the shape of this surface and thus to the trajectory of the tip. In the end, the surface is close to a half cylinder prolongated with flat sides (Figure 6.7a). Sides are enlarged so as to take into account the place needed by the tip.

Simulation results are presented in Figure 6.7. We confirm rotation invariance around the wire axis for a BPW (Figure 6.7c). Influence of the orientation of a TVW around wire axis is illustrated by Figure 6.7d-f. Simulated contrasts are symmetric, contrary to the experimental ones (Figure 6.8c). This observed asymmetry may originate from three different phenomena. First, trajectory of the tip over the sample is asymmetric (dotted line in Figure 6.8b). Second, tip oscillations are not vertical (black arrow in Figure 6.8c). Thus not only $\partial_z H_z$ is taken into account but also $\partial_x H_z$. Third, magnetization of the tip is not perpendicular to sample. Thus some derivatives of H_x, coming from the stray field from the sample, may also be included. It is not clear which of the three origins is the most important.

Lateral resolution of MFM is typically 30 nm, but can reach 20 to 10 nm. However, when looking at simulated MFM images, we see contrast variations occurring within a very small distance, typically of the order of 10 nm. These variations are thus not observable experimentally making it very difficult to discriminate between a transverse and a Bloch point wall.

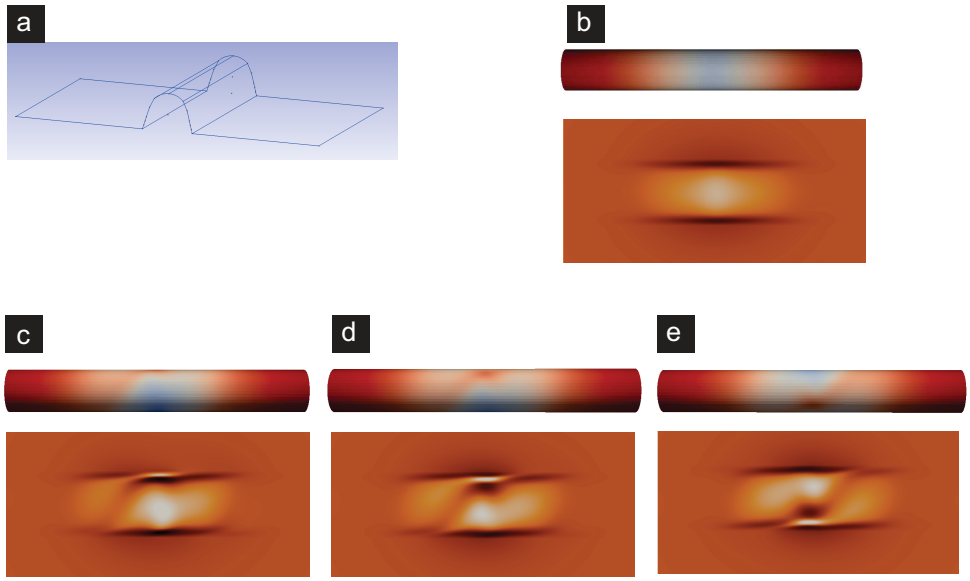

FIGURE 6.7: **Simulated MFM contrast** (a) Surface. (d) to (e) Top: surface magnetic potential, bottom: simulated MFM contrast. (b) BPW, d=70 nm, (c) to (e) TVW, d=70 nm. (d) 45 °-rotation around the wire axis from (d). (e) 135 ° rotation from (d).

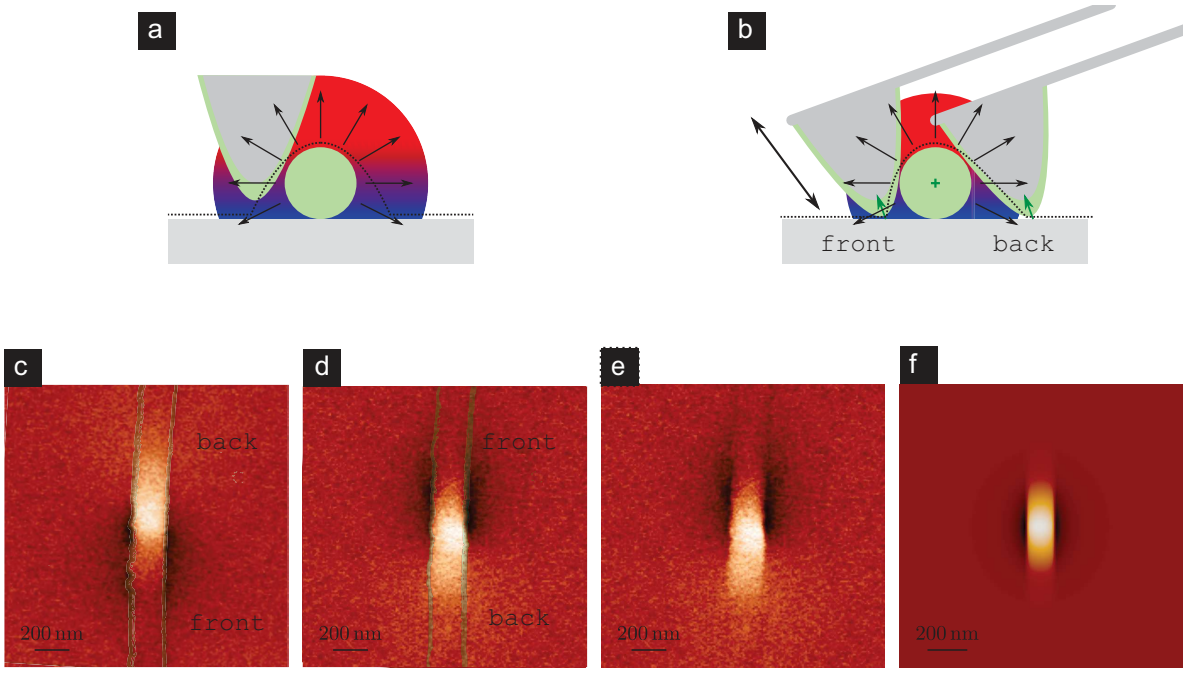

FIGURE 6.8: **Illustration of the experimental artifact on MFM images.** (a) If the tip were moving vertically, there would be no asymmetry on the image. (b) Tip oscillating at the end of a cantilever thus not vertically, which induces an asymmetry between the front and back sides of the wire. (c-e) $d = 80$ nm. (e) is made out of (c)+(d) to remove the front/back artifact. (f) Comparison with simulated contrast for a BPW, $d = 70$ nm. From [11]

Glossary

Abbreviations

ATW	Asymmetric transverse wall
BPW	Bloch point wall
LLG	Landau Lifshitz Gilbert (equation)
MFM	Magnetic Force Microscopy
PEEM	PhotoElectron Emission Microscopy
SPLEEM	Spin Polarized Low Electron Emission Microscopy
TVW	Transverse/Vortex wall
TW	Transverse wall
VW	Vortex wall
XAS	X-ray Absorption Spectroscopy
XMCD	X-ray Magnetic Circular Dichroism

Symbols

A	J/m	exchange constant
α	-	damping parameter
β	-	non-adiabatic constant
E_{ex}	J/m^3	exchange energy volume density
E_{a}	J/m^3	anisotropy energy volume density
E_{mc}	J/m^3	magnetocrystalline energy volume density
E_{Z}	J/m^3	Zeeman energy volume density
$\mathcal{E}_{\mathrm{ex}}$	J	exchange energy
$\mathcal{E}_{\mathrm{d}}$	J	magnetostatic energy
$\mathcal{E}_{\mathrm{SD}}$	J	single domain energy
$\mathcal{E}_{\mathrm{V}}$	J	vortex state energy
$\hat{\mathbf{k}}$	m$^-$1	wave vector
l_{SD}	m	single domain critical size
$\boldsymbol{\ell}$	kg.m^2.s$^-$1	angular momentum
K_{u}	J/m^3	anisotropy constant
$\boldsymbol{\mu}$	A.m^2	magnetic momentum
$\mathbf{M}$	A/m	magnetization vector

M_s	A/m	spontaneous magnetization
m_ℓ		magnetic quantum number
ϕ_d	A	magnetic potential
g	-	Landé factor
H_d	A/m	dipolar field
H_W	A/m	Walker field
H_ext	A/m	external field
H_K	A/m	dipolar field
Δ_d	m	dipolar exchange length
Δ_u	m	anisotropy exchange length
W	m	domain wall width
W_J	m	Jakubovics domain wall width
$W_\mathrm{L,uni}$	m	Lilley uniaxial domain wall width
W_T	m	Thiele domain wall width

Bibliography

[1] S. S. P. Parkin. U.s. patents 6834005, 6898132, 6920062.

[2] A. Thiaville and Y. Nakatani. *Spin dynamics in confined magnetic structures III*, chapter Domain-wall dynamics in nanowires and nanostrips, pages 161–206. Topics Appl. Physics. Springer, Berlin, 2006.

[3] Y. Nakatani, A. Thiaville, and J. Miltat. Head-to-head domain walls in soft nano-strips: a refined phase diagram. *J. Magn. Magn. Mater.* , 290-291:750, 2005.

[4] J. Kimling, F. Kronast, S. Martens, T. Böhnert, M. Martens, J. Herrero-Albillos, L. Tati-Bismaths, U. Merkt, K. Nielsch, and G. Meier. Photoemission electron microscopy of three-dimensional magnetization configurations in core-shell nanostructures. *Phys. Rev. B* , 84:174406, 2011.

[5] R. Streubel, V. P. Kravchuk, D. D. Sheka, D. Makarov, F. Kronast, O. G. Schmidt, and Y. Gaididei. Equilibrium magnetic states in individual hemispherical permalloy caps. *Appl. Phys. Lett.* , 101(13):132419, 2012.

[6] O. Sandig, J. Herrero-Albillos, F.M. Römer, N. Friedenberger, J. Kurde, T. Noll, M. Farle, and F. Kronast. Imaging magnetic responses of nanomagnets by xpeem. *J. Electron Spectr. Rel. Phenom.* , 185(10):365–370, 2012.

[7] J. Zabaleta, S. Valencia, F. Kronast, C. Moreno, P. Abellan, J. Gazquez, H. Sepehri-Amin, F. Sandiumenge, T. Puig, N. Mestres, and X. Obradors. Photoemission electron microscopy study of sub-200 nm self-assembled $La_{0.7}Sr_{0.3}MnO_3$ epitaxial islands. *Nanoscale* , 5(7):2990, 2013.

[8] S. Da Col, S. Jamet, N. Rougemaille, A. Locatelli, T. O. Mentes, B. Santos Burgos, R. Afid, M. Darques, L. Cagnon, J. C. Toussaint, and O. Fruchart. Observation of Bloch-point domain walls in cylindrical magnetic nanowires. *Phys. Rev. B* , 89:180405, 2014.

[9] Robert Streubel, Jehyun Lee, Denys Makarov, Mi-Young Im, Daniil Karnaushenko, Luyang Han, Rudolf Schäfer, Peter Fischer, Sang-Koog Kim, and Oliver G. Schmidt. Magnetic microstructure of rolled-up single-layer ferromagnetic nanomembranes. *Adv. Mater.* , 26:316, 2014.

[10] P. Fischer D. Parkinson O. G. Schmidt D. Makarov R. Streubel, F. Kronast. Retrieving spin textures on curved magnetic thin films with full-field soft x-ray microscopies. *Nat. Com.*, 6, 2015.

[11] S. Da Col. *Parois magnétiques dans les nanofils cylindriques.* PhD thesis, Université de Grenoble, 2014.

[12] W. F. Brown, Jr. Micromagnetics: domain walls. *J. Appl. Phys.* , 30(4):62S, 1959.

[13] W. F. Brown Jr. *Magnetostatic principles in Ferromagnetism.* North-Holland, Amsterdam, 1962.

[14] A. Hubert and R. Schäfer. *Magnetic domains. The analysis of magnetic microstructures.* Springer, Berlin, 1999.

[15] P. O. Jubert and R. Allenspach. Analytical approach to the single-domain-to-vortex transition in small magnetic disks. *Phys. Rev. B* , 70:144402/1–5, 2004.

[16] E. C. Stoner and E. P. Wohlfarth. A mechanism of magnetic hysteresis in heterogeneous alloys. *Phil. Trans. Roy. Soc. Lond. A* , 240:599–642, 1948.

[17] E. C. Stoner and E. P. Wohlfarth. reprint of 1948 'a mechanism of magnetic hysteresis in heterogeneous alloys'. *IEEE Trans. Magn.* , 27(4):3469–3518, 1991.

[18] E. H. Frei, S. Shtrikman, and D. Treves. Critical size and nucleation field of ideal ferromagnetic particles. *Phys. Rev.* , 106:446, 1957.

[19] L. Landau and E. M. Lifschitz. On the theory of the dispertion of magnetic permeability in ferromagnetic bodies. *Phys. Z. Sowjetunion* , 8:153–159, 1935.

[20] T. L. Gilbert. A phenomenological theory of damping in ferromagnetic materials. *Phys. Rev.*, 10:1243, 1955.

[21] F. Bloch. *Z. Phys.* , 74:295, 1932.

[22] B. A. Lilley. Energies and widths of domain boundaries in ferromagnetics. *Philos. Mag.* , 41(7):401–406, 1950.

[23] A. A. Thiele. Steady-state motion of magnetic domains. *Phys. Rev. Lett.* , 30:230–233, 1973.

[24] A. P. Malozemoff and J. C. Slonczewski. *Magnetic domain walls in bubble materials.* Academic press, 1979.

[25] N. L. Schryer and L. R. Walker. The motion of 180 domain walls in uniform dc magnetic fields. *J. Appl. Phys.* , 45(12):5406–5421, 1974.

[26] J.-Y. Chauleau, R. Weil, A. Thiaville, and J. Miltat. Magnetic domain walls displacement: Automotion versus spin-transfer torque. *Phys. Rev. B* , 82:214414, 2010.

[27] R. McMichael and M. Donahue. Head to head domain wall structures in thin magnetic strips. *IEEE Trans. Magn.* , 33:4167, 1997.

[28] J. C. Slonczewski. Current-driven excitation of magnetic multilayers. *J. Magn. Magn. Mater.* , 159:L1–L7, 1996.

[29] A. Thiaville, Y. Nakatani, J. Miltat, and Y. Suzuki. Micromagnetic understanding of current-driven domain wall motion in patterned nanowires. *Europhys. Lett.* , 69(6):990–996, 2005.

[30] E. Feldkeller and H. Thomas. *Phys. Kondens. Materie* , 8:4, 1965.

[31] W. Döring. Point singularities in micromagnetism. *J. Appl. Phys.* , 39(2):1006, 1968.

[32] H. Forster, T. Schrefl, D. Suess, W. Scholz, V. Tsiantos, R. Dittrich, and J. Fidler. Domain wall motion in nanowires using moving grids. *J. Appl. Phys.* , 91(10):6914, 2002.

[33] R. Hertel. Computational micromagnetism of magnetization processes in nickel nanowires. *J. Magn. Magn. Mater.* , 249:251, 2002.

[34] A. Thiaville, Y. Nakatani, F. Piéchon, J. Miltat, and T. Ono. Transient domain wall displacement under spin-polarized current pulses. *Europhys. J. D* , 60:15–27, 2007.

[35] S. K. Kim and O. Tchernyshyov. Pinning of a Bloch point by an atomic lattice. *Phys. Rev. B* , 88:174402, 2013.

[36] A. Thiaville, J. M. García, R. Dittrich, J. Miltat, and T. Schrefl. Micromagnetic study of Bloch-point-mediated vortex core reversal. *Phys. Rev. B* , 67:094410, 2003.

[37] N. Biziere, C. Gatel, R. Lassalle-Balier, M.-C. Clochard, J. E. Wegrowe, and Et. Snoeck. Imaging the fine structure of a magnetic domain wall in a ni nanocylinder. *Nano Lett.* , 13:2053, 2013.

[38] S. Allende, D. Altbir, and K. Nielsch. Magnetic cylindrical nanowires with single modulated diameter. *Phys. Rev. B* , 80(17):174402, 2009.

[39] D. E. Goldberg. *Genetic Algorithms in Search, Optimization, and Machine Learning.* Addison Wesley, 1989.

[40] http://math.nist.gov/oommf/.

[41] B. Kevorkian. *Contribution à la modélisation du retournement de l'aimantation - Applications à des systèmes magnétiques nanostructurés ou de dimensions réduites.* PhD thesis, Université Joseph Fourier, Grenoble, 1998.

[42] H. Szambolics. *Nouvelles formulations éléments finis pour le micromagnétisme et déplacement de parois par courant polarisé en spin.* PhD thesis, Institut Polytechnique de Grenoble, 2008.

[43] http://llgmicro.home.mindspring.com.

[44] http://nmag.soton.ac.uk/nmag/.

[45] http://vampire.york.ac.uk.

[46] http://mumax.github.io.

[47] D. R. Fredkin and T. R. Koehler. Hybrid method for computing the demagnetizing fields. *IEEE tm*, 26, 1990.

[48] F. Alouges and P. Jaisson. Convergence of a finite elements discretization for the Landau Lifshitz equations. *Math. Mod. Meth. Appl. Sci.*, 16:299–313, 2006.

[49] Christian Andreas, Sebastian Gliga, and Riccardo Hertel. Numerical micromagnetism of strong inhomogeneities. *J. Magn. Magn. Mater.* , 362:7, 2014.

[50] K. Nielsch, R. Hertel, R. B. Wehrspohn, J. Barthel, J. Kirschner, U. Gösele, S. F. Fischer, and H. Kronmüller. Switching behavior of single nanowires inside dense nickel nanowire arrays. *IEEE Trans. Magn.* , 38(5):2571, 2002.

[51] H. Forster, T. Schrefl, W. Scholz, D. Suess, V. Tsiantos, and J. Fidler. Micromagnetic simulation of domain wall motion in magnetic nano-wires. *J. Magn. Magn. Mater.* , 249:181, 2002.

[52] M. Waleczek T. Boehnert D. Goerlitz K. Nielsch P. Sergelius, J.M. Montero Moreno. Magnon contribution to the magnetiresistance of iron nanowires deposited using pulsed electrodeposition. *Phys. Status Solidi RRL*, 1-4, 2015.

[53] R. Wieser, U. Nowak, and K. D. Usadel. Domain wall mobility in nanowires: Transverse versus vortex walls. *Phys. Rev. B* , 69:064401, 2004.

[54] R. Hertel and J. Kirschner. Magnetic drops in a soft-magnetic cylinder. *J. Magn. Magn. Mater.* , 278:L291, 2004.

[55] J. A. Otalora, J. A. Lopez-Lopez, P. Landeros, P. Vargas, and A. S. Nunez. Breaking of chiral symmetry in vortex domain wall propagation in ferromagnetic nanotubes. *J. Magn. Magn. Mater.* , 341:86, 2013.

[56] A. Hubert and W. Rave. Systematic analysis of micromagnetic switching processes. *Phys. Stat. Sol. (b)* , 211(2):S815–829, 1999.

[57] R. Feldkeller. *Z. Angew. Physik* , 19:530, 1965.

[58] M. Kléman. *Points, Lines and Walls.* Wiley, Chichester, 1983.

[59] A. S. Arrott and T. L. Templeton. Micromagnetics and hysteresis as prototypes for complex systems. *Physica B* , 233:259–271, 1997.

[60] R. Hertel and H. Kronmüller. Computation of the magnetic domain structure in bulk permalloy. *Phys. Rev. B* , 60(10):7366–7378, 1999.

[61] F. Cheynis, A. Masseboeuf, O. Fruchart, N. Rougemaille, J. C. Toussaint, R. Belkhou, P. Bayle-Guillemaud, and A. Marty. Controlled switching of Néel caps in flux-closure magnetic dots. *Phys. Rev. Lett.* , 102:107201, 2009.

[62] A. Masseboeuf, O. Fruchart, J. C. Toussaint, E. Kritsikis, L. Buda-Prejbeanu, F. Cheynis, P. Bayle-Guillemaud, and A. Marty. Dimensionality cross-over in magnetism: from domain walls (2d) to vortices (1d). *Phys. Rev. Lett.* , 104:127204, 2010.

[63] S. Middelhoek. Domain walls in thin Ni-Fe films. *J. Appl. Phys.* , 34(4):1054–1059, 1963.

[64] V. D. NǴuyen, O. Fruchart, S. Pizzini, J. Vogel, J. C. Toussaint, and N. Rougemaille. Third type of magnetic domain wall in soft nanostrips. *Scientific Reports*, 5, 2015.

[65] S. Jamet, Rougemaille, J. C. Toussaint, and O. Fruchart. *Magnetic Nano- and Microwires: Design, synthesis, properties and applications.* Woodhead Publishing, 2015.

[66] O. Fruchart, J.-P. Nozières, W. Wernsdorfer, D. Givord, F. Rousseaux, and D. Decanini. Enhanced coercivity in sub-micrometer-sized ultrathin epitaxial dots with in-plane magnetization. *Phys. Rev. Lett.* , 82(6):1305–1308, 1999.

[67] O. Fruchart, J. C. Toussaint, and B. Kevorkian. Micromagnetic model of non-collective magnetization reversal in ultrathin magnetic dots with in-plane uniaxial anisotropy. *Phys. Rev. B* , 63(17):174418, 2001.

[68] M. Chandra Sekhar, H. F. Liew, I. Purnama, W. S. Lew, M. Tran, and G. C. Han. Helical domain walls in constricted cylindrical NiFe nanowires. *Appl. Phys. Lett.* , 101:152406, 2012.

[69] J. P. Jakubovics. Comments on the definition of ferromagnetic domain wall width. *Philos. Mag. B* , 38(4):401–406, 1978.

[70] J. Steiner, H. Wieczoreck, R. Schäfer, J. McCord, and F. Otto. The formation and coarsening of the concertina pattern. 2011.

[71] O. V. Pylypovskyi, D. D. Sheka, and Y. Gaididei. Bloch point structure in a magnetic nanosphere. *Phys. Rev. B* , 85:224401, 2012.

[72] R. Hertel and A. Kakay. Analytic form of transverse head-to-head domain walls in thin cylindrical wires. *Journal of Magnetism and Magnetic Materials*, 379:45–49, 2015.

[73] C. M. Schneider and G. Schönhense. Investigating surface magnetism by means of photoexcitation electron emission microscopy. *Rep. Prog. Phys.* , 65:R1785–R1839, 2002.

[74] P. Fischer, T. Eimüller, G. Schütz, G. Denbeaux, A. Pearson, L. Johnson, D. Attwood, S. Tsunashima, M. Kumazawa, N. Takagi, M. Köhler, and G. Bayreuther. Element-specific imaging of magnetic domains at 25 nm spatial resolution using soft x-ray microscopy. *Rev. Sci. Instr.* , 72(5):2322, 2001.

[75] T. Kasama, R. E. Dunin-Borkowski, and M. Beleggia. *Holography - Different Fields of Application*, review, magnetism, instrumentation Chapter 3: Electron Holography of Magnetic Materials. Intech, 2011.

[76] J. Zweck and T. Uhlig. *Novel techniques for characterizing and preparing samples*, volume 3 of *Handbook of Magnetism and advanced magnetic materials*, experiment, instrumentation, review Lorentz microscopy of thin-film systems, pages 1393–1427. Wiley, 2007.

[77] J. N. Chapman and M. R. Scheinfein. Transmission electron microscopies of magnetic microstructures. *J. Magn. Magn. Mater.* , 200:729–740, 1999.

[78] R. Allenspach. Spin-polarized scanning electron microscopy. *IBM J. Res. Develop.* , 44(4):553, 2000.

[79] N. Rougemaille and A. K. Schmid. Magnetic imaging with spin-polarized low-energy electron microscopy. *Europhys. J.: Appl. Phys.* , 50:20101, 2010.

[80] E. Bauer. Low energy electron microscopy. *Rep. Prog. Phys.* , 57:895–938, 1994.

[81] Stoehr Y. Idzerda R. Nakajima, J. Electron-yield satruation effects in L-edge x-ray magnetic circular dichroism spectra of Fe, Co and Ni. *Phys. Rev. B*, 59:6421, 1999.

[82] J. M. D. Coey. *Magnetism and magnetic materials.* Cambride University Press, 2010.

[83] S. Blundell. *Magnetism in condensed matter.* Oxford University Press, 2001.

[84] A. Locatelli, L. Aballe, T. O. Menteş, M. Kiskinova, and E. Bauer. Photoemission electron microscopy with chemical sensitivity: SPELEEM methods and applications. *Surf. Interf. Analysis* , 38:12–13, 2006.

[85] https://www.elettra.trieste.it/it/lightsources/elettra/elettra-beamlines/nanospectroscopy/useful-info-for-ns-users/page-4.html?showall=.

[86] F. Alouges, E. Kritsikis, and J.-C. Toussaint. A convergent finite element approximation for Landau-Lifschitz-Gilbert equation. *Physica B* , 407:1345, 2012.

[87] R. Nakajima, J. Stöhr, and Y. U. Idzerda. Electron-yield saturation effects in l-edge x-ray magnetic circular dichroism spectra of Fe, Co, and Ni. *Phys. Rev. B* , 59(9):6421, 1999.

[88] Wen-Yaung Lee and Jerome Eldridge. Oxidation studies of permalloy films by quartz crystal microbalance, aes, and xps. *J. Electrochem. Soc.* , 124(11):1747, 1977.

[89] J. B. Kortright, S.-K. Kim, T. Warwick, and N. V. Smith. Soft x-ray circular polarizer using magnetic circular dichroism at the Fe $L3$ line. *Appl. Phys. Lett.*, 71:1446, 1997.

[90] D. P. Pappas, K.-P Kämper, B. P. Miller, and H. Hopster. Spin-dependent electron attenuation by transmission through thin ferromagnetic films. *Phys. Rev. Lett.*, 66:504, 1991.

[91] J. B. Kortright and S. K. Kim. Resonant magneto-optical properties of Fe near its 2p levels, measurement and applications. *Phys. Rev. B*, 62:12216, 2000.

[92] J. D. Jackson. *Classical Electrodynamics*. Wiley, 1975.

[93] http://scalfmm-public.gforge.inria.fr/doc/.

[94] L. Ying, G. Biros, and D. Zorin. A kernel-independent adaptative fast multipole method in two and three dimensions. *Journal of Computational Physics*, 196:591–626, 2004.

[95] www.boost.org.

[96] http://doc.cgal.org/4.5.2/manual/packages.html.

[97] http://www.cs.umd.edu/ mount/ann/.

[98] H. S. M. Coxeter. *Introduction to Geometry, 2nd ed.*, page 218. Wiley, 1969.

[99] http://www.paraview.org.

[100] https://wci.llnl.gov/codes/visit/.

[101] http://www.avs.com/solutions/express/.

[102] The MathWorks, Inc. MATLAB and Simulink are registered trademarks of The MathWorks, Inc. see mathworks.com.